

---

# Simulation of quantum vacuum in higher dimensions

Arnau Pons Domenech

---



2017



---

# Simulation of quantum vacuum in higher dimensions

Arnau Pons Domenech

---

Doctoral thesis  
at the Physics Department  
of the Ludwig-Maximilians-Universität  
München

presented by  
Arnau Pons Domenech  
from Barcelona

Munich, 2017

Evaluator: Prof. Dr. Hartmut Ruhl

Zweitgutachter: Prof. Dr. Holger Gies

Tag der Abgabe: 19.12.2017

Tag der mündlichen Prüfung: 14.02.2018

# Zusammenfassung

Mit der Einführung neuer Petawatt (PW) Lasersysteme (ELI-NP, Firex-I, HIBEF) wird es möglich, nichtperturbativen Quantenvakuumeffekte experimentell zu erforschen. Nichtlineare Vakuumeffekte sind für starke elektromagnetische Felder zuerst von Heisenberg und Euler vorhergesagt worden. Später sind sie von Schwinger im Rahmen seiner *Effective Time* Methode reproduziert worden. Nichtlineare Vakuumeffekte haben ihren Ursprung in der Erzeugung und Vernichtung von virtuellen Teilchenpaaren in starken elektromagnetischen Feldern und dem Dipolmoment, das sie während ihrer Lebenspanne erzeugen.

Ziel der vorliegenden Dissertation ist es, den von Schwinger eingeführten *Effective Time* Formalismus zu benutzen, um ein numerisches Simulationsprogramm zu entwickeln. Das Programm soll es ermöglichen, die an den großen Laserinfrastrukturen (ELI-NP, Firex-I und andere) geplanten Experimente detailgetreu zu modellieren und somit ein unentbehrliches Werkzeug für das Verständnis und die Parameterwahl der geplanten Experimente zu werden.

Zu diesem Zweck wird ein Satz von modifizierten Maxwell-Gleichungen verwendet, welche aus einer geeigneten Schwachfeldentwicklung des Heisenberg-Euler Lagrangians hergeleitet werden. Die von diesen Gleichungen beschriebenen elektromagnetischen Felder werden auf ein diskretes Gitter projiziert, um zu einem Satz von gewöhnlichen Differentialgleichungen (GDGL) zu gelangen. Diese Differentialgleichungen werden mit Hilfe des generischen GDGL Löasers CVODE aus der SUNDIALS Bibliothek gelöst.

Die größten Hindernisse, die in dieser Arbeit überwunden werden mussten, sind (i) die Herleitung eines nutzbaren analytischen Rahmens, (ii) die Bestimmung und Berechnung der maßgebenden Variablen des Problems (Ableitungsgewichtungen, Jacobi Matrizen, elektromagnetische Invarianten, Eigenrichtungen, ... ), (iii) die Entwicklung eines geeigneten numerischen Algorithmus, welcher die Steifheit und implizite Natur der zugrunde liegenden partiellen Differentialgleichung mit einbezieht und (iv) das Optimieren des resultierenden Auslastungsproblems der verwendeten Computer.

Der resultierende neue Simulationsalgorithmus für das Quantenvakuum wird erfolgreich mit Hilfe bekannter nichtlinearer Quantenvakuumphänomene geprüft und dazu benutzt die verschiedenen Eigenschaften des Quantenvakuums zu untersuchen. Diese sind unter anderem Vakuum Doppelbrechung, die Erzeugung von Oberschwingungen in höheren Dimensionen, die Fokussierung, Brechung und Spie-

gelung von Licht durch Licht, etc.

# Abstract

With the introduction of new petawatt (PW) class lasers (ELI-NP, Firex-I, HIBEF) a new regime becomes accessible, where nonperturbative quantum vacuum effects can be measured. First predicted in strong electromagnetic(em)-fields by Heisenberg and Euler, these vacuum effects were later introduced into the effective time framework of QED by Schwinger. They originate in the creation and annihilation of virtual particle pairs in extremely strong electromagnetic fields and the dipole moment that arises during this closed loop process.

The goal of this thesis is to use the effective time framework derived by the aforementioned people to develop a computer simulation framework which allows the accurate modeling of planned experiments at ELI-NP, Firex-I, and other sites, thus delivering a crucial tool for the determination and understanding of relevant experiments.

To this end, a set of modified Maxwell equations is required, which are derived with the help of an appropriate weak field expansion of the Heisenberg-Euler Lagrangian. The em-fields are then projected onto a finite difference lattice leading to a set of ordinary differential equations (ODE's) for the time propagation of the em-fields. The ODE's are solved in time using the generic ODE solver CVODE from the SUNDIALS library.

The main obstacles that had to be overcome in this thesis were (i) the derivation of a suitable analytic framework (ii) the determination of the key variables (stencil values, Jacobi matrices, electromagnetic invariants, eigen directions, ...), (iii) developing a suitable numerical scheme taking into account the stiffness and implicitness of the PDE, and (iv) resolving the resulting computational load challenge.

The resulting new quantum vacuum simulation (QVS) algorithm is tested successfully against a set of already known results and used to simulate a variety of different setups highlighting different properties of the quantum vacuum. These include among others vacuum birefringence, high harmonic generation in higher dimensions, light by light focusing and light by light diffraction/refraction.



# Contents

<b>1. Introduction</b>	<b>1</b>
1.1. Classical electrodynamics . . . . .	1
1.2. Nonlinear media: Polarization tensor . . . . .	2
1.3. The vacuum as a nonlinear QED vacuum . . . . .	4
1.4. Structure of the thesis . . . . .	4
<b>2. State of the art</b>	<b>7</b>
2.1. The Dirac equation . . . . .	7
2.2. Schwinger's proper time formalism . . . . .	9
2.2.1. The zero field case . . . . .	16
2.2.2. The Heisenberg-Euler Lagrangian . . . . .	19
2.2.3. Beyond the constant field approximation . . . . .	27
2.3. Non-pertubative pair production . . . . .	28
2.4. The weak field expansion . . . . .	29
2.5. The nonlinear Maxwell equations . . . . .	31
2.5.1. Euler-Lagrange formalism . . . . .	33
2.5.2. Comparison with the classical Maxwell equations . . . . .	34
2.6. The probe in a constant field case . . . . .	34
2.7. The case of two colliding plane wave pulses . . . . .	36
2.7.1. Contributions from 4-photon interaction . . . . .	37
2.7.2. Contributions from 6-photon interaction . . . . .	39
2.7.3. Analytical solution . . . . .	39
<b>3. State of the art in numerical mathematics</b>	<b>45</b>
3.1. Classification of PDE . . . . .	45
3.2. The finite element method (FEM) . . . . .	47
3.3. The three wave mixing method . . . . .	49
3.4. The Yee algorithm . . . . .	49
3.5. The general finite difference case . . . . .	50
3.5.1. The Nyquist frequency . . . . .	54
3.5.2. Consistency, stability, convergence . . . . .	55

## Contents

<b>4. Programming concepts</b>	<b>57</b>
4.1. Key computational concepts . . . . .	57
4.2. Parallel machines . . . . .	58
<b>5. The quantum vacuum simulation algorithm for the Heisenberg-Euler Lagrangian</b>	<b>61</b>
5.1. Reformulation of the Maxwell equations . . . . .	61
5.2. From PDE to ODE . . . . .	63
5.3. Analytical properties of the numerical scheme . . . . .	65
5.4. Remarks on the implementation . . . . .	71
<b>6. Benchmarks</b>	<b>77</b>
6.1. The constant background case . . . . .	77
6.2. Vacuum birefringence . . . . .	78
6.3. High harmonic generation . . . . .	83
<b>7. Simulation results beyond the scope of analytically solvable setups</b>	<b>89</b>
7.1. Harmonic generation in the nonzero frequency background case . . . . .	89
7.2. Gaussian Beams in 2 Dimension . . . . .	91
7.3. Non-coaxial collisions . . . . .	93
7.3.1. The quasi 1D case . . . . .	93
7.3.2. Collisions between pulses with the same polarization at an angle . . . . .	95
7.3.3. Polarization tagging of colliding pulses . . . . .	98
7.4. Focusing of light by light . . . . .	98
7.5. Reflection effects at the pump . . . . .	102
7.6. Rabi oscillations . . . . .	104
<b>8. Summary and conclusions</b>	<b>109</b>
8.1. Outlook . . . . .	110
<b>A. Notation</b>	<b>115</b>
<b>B. Further calculations</b>	<b>119</b>
<b>Bibliography</b>	<b>123</b>

# 1. Introduction

## 1.1. Classical electrodynamics

In 1865 Maxwell [1] published the four differential equations that described the electromagnetic interactions in the non-relativistic regime. These can be written as [2]:

$$\begin{aligned}\nabla \cdot \vec{D} &= 4\pi\rho_f, \\ \nabla \cdot \vec{B} &= 0, \\ \nabla \times \vec{E} &= -\frac{1}{c}\frac{\partial \vec{B}}{\partial t}, \\ \nabla \times \vec{H} &= \frac{1}{c}\left(4\pi\vec{j}_f + \frac{\partial \vec{D}}{\partial t}\right),\end{aligned}\tag{1.1}$$

where  $\vec{E}$  is the electric,  $\vec{B}$  the magnetic,  $\vec{H}$  the magnetizing,  $\vec{D}$  the displacement field, and  $\vec{j}_f$  the current vector. Here,  $\vec{H}$  and  $\vec{D}$  are defined by

$$\begin{aligned}\vec{D} &= \epsilon\vec{E} + \vec{P}, \\ \vec{H} &= \frac{1}{\mu}\vec{B} - \vec{M},\end{aligned}\tag{1.2}$$

with  $\vec{P}$  being the polarization and  $\vec{M}$  the magnetization. These were assumed to be caused by the interaction of light with matter.

When in vacuum, the equations simplify to  $\rho_f = \vec{j}_f = 0$ ,  $\vec{D} = \vec{E}$  and  $\vec{H} = \vec{B}$  leaving only a set of linear equations behind. The main consequence is that no matter the amount of interacting elements or their intensities, the resulting field configuration can always be derived by propagating each component separately at an arbitrary intensity and then scaling and combining the results. The important physical implication of this mathematical quirk is that in Maxwell's picture light can never interact with light.

## 1. Introduction

### 1.2. Nonlinear media: Polarization tensor

Things change when an optical medium is introduced. The now non-zero polarization can be written as:

$$\frac{P_i}{\epsilon_0} = \sum_j \chi_{ij}^{(1)} E_j + \sum_{jk} \chi_{ijk}^{(2)} E_j E_k + \sum_{jkl} \chi_{ijkl}^{(3)} E_j E_k E_l + \dots \quad (1.3)$$

The most common way to classify these contributions is into linear ( $\chi^{(1)}$ ) and nonlinear terms ( $\chi^{(2)}$  and higher).

Linear contributions lead to a change of the refractive index, causing a difference in light propagation speed, which in turn causes light reflection and diffraction (see figure 1.2). In cases where  $\chi^{(1)} \neq c1_2$ , the medium is anisotropic sourcing effects such as the rotation of the polarization axis of the traversing electromagnetic field and polarization dependent refraction/reflection. The latter effect is called birefringence (see figure 1.3) and is usually caused by the presence of dipoles in the crystal.

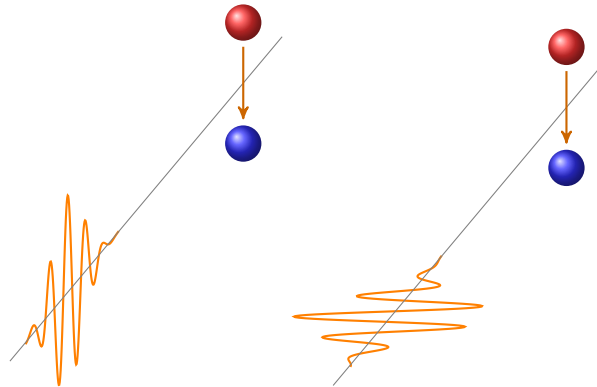


**Figure 1.1.:** Sketch of an electric component of a light pulse propagating through an electric dipole. To the left, the electric field is parallel to the axis of the dipole and thus the dipole interacts with it. To the right, the field is orthogonal and thus the field does not perceive any dipole moment.

The nonlinear  $\chi$  are the origin of effects such as optical field rectification, Raman effect Kerr effect, high harmonic generation, etc. While microscopically these effects have a more complex mechanism, e.g., the recombination of an electron that has escaped through quantum tunneling, on a macroscopic scale they can be approximated by contributions to the  $\chi$  matrices.

1.2. Nonlinear media: Polarization tensor

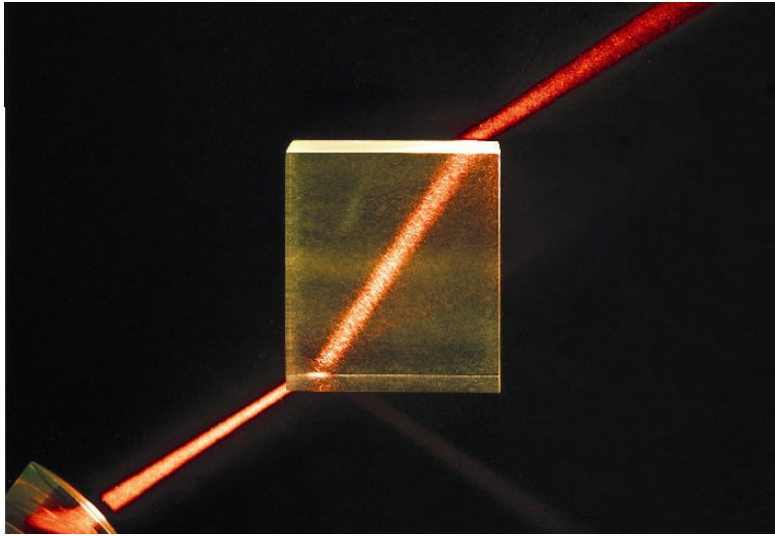


**Figure 1.2.:** Photograph of a light beam reflected and diffracted on a square cristal.(Source:[http://www.topgeo.de/bilder/calcit-doppelspat\\_13312.jpg](http://www.topgeo.de/bilder/calcit-doppelspat_13312.jpg))



**Figure 1.3.:** Photograph of a calcite crystal on a piece of paper. (Source:[http://www.topgeo.de/bilder/calcit-doppelspat\\_13312.jpg](http://www.topgeo.de/bilder/calcit-doppelspat_13312.jpg))

### 1.3. The vacuum as a nonlinear QED vacuum

Subsequently in 1927 [3] the postulation of the theory for absorption and emission of radiation changed the physical landscape. Now, photons could decay by themselves into electron positron pairs. These pairs in turn can act as a dipole for other photons, thereby causing the vacuum to become a nonlinear optical medium when subjected to high intensity fields.

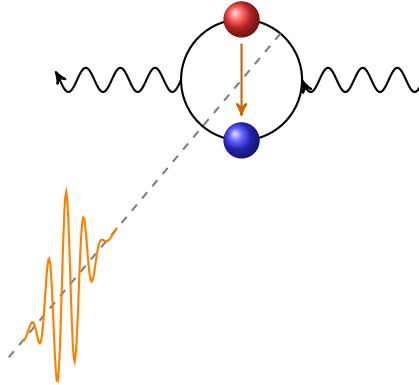


**Figure 1.4.:** Sketch of an electric component of a light pulse propagating through an electric dipole created by an electron positron pair.

The resulting Lagrangian was first published by Heisenberg and Euler in 1935 [4], describing a fully nonlinear medium that is anisotropic due to the polarization direction of the strong background, which creates the pairs, generating a characteristic direction.

Due to the small cross section of these effect, it was considered merely a theoretical quirk at the time. However, with the arrival of Petawatt class lasers (e.g. ELI-NP and others [5, 6, 7]) these effects enter the regime of experimental observability [8]. The analytic computation of the strength and form of these interactions is nevertheless not possible except in a few severely constrained scenarios. Thus, there is a need for the development of a computer algorithm to simulate the light interactions in quantum vacuum.

### 1.4. Structure of the thesis

This thesis is divided into 8 chapters. Chapter 2, presents the derivation of the analytic framework used as a basis for all further computational derivations. It mainly follows the method presented by Schwinger [9] combined with some modern results [8, 10, 11, 12, 13, 14]. Chapter 3, gives a description of the most

#### 1.4. Structure of the thesis

common PDE solving algorithms along with a brief discussion of their suitability for the solution of a nonlinear Maxwell equation. Next, chapter 4 contains a brief introduction to the key computational concepts that are relevant in shaping the quantum vacuum simulation algorithm (QVSA). Chapter 5 uses the information presented in the previous 3 chapters to derive the QVSA. Then, in chapter 6, the QVSA is benchmarked against the results published in [8, 10, 13]. With the validated algorithm at hand chapter 7 goes into the non-explored realms of quantum vacuum physics and studies effects such as light by light focusing, high harmonic generation in higher dimensions,... . Finally, chapter 8 offers a summary of the results presented throughout the thesis as well as an outlook into possible future applications.



## 2. State of the art

Reproducing the work in [8, 9, 10], the Heisenberg-Euler (HE) Lagrangian is derived from first principle starting with the Dirac equation and using Schwinger's proper time formalism. Furthermore, its low energy approximation is computed and its effect on the Maxwell-Ampère law is derived. Last but not least the analytic results for specific initial settings are presented. This serves to introduce the notation and definitions used throughout this thesis, present the framework on which the simulations will be build and set the benchmarks against which the simulation algorithm will be tested.

### 2.1. The Dirac equation

The non-interacting Klein-Gordon equation is considered as a starting point

$$(\partial_\mu \partial^\mu + m^2) \phi = 0. \quad (2.1)$$

It correctly describes the relativistic kinematics of spinless particles but cannot be adapted to account for spin particles, such as all the elementary particles except the Higgs-Boson. In order to introduce spin coupling and other effects, it is necessary to consider the Dirac equation

$$(i\gamma^\mu \partial_\mu - m) \Psi = 0. \quad (2.2)$$

The Dirac equation is considered to be the "root" of the Klein-Gordon equation since the multiplication of its functional by its complex conjugated yields

$$(-i\gamma^\mu \partial_\mu - m) (i\gamma^\nu \partial_\nu - m) \Psi = 0, \quad (2.3)$$

which may be rewritten as

$$(\gamma^\mu \gamma^\nu \partial_\mu \partial_\nu + m^2) \Psi = 0. \quad (2.4)$$

Symmetrizing (2.4) results in a symmetric and an anti-symmetric combination of gamma matrices

$$\left[ \frac{1}{2}(\gamma^\mu \gamma^\nu + \gamma^\nu \gamma^\mu) \partial_\mu \partial_\nu + \frac{1}{2}(\gamma^\mu \gamma^\nu - \gamma^\nu \gamma^\mu) \partial_\mu \partial_\nu + m^2 \right] \Psi = 0. \quad (2.5)$$

## 2. State of the art

As the second term in (2.5) is the summation over the product of a symmetric and an anti-symmetric term it must be zero. Now, in order to reproduce the Klein-Gordon equation the relation

$$\{\gamma^\mu, \gamma^\nu\} = 2g^{\mu\nu} \quad (2.6)$$

must be fulfilled. This is the so called on shell condition.

### Coupling to the electromagnetic field

In order to formulate a quantum field theory (QFT) for the quantum vacuum a Lagrangian is required. The Lagrangian for the free Dirac field is

$$\mathcal{L} = \bar{\Psi} i \gamma^\mu \partial_\mu \Psi - m \bar{\Psi} \Psi, \quad (2.7)$$

where  $\bar{\Psi} = \Psi^\dagger \gamma_0$  is the adjoint spinor, which satisfies the *equal time* anti-commutation relation

$$\{\Psi(\mathbf{x}), \bar{\Psi}(\mathbf{x}')\} = \gamma_0 \delta^{(3)}(\vec{x} - \vec{x}'). \quad (2.8)$$

The Dirac equation is obtained by using the Euler-Lagrange formalism with the adjoint spinor as a variable, i.e.,  $\partial \mathcal{L} / \partial \bar{\Psi} = 0$ . It can be seen that (2.7) is invariant under a global phase transformation

$$\Psi \rightarrow e^{-ie\alpha} \Psi, \quad (2.9)$$

as the multiplication of  $\Psi$  with its complex conjugate will cancel out. Here  $e$  is the elementary charge and  $\alpha$  the phase. If the phase is no longer globally constant, i.e.,  $\alpha = \alpha(x)$ , the first term of the Lagrangian (2.7) becomes

$$\bar{\Psi} \partial_\mu \Psi \rightarrow e^{ie\alpha} \bar{\Psi} \partial_\mu e^{-ie\alpha} \Psi = \bar{\Psi} \partial_\mu \Psi - ie \bar{\Psi} (\partial_\mu \alpha) \Psi. \quad (2.10)$$

In order for the Lagrangian to remain invariant under a local phase transformation as in (2.10) the derivative  $\partial_\mu$  needs to be exchanged with the so called *covariant* derivative

$$\partial_\mu \rightarrow D_\mu = \partial_\mu + ie A_\mu. \quad (2.11)$$

Here  $A_\mu$  is the *gauge field* that transforms as

$$A_\mu \rightarrow A'_\mu = A_\mu + \partial_\mu \alpha. \quad (2.12)$$

With this transformation the second term in (2.10) vanishes as

$$\begin{aligned} D_\mu \Psi &\rightarrow (\partial_\mu + ie A'_\mu) e^{-ie\alpha} \Psi \\ &= (\partial_\mu + ie A_\mu + ie \partial_\mu \alpha) e^{-ie\alpha} \Psi \end{aligned}$$

## 2.2. Schwinger's proper time formalism

$$\begin{aligned}
&= e^{-ie\alpha}(\partial_\mu + ieA_\mu + ie\partial_\mu\alpha - ie\partial_\mu\alpha)\Psi \\
&= e^{-ie\alpha}D_\mu\Psi.
\end{aligned} \tag{2.13}$$

The Dirac equations for the spinors and their adjoints in position space become

$$\gamma^\mu(-i\partial_\mu - eA_\mu(\mathbf{x}))\Psi(\mathbf{x}) + m\Psi(\mathbf{x}) = 0, \tag{2.14}$$

$$(i\partial_\mu - eA_\mu(\mathbf{x}))\bar{\Psi}(\mathbf{x})\gamma^\mu + m\bar{\Psi}(\mathbf{x}) = 0. \tag{2.15}$$

## 2.2. Schwinger's proper time formalism

The current vector can be derived from the symmetrisation of the charge as

$$j_\mu(\mathbf{x}) = -\frac{e}{2}(\gamma_\mu)_{\alpha\beta}[\Psi_\alpha(\mathbf{x}), \bar{\Psi}_\beta(\mathbf{x})] = \frac{e}{2}[\bar{\Psi}(\mathbf{x}), \gamma_\mu\Psi(\mathbf{x})], \tag{2.16}$$

where the right hand side is in matrix notation. This current vector can be related to time symmetry. To see this the chronologically ordered operator

$$(A(\mathbf{x})B(\mathbf{x}'))_+ = \begin{cases} A(\mathbf{x})B(\mathbf{x}'), & \text{for } x_0 > x'_0 \\ B(\mathbf{x}')A(\mathbf{x}), & \text{for } x_0 < x'_0 \end{cases} \tag{2.17}$$

is introduced. With the help of (2.17) and the time sign operator

$$\text{tsgn}(\mathbf{x}) = \begin{cases} 1, & \text{for } x_0 > 0 \\ -1, & \text{for } x_0 < 0 \end{cases}. \tag{2.18}$$

for  $\Psi$  and  $\bar{\Psi}$  it is found that

$$(\Psi_\alpha(\mathbf{x}), \bar{\Psi}_\beta(\mathbf{x}'))_+ \text{tsgn}(\mathbf{x} - \mathbf{x}') = \begin{cases} \Psi_\alpha(\mathbf{x})\bar{\Psi}_\beta(\mathbf{x}'), & \text{for } x_0 > x'_0 \\ -\bar{\Psi}_\beta(\mathbf{x}')\Psi_\alpha(\mathbf{x}), & \text{for } x_0 < x'_0 \end{cases}. \tag{2.19}$$

With it the commutator of the spinors takes the form

$$\begin{aligned}
[\Psi_\alpha(\mathbf{x}), \bar{\Psi}_\beta(\mathbf{x})] &= \Psi_\alpha(\mathbf{x})\bar{\Psi}_\beta(\mathbf{x}) - \bar{\Psi}_\beta(\mathbf{x})\Psi_\alpha(\mathbf{x}) \\
&= \lim_{\mathbf{x}' \rightarrow \mathbf{x}} [\Psi_\alpha(\mathbf{x})\bar{\Psi}_\beta(\mathbf{x}') - \bar{\Psi}_\beta(\mathbf{x}')\Psi_\alpha(\mathbf{x})] \\
&= \lim_{\mathbf{x}' \nearrow \mathbf{x}} \Psi_\alpha(\mathbf{x})\bar{\Psi}_\beta(\mathbf{x}') - \lim_{\mathbf{x}' \searrow \mathbf{x}} \bar{\Psi}_\beta(\mathbf{x}')\Psi_\alpha(\mathbf{x}) \\
&= \lim_{\mathbf{x}' \nearrow \mathbf{x}} (\Psi_\alpha(\mathbf{x}), \bar{\Psi}_\beta(\mathbf{x}'))_+ \text{tsgn}(\mathbf{x} - \mathbf{x}') \\
&\quad + \lim_{\mathbf{x}' \searrow \mathbf{x}} (\Psi_\alpha(\mathbf{x}), \bar{\Psi}_\beta(\mathbf{x}'))_+ \text{tsgn}(\mathbf{x} - \mathbf{x}') \\
&= 2 \lim_{\mathbf{x}' \rightarrow \mathbf{x}} (\Psi_\alpha(\mathbf{x}), \bar{\Psi}_\beta(\mathbf{x}'))_+ \text{tsgn}(\mathbf{x} - \mathbf{x}').
\end{aligned} \tag{2.20}$$

## 2. State of the art

The validity of the insertion and exchange of the limit operators is given by the fact that the Dirac spinors are differentiable and therefore smooth. This causes all the limits above to exist and thus the equivalence of the expressions. Using (2.20) the expectation value  $\langle \cdot \rangle$  for the current  $j_\mu$  becomes

$$\begin{aligned}
\langle j_\mu(\mathbf{x}) \rangle &= \left\langle \frac{-e}{2} (\gamma_\mu)_{\alpha\beta} [\Psi_\alpha(\mathbf{x}), \bar{\Psi}_\beta(\mathbf{x})] \right\rangle \\
&= \left\langle \frac{i^2 e}{2} (\gamma_\mu)_{\alpha\beta} 2 \lim_{\mathbf{x}' \rightarrow \mathbf{x}} (\Psi_\alpha(\mathbf{x}), \bar{\Psi}_\beta(\mathbf{x}'))_+ \text{tsgn}(\mathbf{x} - \mathbf{x}') \right\rangle \\
&= ie (\gamma_\mu)_{\alpha\beta} i \lim_{\mathbf{x}' \rightarrow \mathbf{x}} \langle (\Psi_\alpha(\mathbf{x}), \bar{\Psi}_\beta(\mathbf{x}'))_+ \rangle \text{tsgn}(\mathbf{x} - \mathbf{x}') \\
&= ie \text{tr} \gamma_\mu i \langle (\Psi(\mathbf{x}), \bar{\Psi}(\mathbf{x}'))_+ \rangle \text{tsgn}(\mathbf{x} - \mathbf{x}')|_{\mathbf{x}' \rightarrow \mathbf{x}}. \tag{2.21}
\end{aligned}$$

Here  $\text{tr}$  is defined as

$$\text{tr} M = \sum_{\alpha} M_{\alpha\alpha} \tag{2.22}$$

and the double sum in the next to last line of (2.21) reduces to it by virtue of (2.8). Defining

$$G(\mathbf{x}, \mathbf{x}') = i \langle (\Psi(\mathbf{x}), \bar{\Psi}(\mathbf{x}'))_+ \rangle \text{tsgn}(\mathbf{x} - \mathbf{x}') \tag{2.23}$$

makes it possible to write (2.21) as

$$\langle j_\mu(\mathbf{x}) \rangle = ie \text{tr} \gamma_\mu G(\mathbf{x}, \mathbf{x}')|_{\mathbf{x}' \rightarrow \mathbf{x}}. \tag{2.24}$$

Since  $\text{tsgn}$  is constant for all  $x_0 \neq x'_0$ , the differential equation describing  $G(\mathbf{x}, \mathbf{x}')$  is the same as the one describing the spinors when  $x_0 \neq x'_0$

$$[\gamma^\mu(-i\partial_\mu - eA_\mu(\mathbf{x})) + m]G(\mathbf{x}, \mathbf{x}') = 0. \tag{2.25}$$

It holds in a weak sense that  $\partial_0 \text{tsgn}(\mathbf{x} - \mathbf{x}') = 2\delta(x_0 - x'_0)$ . Equation (2.25) can be amended to describe the whole space

$$\begin{aligned}
0 &= [\gamma^\mu(-i\partial_\mu - eA_\mu(\mathbf{x})) + m]G(\mathbf{x}, \mathbf{x}') - \gamma^0(-i)2\delta(x_0 - x'_0)i \langle (\Psi(\mathbf{x}), \bar{\Psi}(\mathbf{x}'))_+ \rangle \\
&\stackrel{\text{avg}}{=} [\gamma^\mu(-i\partial_\mu - eA_\mu(\mathbf{x})) + m]G(\mathbf{x}, \mathbf{x}') - \gamma^0 2\delta(x_0 - x'_0) \left\langle \frac{\Psi(\mathbf{x})\bar{\Psi}(\mathbf{x}') + \bar{\Psi}(\mathbf{x}')\Psi(\mathbf{x})}{2} \right\rangle \\
&= [\gamma^\mu(-i\partial_\mu - eA_\mu(\mathbf{x})) + m]G(\mathbf{x}, \mathbf{x}') - \gamma^0 \delta(x_0 - x'_0) \langle \{\Psi(\mathbf{x}), \bar{\Psi}(\mathbf{x}')\} \rangle \\
&\stackrel{(2.8)}{=} [\gamma^\mu(-i\partial_\mu - eA_\mu(\mathbf{x})) + m]G(\mathbf{x}, \mathbf{x}') - \gamma^0 \delta(x_0 - x'_0) \langle \gamma_0 \delta^{(4)}(\mathbf{x} - \mathbf{x}') \rangle \\
&= [\gamma^\mu(-i\partial_\mu - eA_\mu(\mathbf{x})) + m]G(\mathbf{x}, \mathbf{x}') - \mathbf{1}_4 \delta^{(4)}(\mathbf{x} - \mathbf{x}'), \tag{2.26}
\end{aligned}$$

by making use of the chain rule to subtract the extra term and averaging over the limit from above and below. Equation (2.26) can be reformulated into

$$[\gamma^\mu(-i\partial_\mu - eA_\mu(\mathbf{x})) + m]G(\mathbf{x}, \mathbf{x}') = \delta^{(4)}(\mathbf{x} - \mathbf{x}'). \tag{2.27}$$

## 2.2. Schwinger's proper time formalism

Therefore  $G(\mathbf{x}, \mathbf{x}')$  is a Green's function for the Dirac field. It can be interpreted as an element of the operator  $G$ , which operates in four spinor dimensions and two spacetime dimensions, fulfilling

$$G(\mathbf{x}, \mathbf{x}') = \langle \mathbf{x} | G | \mathbf{x}' \rangle . \quad (2.28)$$

Then, (2.27) can be rewritten as

$$(\gamma^\mu \Pi_\mu + m)G = \mathbf{1} . \quad (2.29)$$

Here the definition

$$\Pi_\mu = p_\mu - eA_\mu \quad (2.30)$$

has been used. The commutation relation for this new momentum operator can be computed with the help of the canonical momentum and the space operator commutation relations in position space

$$[x_\mu, p_\nu] = i\delta_{\mu\nu} , \quad (2.31)$$

$$[p_\mu, p_\nu] = 0 . \quad (2.32)$$

With the help of (2.31) and (2.32) it is obtained that

$$\begin{aligned} [x_\mu, \Pi_\nu] &= [x_\mu, p_\nu] - e[x_\mu, A_\nu(\mathbf{x})] \\ &= i\delta_{\mu\nu} - e0 \\ &= i\delta_{\mu\nu} , \end{aligned} \quad (2.33)$$

$$\begin{aligned} [\Pi_\mu, \Pi_\nu] &= [p_\mu, p_\nu] - e[p_\mu, A_\nu(\mathbf{x})] - e[A_\mu(\mathbf{x}), p_\nu] + e^2[A_\mu(\mathbf{x}), A_\nu(\mathbf{x})] \\ &= 0 - e[-i\partial_\mu, A_\nu(\mathbf{x})] - e[A_\mu(\mathbf{x}), -i\partial_\nu] + e^20 \\ &= ie [\partial_\mu A_\nu(\mathbf{x}) - A_\nu(\mathbf{x})\partial_\mu + A_\mu(\mathbf{x})\partial_\nu - \partial_\nu A_\mu(\mathbf{x})] \\ &= ie [(\partial_\mu(A_\nu(\mathbf{x})) + A_\nu(\mathbf{x})\partial_\mu) - A_\nu(\mathbf{x})\partial_\mu \\ &\quad + A_\mu(\mathbf{x})\partial_\nu - (\partial_\nu(A_\mu(\mathbf{x})) + A_\mu(\mathbf{x})\partial_\nu)] \\ &= ie [\partial_\mu(A_\nu(\mathbf{x})) - \partial_\nu(A_\mu(\mathbf{x}))] . \end{aligned} \quad (2.34)$$

Defining the *electromagnetic field tensor*  $F_{\mu\nu}$  via

$$F_{\mu\nu} = \partial_\mu(A_\nu(\mathbf{x})) - \partial_\nu(A_\mu(\mathbf{x})) \quad (2.35)$$

yields the expression for the commutation relations to

$$[x_\mu, \Pi_\nu] = i\delta_{\mu\nu} , \quad [\Pi_\mu, \Pi_\nu] = ieF_{\mu\nu} . \quad (2.36)$$

Now, using the operator approach presented in [15] the current vector can be determined by the variation of the action  $S$  with respect to the gauge field, i.e.,

$$\frac{\delta S[\Psi, \bar{\Psi}, A]}{\delta A_\mu} = \langle j^\mu(\mathbf{x}) \rangle , \quad (2.37)$$

## 2. State of the art

where  $S$  is the well known action of quantum dynamics. In order to reduce the actions  $S$  in (2.37) to an effective action  $W^{(1)}$  the fermionic degrees of freedom need to be averaged out, leaving

$$\frac{\delta W^{(1)}[A]}{\delta A_\mu} = {}_A \langle 0 | j^\mu(\mathbf{x}) | 0 \rangle_A. \quad (2.38)$$

Here  $|0\rangle_A$  is the ground state of the quantum vacuum in the presence of a gauge field. By multiplying both sides of (2.38) with the variation of the gauge field and using the expression of  $\langle j^\mu(\mathbf{x}) \rangle$  given in (2.24) allows the derivation of the expression

$$\begin{aligned} \delta W^{(1)} &= \int d^4\mathbf{x} \delta A_\mu(\mathbf{x}) \langle j^\mu(\mathbf{x}) \rangle \\ &= \int d^4\mathbf{x} \delta A_\mu(\mathbf{x}) i e \text{tr} \gamma^\mu \langle \mathbf{x} | G | \mathbf{x} \rangle \\ &= \int d^4\mathbf{x} \langle \mathbf{x} | \delta A_\mu | \mathbf{x} \rangle i e \text{tr} \gamma^\mu \langle \mathbf{x} | G | \mathbf{x} \rangle \\ &= i e \int d^4\mathbf{x} \text{tr} \gamma^\mu \langle \mathbf{x} | \delta A_\mu | \mathbf{x} \rangle \langle \mathbf{x} | G | \mathbf{x} \rangle \\ &= i e \int d^4\mathbf{x} \langle \mathbf{x} | \text{tr} \gamma^\mu \delta A_\mu G | \mathbf{x} \rangle \\ &= i e \text{Tr} (\gamma^\mu \delta A_\mu G), \end{aligned} \quad (2.39)$$

where  $\text{Tr}$  is the trace over spinor-indices, space and time. Furthermore, the operator  $\delta A_\mu$  is defined such that

$$\langle \mathbf{x} | \delta A_\mu | \mathbf{x}' \rangle = \delta^{(4)}(\mathbf{x} - \mathbf{x}') \delta A_\mu(\mathbf{x}). \quad (2.40)$$

It follows that

$$- e \gamma^\mu \delta A_\mu = \delta(\gamma^\mu \Pi_\mu + m), \quad (2.41)$$

since  $\delta m = \delta p = 0$ . Also the relation

$$\frac{1}{x} = i \int_0^\infty ds e^{-ixs} \quad (2.42)$$

can be used to write  $G = (\gamma^\mu \Pi_\mu + m)^{-1}$  as

$$G = i \int_0^\infty ds e^{-i(\gamma^\mu \Pi_\mu + m)s}. \quad (2.43)$$

Inserting (2.41) and (2.43) in (2.39) yields

$$\delta W^{(1)} = - i \text{Tr} \delta(\gamma^\mu \Pi_\mu + m) i \int_0^\infty ds e^{-i(\gamma^\mu \Pi_\mu + m)s}$$

## 2.2. Schwinger's proper time formalism

$$\begin{aligned}
&= \int_0^\infty ds \operatorname{Tr} \delta(\gamma^\mu \Pi_\mu + m) e^{-i(\gamma^\mu \Pi_\mu + m)s} \\
&\stackrel{*}{=} \int_0^\infty ds \operatorname{Tr} \frac{i}{s} \delta(e^{-i(\gamma^\mu \Pi_\mu + m)s}) \\
&\stackrel{**}{=} \int_0^\infty ds \operatorname{Tr} \frac{i}{s} \delta(e^{-i\gamma^\mu \Pi_\mu} e^{-ims}) \\
&= \delta \left( i \int_0^\infty ds \frac{e^{-ims}}{s} \operatorname{Tr} e^{-i\gamma^\mu \Pi_\mu} \right). \tag{2.44}
\end{aligned}$$

Step (\*) is a direct consequence of applying the chain rule on  $\delta e^{-i\phi s}$ , where  $\phi = \gamma^\mu \Pi_\mu + m$  and (\*\*) follows from the fact that  $\operatorname{Tr}[AB] = \operatorname{Tr}[BA]$ . Comparing the right hand side with the left hand side of (2.44) gives

$$i \int_0^\infty ds \frac{e^{-ims}}{s} \operatorname{Tr} e^{-i\gamma^\mu \Pi_\mu} = W^{(1)} \stackrel{!}{=} \int d^4 \mathbf{x} \mathcal{L}^{(1)}(\mathbf{x}), \tag{2.45}$$

from which directly follows, that

$$\mathcal{L}^{(1)}(\mathbf{x}) = i \int_0^\infty ds \frac{e^{-ims}}{s} \operatorname{tr} \langle \mathbf{x} | e^{-i\gamma^\mu \Pi_\mu} | \mathbf{x} \rangle. \tag{2.46}$$

### Alternative representation for the Green operator

Since  $[m, \gamma^\mu \Pi_\mu] = 0$ , it can be computed that

$$\begin{aligned}
(m + \gamma^\mu \Pi_\mu)(m - \gamma^\mu \Pi_\mu) &= m^2 + m\gamma^\mu \Pi_\mu - m\gamma^\mu \Pi_\mu - (\gamma^\mu \Pi_\mu)^2 \\
&= m^2 - (\gamma^\mu \Pi_\mu)^2 \tag{2.47}
\end{aligned}$$

and thus the Green's operator  $G$  may be rewritten as

$$G = \frac{1}{m + \gamma^\mu \Pi_\mu} = \frac{m - \gamma^\mu \Pi_\mu}{m^2 - (\gamma^\mu \Pi_\mu)^2} = (m - \gamma^\mu \Pi_\mu)(m^2 - (\gamma^\mu \Pi_\mu)^2)^{-1} \tag{2.48}$$

$$= (m^2 - (\gamma^\mu \Pi_\mu)^2)^{-1}(m - \gamma^\mu \Pi_\mu), \tag{2.49}$$

which when using the identity in (2.42) becomes

$$G = (m - \gamma^\mu \Pi_\mu) i \int_0^\infty ds e^{-i(m^2 - (\gamma^\mu \Pi_\mu)^2)s} \tag{2.50}$$

$$= i \int_0^\infty ds e^{-i(m^2 - (\gamma^\mu \Pi_\mu)^2)s} (m - \gamma^\mu \Pi_\mu) \tag{2.51}$$

Inserting (2.51) in (2.39) instead of the previously used (2.43) results in

$$\delta W^{(1)} = -i \operatorname{Tr} \delta(\gamma^\mu \Pi_\mu + m) (m - \gamma^\mu \Pi_\mu) i \int_0^\infty ds e^{-i(m^2 - (\gamma^\mu \Pi_\mu)^2)s}$$

## 2. State of the art

$$\begin{aligned}
&= \text{Tr} \delta(\gamma^\mu \Pi_\mu) (m - \gamma^\mu \Pi_\mu) \int_0^\infty ds e^{-i(m^2 - (\gamma^\mu \Pi_\mu)^2)s} \\
&\stackrel{*}{=} \text{Tr} \delta(\gamma^\mu \Pi_\mu) (-\gamma^\mu \Pi_\mu) \int_0^\infty ds e^{-i(m^2 - (\gamma^\mu \Pi_\mu)^2)s} \\
&= \text{Tr} \int_0^\infty ds \delta(\gamma^\mu \Pi_\mu) (-\gamma^\mu \Pi_\mu) e^{-i(m^2 - (\gamma^\mu \Pi_\mu)^2)s} \\
&\stackrel{**}{=} \text{Tr} \int_0^\infty ds \frac{i}{2s} \delta(e^{-i(m^2 - (\gamma^\mu \Pi_\mu)^2)s}) \\
&= \delta \left( \frac{i}{2} \text{Tr} \int_0^\infty ds s^{-1} e^{-i(m^2 - (\gamma^\mu \Pi_\mu)^2)s} \right). \tag{2.52}
\end{aligned}$$

Line (\*) is due to the fact that traces over odd powers of  $\gamma^\mu$  disappear and (\*\*) can be obtained by repeated use of the chain rule

$$\begin{aligned}
\frac{i}{2s} \delta(e^{-i(m^2 - (\gamma^\mu \Pi_\mu)^2)s}) &= \frac{i}{2s} (-is) \delta(m^2 - (\gamma^\mu \Pi_\mu)^2) e^{-i(m^2 - (\gamma^\mu \Pi_\mu)^2)s} \\
&= \frac{i}{2s} (-is) \delta(-(\gamma^\mu \Pi_\mu)^2) e^{-i(m^2 - (\gamma^\mu \Pi_\mu)^2)s} \\
&= \frac{i}{2s} (-is) 2(-\gamma^\mu \Pi_\mu) \delta(\gamma^\mu \Pi_\mu) e^{-i(m^2 - (\gamma^\mu \Pi_\mu)^2)s} \\
&= (-\gamma^\mu \Pi_\mu) \delta(\gamma^\mu \Pi_\mu) e^{-i(m^2 - (\gamma^\mu \Pi_\mu)^2)s}. \tag{2.53}
\end{aligned}$$

By the same rational as before the Lagrangian  $\mathcal{L}^{(1)}$  is obtained

$$\begin{aligned}
\mathcal{L}^{(1)}(\mathbf{x}) &= \frac{i}{2} \langle \mathbf{x} | \text{tr} \int_0^\infty ds s^{-1} e^{-i(m^2 - (\gamma^\mu \Pi_\mu)^2)s} | \mathbf{x} \rangle \\
&= \frac{i}{2} \int_0^\infty ds s^{-1} \langle \mathbf{x} | \text{tr} e^{-i(m^2 - (\gamma^\mu \Pi_\mu)^2)s} | \mathbf{x} \rangle \\
&= \frac{i}{2} \int_0^\infty ds s^{-1} \langle \mathbf{x} | \text{tr} e^{-im^2s} e^{i(\gamma^\mu \Pi_\mu)^2s} | \mathbf{x} \rangle \\
&= \frac{i}{2} \int_0^\infty ds \frac{e^{-im^2s}}{s} \text{tr} \langle \mathbf{x} | \underbrace{e^{i(\gamma^\mu \Pi_\mu)^2s}}_{U(s)} | \mathbf{x} \rangle. \tag{2.54}
\end{aligned}$$

Formulation (2.54) shows that the evaluation of the Lagrangian and the Green's function mainly depend on the evaluation of the operator  $U(s)$ . Due to its form it is easy to write  $U(s)$  as a classic time evolution operator, where

$$U(s) = e^{-i\mathcal{H}s}, \quad \mathcal{H} = -(\gamma^\mu \Pi_\mu)^2, \tag{2.55}$$

where  $\mathcal{H}$  has the properties of a Hamiltonian. Applying  $U(s)$  to a state  $|\mathbf{x}\rangle$  yields

$$U^\dagger(s) |\mathbf{x}\rangle = U^\dagger(s) |\mathbf{x}(0)\rangle = |\mathbf{x}(s)\rangle. \tag{2.56}$$

## 2.2. Schwinger's proper time formalism

The strong resemblance of this formulation to the classical time evolution formulas motivates the definition of  $s$  as a *proper time* parameter. Note, that it transforms the original problem into one where the space-time coordinates of the particles evolve with of  $s$ .

The governing ‘‘Hamiltonian’’  $\mathcal{H}$  of this proper time evolution can be rewritten as

$$\begin{aligned}
\mathcal{H} &= -(\gamma^\mu \Pi_\mu)^2 = -\gamma^\mu \Pi_\mu \gamma^\nu \Pi_\nu = -\gamma^\mu \gamma^\nu \Pi_\mu \Pi_\nu \\
&= -\frac{1}{2}\{\gamma^\mu, \gamma^\nu\} \Pi_\mu \Pi_\nu - \frac{1}{2}[\gamma^\mu, \gamma^\nu] \Pi_\mu \Pi_\nu \\
&= \frac{1}{2}2g^{\mu\nu} \Pi_\mu \Pi_\nu - \frac{1}{i}\sigma^{\mu\nu} \Pi_\mu \Pi_\nu = \Pi^\mu \Pi_\mu + \frac{i}{2}(\sigma^{\mu\nu} \Pi_\mu \Pi_\nu + \sigma^{\nu\mu} \Pi_\nu \Pi_\mu) \\
&= \Pi^\mu \Pi_\mu + \frac{i}{2}(\sigma^{\mu\nu} \Pi_\mu \Pi_\nu - \sigma^{\mu\nu} \Pi_\nu \Pi_\mu) = \Pi^\mu \Pi_\mu + \frac{i}{2}\sigma^{\mu\nu} [\Pi_\mu, \Pi_\nu] \\
&= \Pi^\mu \Pi_\mu + \frac{i}{2}\sigma^{\mu\nu} i e F_{\mu\nu} = \Pi^\mu \Pi_\mu - \frac{e}{2}\sigma^{\mu\nu} F_{\mu\nu}, \tag{2.57}
\end{aligned}$$

where  $\sigma$  is defined as

$$\sigma^{\mu\nu} = \frac{i}{2}[\gamma^\mu, \gamma^\nu]. \tag{2.58}$$

In the original paper by Schwinger [9] a different Clifford-Algebra-Relation is used then the one introduced in (2.6), this however does not influence the result. In analogy to the usual quantum mechanic time evolution [16], the equations of motion for the space time coordinates are given by

$$\begin{aligned}
\frac{dx_\mu}{ds} &= -i[x_\mu, \mathcal{H}] = -i[x_\mu, \Pi^\xi \Pi_\xi - \frac{e}{2}\sigma^{\xi\nu} F_{\xi\nu}] \\
&= -i[x_\mu, \Pi^\xi \Pi_\xi] = -i\Pi^\xi [x_\mu, \Pi_\xi] - i[x_\mu, \Pi^\xi] \Pi_\xi \\
&= -i\Pi^\xi (i\delta_{\mu\xi}) - i(i\delta_{\mu\tau} g^{\tau\xi}) \Pi_\xi \\
&= \Pi_\mu + \Pi_\mu = 2\Pi_\mu, \tag{2.59}
\end{aligned}$$

$$\begin{aligned}
\frac{d\Pi_\mu}{ds} &= -i[\Pi_\mu, \mathcal{H}] = -i[\Pi_\mu, \Pi^\xi \Pi_\xi - \frac{e}{2}\sigma^{\xi\nu} F_{\xi\nu}] \\
&= -i[\Pi_\mu, \Pi^\xi \Pi_\xi] + i[\Pi_\mu, \frac{e}{2}\sigma^{\xi\nu} F_{\xi\nu}] \\
&= -i\Pi^\xi [\Pi_\mu, \Pi_\xi] - i[\Pi_\mu, \Pi^\xi] \Pi_\xi + \frac{ie}{2}\sigma^{\xi\nu} [\Pi_\mu, F_{\xi\nu}] \\
&= -i\Pi^\xi (ieF_{\mu\xi}) - i(ieF_\mu{}^\xi) \Pi_\xi + \frac{ie}{2}\sigma^{\xi\nu} [-i\partial_\mu - eA_\mu(\mathbf{x}), F_{\xi\nu}] \\
&= e\{\Pi^\xi, F_{\mu\xi}\} + \frac{ie}{2}\sigma^{\xi\nu} [-i\partial_\mu, F_{\xi\nu}] \\
&= 2eF_{\mu\xi} \Pi^\xi - e[F_{\mu\xi}, \Pi^\xi] + \frac{e}{2}\sigma^{\xi\nu} \partial_\mu (F_{\xi\nu}) \\
&= 2eF_{\mu\xi} \Pi^\xi - ie\partial_\nu (F_{\mu\xi}) g^{\nu\xi} + \frac{e}{2}\sigma^{\xi\nu} \partial_\mu (F_{\xi\nu}). \tag{2.60}
\end{aligned}$$

## 2. State of the art

The Schrödinger equation becomes

$$i\partial_s \langle \mathbf{x}_i(s) | \mathbf{x}_f(0) \rangle = \langle \mathbf{x}_i(s) | \mathcal{H} | \mathbf{x}_f(0) \rangle . \quad (2.61)$$

Furthermore, the application of the proper time evolved momentum operator  $\Pi$  yields

$$(-i\partial_\mu^i - eA_\mu(\mathbf{x}_i)) \langle \mathbf{x}_i(s) | \mathbf{x}_f(0) \rangle = \langle \mathbf{x}_i(s) | \Pi_\mu(s) | \mathbf{x}_f(0) \rangle , \quad (2.62)$$

$$(i\partial_\mu^f - eA_\mu(\mathbf{x}_f)) \langle \mathbf{x}_i(s) | \mathbf{x}_f(0) \rangle = \langle \mathbf{x}_i(s) | \Pi_\mu(0) | \mathbf{x}_f(0) \rangle , \quad (2.63)$$

where  $\partial_\mu^k$  means  $\partial/\partial(\mathbf{x}_k)_\mu$  for  $k \in \{i, f\}$ . Last but not least,

$$\lim_{s \rightarrow 0} U(s) = \mathbb{1} \quad (2.64)$$

implies that

$$\lim_{s \rightarrow 0} \langle \mathbf{x}_i(s) | \mathbf{x}_f(0) \rangle = \delta^{(4)}(\mathbf{x}_i - \mathbf{x}_f) . \quad (2.65)$$

### 2.2.1. The zero field case

In order to exemplify the workings of the proper time formalism, the derivation of the Green's function and Lagrangian is presented for the case where  $F_{\mu\nu} = 0$ . In this case the equations of motion become

$$\frac{d\Pi_\mu}{ds} = 0, \quad \frac{dx_\mu}{ds} = 2\Pi_\mu . \quad (2.66)$$

By the fundamental theorem of calculus it is obtained that

$$\Pi_\mu(s) - \Pi_\mu(0) = \int_0^s ds' \frac{d\Pi_\mu}{ds'} = \int_0^s ds' 0 = 0 \quad (2.67)$$

and thus

$$\Pi_\mu(s) = \Pi_\mu(0) . \quad (2.68)$$

An analogous computation for  $x_\mu$  yields

$$x_\mu(s) - x_\mu(0) = \int_0^s ds' \frac{dx_\mu}{ds'} = \int_0^s ds' (2\Pi_\mu(s')) = \int_0^s ds' 2\Pi_\mu(0) = 2s\Pi_\mu(0) , \quad (2.69)$$

which solved for  $\Pi_0$  turns into

$$\Pi_\mu(0) = \frac{1}{2s}(x_\mu(s) - x_\mu(0)) . \quad (2.70)$$

## 2.2. Schwinger's proper time formalism

Plugging (2.70) into (2.57) results in the expression

$$\begin{aligned}
\mathcal{H} &= \Pi_\mu \Pi^\mu = \frac{1}{4s^2} (x_\mu(s) - x_\mu(0))(x^\mu(s) - x^\mu(0)) \\
&= \frac{1}{4s^2} (x_\mu(s)x^\mu(s) - 2x_\mu(s)x^\mu(0) + x_\mu(0)x^\mu(0)) + \frac{1}{4s^2} [x_\mu(s), x^\mu(0)] \\
&= \frac{1}{4s^2} (x_\mu(s)x^\mu(s) - 2x_\mu(s)x^\mu(0) + x_\mu(0)x^\mu(0)) \\
&\quad + \frac{1}{4s^2} [x_\mu(0) + 2s\Pi_\mu(0), x^\mu(0)] \\
&= \frac{1}{4s^2} (x_\mu(s)x^\mu(s) - 2x_\mu(s)x^\mu(0) + x_\mu(0)x^\mu(0)) + \frac{1}{2s} [\Pi_\mu(0), x^\mu(0)] \\
&= \frac{1}{4s^2} (x_\mu(s)x^\mu(s) - 2x_\mu(s)x^\mu(0) + x_\mu(0)x^\mu(0)) + \frac{-i}{2s} \delta_{\mu\xi} g^{\xi\mu} \\
&= \frac{1}{4s^2} (x_\mu(s)x^\mu(s) - 2x_\mu(s)x^\mu(0) + x_\mu(0)x^\mu(0)) - \frac{2i}{s}. \tag{2.71}
\end{aligned}$$

Using this relation in (2.61) results in the differential equation

$$\begin{aligned}
i\partial_s \langle \mathbf{x}_i(s) | \mathbf{x}_f(0) \rangle &= \langle \mathbf{x}_i(s) | \mathcal{H} | \mathbf{x}_f(0) \rangle \\
&= \langle \mathbf{x}_i(s) | \left( \frac{1}{4s^2} (x_\mu(s)x^\mu(s) - 2x_\mu(s)x^\mu(0) + x_\mu(0)x^\mu(0)) - \frac{2i}{s} \right) | \mathbf{x}_f(0) \rangle \\
&= \left( \frac{1}{4s^2} (x_{i\mu}x_i^\mu - 2x_{i\mu}x_f^\mu + x_{f\mu}x_f^\mu) - \frac{2i}{s} \right) \langle \mathbf{x}_i(s) | \mathbf{x}_f(0) \rangle \\
&= \left( \frac{1}{4s^2} (x_{i\mu} - x_{f\mu})(x_i^\mu - x_f^\mu) - \frac{2i}{s} \right) \langle \mathbf{x}_i(s) | \mathbf{x}_f(0) \rangle \\
&= \left( \frac{1}{4s^2} \Delta x_\mu \Delta x^\mu - \frac{2i}{s} \right) \langle \mathbf{x}_i(s) | \mathbf{x}_f(0) \rangle. \tag{2.72}
\end{aligned}$$

It can be solved using an integrating factor:

$$\langle \mathbf{x}_i(s) | \mathbf{x}_f(0) \rangle = C(\mathbf{x}_i, \mathbf{x}_f) s^{-2} e^{\frac{i}{4s} \Delta x_\mu \Delta x^\mu}. \tag{2.73}$$

The validity of this solution is easily verified by performing the differentiation

$$\begin{aligned}
i\frac{\partial}{\partial s} C(\mathbf{x}_i, \mathbf{x}_f) s^{-2} e^{\frac{i}{4s} \Delta x_\mu \Delta x^\mu} &= iC(\mathbf{x}_i, \mathbf{x}_f) \frac{\partial}{\partial s} s^{-2} e^{\frac{i}{4s} \Delta x_\mu \Delta x^\mu} \\
&= iC(\mathbf{x}_i, \mathbf{x}_f) \left( -2s^{-3} e^{\frac{i}{4s} \Delta x_\mu \Delta x^\mu} + s^{-2} e^{\frac{i}{4s} \Delta x_\mu \Delta x^\mu} \frac{\partial}{\partial s} \frac{i}{4s} \Delta x_\mu \Delta x^\mu \right) \\
&= iC(\mathbf{x}_i, \mathbf{x}_f) \left( -2s^{-3} e^{\frac{i}{4s} \Delta x_\mu \Delta x^\mu} - s^{-2} e^{\frac{i}{4s} \Delta x_\mu \Delta x^\mu} \frac{i}{4s^2} \Delta x_\mu \Delta x^\mu \right) \\
&= iC(\mathbf{x}_i, \mathbf{x}_f) s^{-2} \left( -2s^{-1} - \frac{i}{4s^2} \Delta x_\mu \Delta x^\mu \right) e^{\frac{i}{4s} \Delta x_\mu \Delta x^\mu}
\end{aligned}$$

## 2. State of the art

$$\begin{aligned}
&= i \left( -2s^{-1} - \frac{i}{4s^2} \Delta x_\mu \Delta x^\mu \right) \langle \mathbf{x}_i(s) | \mathbf{x}_f(0) \rangle \\
&= \left( \frac{-2i}{s} + \frac{1}{4s^2} \Delta x_\mu \Delta x^\mu \right) \langle \mathbf{x}_i(s) | \mathbf{x}_f(0) \rangle .
\end{aligned} \tag{2.74}$$

The remaining function  $C(\mathbf{x}_i, \mathbf{x}_f)$  can then be computed by making use of the fact that

$$\langle \mathbf{x}_i(s) | \Pi_\mu(s) | \mathbf{x}_f(0) \rangle = \langle \mathbf{x}_i(s) | \Pi_\mu(0) | \mathbf{x}_f(0) \rangle \tag{2.75}$$

and therefore

$$(-i\partial_\mu^i - eA_\mu(\mathbf{x}_i))C(\mathbf{x}_i, \mathbf{x}_f) = (i\partial_\mu^f - eA_\mu(\mathbf{x}_f))C(\mathbf{x}_i, \mathbf{x}_f), \tag{2.76}$$

which can be solved by

$$C(\mathbf{x}_i, \mathbf{x}_f) = c\phi(\mathbf{x}_i, \mathbf{x}_f), \tag{2.77}$$

where  $c$  is a constant and

$$\phi(\mathbf{x}_i, \mathbf{x}_f) = e^{ie \int_{\mathbf{x}_f}^{\mathbf{x}_i} dx^\mu A_\mu(\mathbf{x})} = e^{-ie \int_{\mathbf{x}_i}^{\mathbf{x}_f} dx^\mu A_\mu(\mathbf{x})}. \tag{2.78}$$

Note, that the line integral in  $\phi$  is independent of the path chosen since  $F_{\mu\nu} = 0$  and therefore  $A(\mathbf{x})$  is curl free. The final unknown is fixed by the limit  $s \rightarrow 0$  (2.65) as

$$\delta(\mathbf{x}_i - \mathbf{x}_f) = \lim_{s \rightarrow 0} \langle \mathbf{x}_i(s) | \mathbf{x}_f(0) \rangle = \lim_{s \rightarrow 0} c s^{-2} e^{\frac{i}{4s} \Delta x_\mu \Delta x^\mu} e^{-ie \int_{\mathbf{x}_i}^{\mathbf{x}_f} dx^\mu A_\mu(\mathbf{x})}. \tag{2.79}$$

Integrating both sides over  $\mathbf{x} = \mathbf{x}_i - \mathbf{x}_f$  results in

$$1 = \lim_{s \rightarrow 0} c s^{-2} \int_{\mathbb{R}^4} d^4\mathbf{x} e^{\frac{i}{4s} x_\mu x^\mu}. \tag{2.80}$$

Performing the integration with  $d^4\mathbf{x} = \Pi_\mu \eta_{\mu\nu} dx^\nu$ , computing the limit and solving for  $c$  results in

$$c = -\frac{i}{16\pi^2} \tag{2.81}$$

and the complete solution thus becomes

$$\langle \mathbf{x}_i(s) | \mathbf{x}_f(0) \rangle = -\frac{i}{16\pi^2} s^{-2} e^{\frac{i}{4s} \Delta x_\mu \Delta x^\mu} e^{-ie \int_{\mathbf{x}_i}^{\mathbf{x}_f} dx^\mu A_\mu(\mathbf{x})}. \tag{2.82}$$

With the help of (2.82) the Green's function (2.51) now becomes

$$G(\mathbf{x}_i, \mathbf{x}_f) = i \int_0^\infty ds \langle \mathbf{x}_i | e^{-i(m^2 - (\gamma^\mu \Pi_\mu)^2)s} (m - \gamma^\mu \Pi_\mu) | \mathbf{x}_f \rangle$$

## 2.2. Schwinger's proper time formalism

$$\begin{aligned}
&= i \int_0^\infty ds \langle \mathbf{x}_i | e^{-im^2s} e^{-i(\gamma^\mu \Pi_\mu)^2s} (m - \gamma^\mu \Pi_\mu) | \mathbf{x}_f \rangle \\
&= i \int_0^\infty ds e^{-im^2s} \langle \mathbf{x}_i | e^{-i(\gamma^\mu \Pi_\mu)^2s} (m - \gamma^\mu \Pi_\mu) | \mathbf{x}_f \rangle \\
&= i \int_0^\infty ds e^{-im^2s} \langle \mathbf{x}_i(s) | (m - \gamma^\mu \Pi_\mu) | \mathbf{x}_f(0) \rangle \\
&= i \int_0^\infty ds e^{-im^2s} \langle \mathbf{x}_i(s) | \left( m - \gamma^\mu \frac{(x_\mu(s) - x_\mu(0))}{2s} \right) | \mathbf{x}_f(0) \rangle \\
&= i \int_0^\infty ds e^{-im^2s} \left( m - \gamma^\mu \frac{(\mathbf{x}_i - \mathbf{x}_f)}{2s} \right) \langle \mathbf{x}_i(s) | \mathbf{x}_f(0) \rangle \\
&= -\frac{i}{16\pi^2} e^{-ie \int_{\mathbf{x}_i}^{\mathbf{x}_f} dx^\mu A_\mu(\mathbf{x})} \\
&\quad \cdot \int_0^\infty ds e^{-im^2s} \left( m - \gamma^\mu \frac{(\mathbf{x}_i - \mathbf{x}_f)}{2s} \right) s^{-2} e^{\frac{i}{4s} \Delta x_\mu \Delta x^\mu}. \quad (2.83)
\end{aligned}$$

### 2.2.2. The Heisenberg-Euler Lagrangian

Let now

$$F_{\mu\nu} = \text{const.} \neq 0. \quad (2.84)$$

Then (2.59) and (2.60) take the form

$$\frac{dx_\mu}{ds} = 2\Pi_\mu, \quad \frac{d\Pi_\mu}{ds} = 2eF_{\mu\nu}\Pi^\nu \quad (2.85)$$

which in matrix notation may be written as

$$\frac{d\mathbf{x}}{ds} = 2\mathbf{\Pi}, \quad \frac{d\mathbf{\Pi}}{ds} = 2e\mathbf{F}\mathbf{\Pi}. \quad (2.86)$$

The equation for the momentum can be solved by using the integrating factor formulation

$$\mathbf{\Pi}(s) = e^{2e\mathbf{F}s} c, \quad (2.87)$$

where the constant  $c$  is determined by

$$\mathbf{\Pi}(0) = e^{2e\mathbf{F}0} c = e^0 c = \mathbb{1}c = c. \quad (2.88)$$

Since

$$\frac{d\mathbf{x}}{ds} = 2\mathbf{\Pi} = (e\mathbf{F})^{-1} 2e\mathbf{F}\mathbf{\Pi} = (e\mathbf{F})^{-1} \frac{d\mathbf{\Pi}}{ds}, \quad (2.89)$$

the solution for  $\mathbf{x}$  must fulfill

$$\mathbf{x}(s) - \mathbf{x}(0) = (e\mathbf{F})^{-1} (\mathbf{\Pi}(s) - \mathbf{\Pi}(0)), \quad (2.90)$$

## 2. State of the art

by virtue of the linearity of the differential operator. Inserting (2.88), (2.87) and solving for  $\mathbf{x}(s)$  yields

$$\mathbf{x}(s) = (e\mathbf{F})^{-1}(e^{2e\mathbf{F}s} - \mathbf{1})\mathbf{\Pi}(0) + \mathbf{x}(0). \quad (2.91)$$

Solving for  $\mathbf{\Pi}(0)$  results in

$$\begin{aligned} \mathbf{\Pi}(0) &= e\mathbf{F}(e^{2e\mathbf{F}s} - \mathbf{1})^{-1}(\mathbf{x}(s) - \mathbf{x}(0)) \\ &= e\mathbf{F}e^{-e\mathbf{F}s}(e^{e\mathbf{F}s} - e^{-e\mathbf{F}s})^{-1}(\mathbf{x}(s) - \mathbf{x}(0)) \\ &= e\mathbf{F}e^{-e\mathbf{F}s}\frac{1}{2}\sinh(e\mathbf{F}s)^{-1}(\mathbf{x}(s) - \mathbf{x}(0)) \\ &= \frac{1}{2}e\mathbf{F}e^{-e\mathbf{F}s}\sinh(e\mathbf{F}s)^{-1}(\mathbf{x}(s) - \mathbf{x}(0)), \end{aligned} \quad (2.92)$$

and solving for  $\mathbf{\Pi}(s)$

$$\begin{aligned} \mathbf{\Pi}(s) &= e^{2e\mathbf{F}s} \\ &= e^{2e\mathbf{F}s}\frac{1}{2}e\mathbf{F}e^{-e\mathbf{F}s}\sinh(e\mathbf{F}s)^{-1}(\mathbf{x}(s) - \mathbf{x}(0)) \\ &= \frac{1}{2}e\mathbf{F}e^{e\mathbf{F}s}\sinh(e\mathbf{F}s)^{-1}(\mathbf{x}(s) - \mathbf{x}(0)) \\ &= \frac{1}{2}(\mathbf{x}(s) - \mathbf{x}(0))^\top e\mathbf{F}e^{-e\mathbf{F}s}\sinh(e\mathbf{F}s)^{-1}, \end{aligned} \quad (2.93)$$

where the last transformation makes use of the fact that  $F_{\mu\nu} = -F_{\nu\mu}$  and thus  $\mathbf{x}^\top\mathbf{F} = -\mathbf{F}\mathbf{x}$ . The Hamiltonian now becomes

$$\begin{aligned} \mathcal{H} + \frac{e}{2}\sigma^{\mu\nu}F_{\mu\nu} \\ &= \mathbf{\Pi}^2(s) = (\mathbf{x}(s) - \mathbf{x}(0))^\top \frac{1}{4}e^2\mathbf{F}^2\sinh(e\mathbf{F}s)^{-2}(\mathbf{x}(s) - \mathbf{x}(0)) \\ &= \mathbf{x}^\top(s)\mathbf{K}\mathbf{x}(s) - 2\mathbf{x}^\top(s)\mathbf{K}\mathbf{x}(0) + \mathbf{x}^\top(0)\mathbf{K}\mathbf{x}(0) + [x_\mu(s), x_\nu(0)]K^{\mu\nu} \\ &= \square, \end{aligned}$$

which with

$$\begin{aligned} [x_\mu(s), x_\nu(0)] &= [x_\mu(0) + (e\mathbf{F})^{-1}(e^{2e\mathbf{F}s} - \mathbf{1})|_{\mu\xi}\mathbf{\Pi}^\xi(0), x_\nu(0)] \\ &= (e\mathbf{F})^{-1}(e^{2e\mathbf{F}s} - \mathbf{1})|_{\mu\xi}[\mathbf{\Pi}^\xi(0), x_\nu(0)] \\ &= (e\mathbf{F})^{-1}(e^{2e\mathbf{F}s} - \mathbf{1})|_{\mu\xi}(-i)\delta^\xi_\nu \\ &= -i(e\mathbf{F})^{-1}(e^{2e\mathbf{F}s} - \mathbf{1})|_{\mu\nu}, \end{aligned} \quad (2.94)$$

can be rewritten as

$$\square = \mathbf{x}^\top(s)\mathbf{K}\mathbf{x}(s) - 2\mathbf{x}^\top(s)\mathbf{K}\mathbf{x}(0) + \mathbf{x}^\top(0)\mathbf{K}\mathbf{x}(0) - i(e\mathbf{F})^{-1}(e^{2e\mathbf{F}s} - \mathbf{1})|_{\mu\nu}K^{\mu\nu}$$

## 2.2. Schwinger's proper time formalism

$$\begin{aligned}
&\stackrel{sym}{=} \mathbf{x}^\top(s)\mathbf{K}\mathbf{x}(s) - 2\mathbf{x}^\top(s)\mathbf{K}\mathbf{x}(0) + \mathbf{x}^\top(0)\mathbf{K}\mathbf{x}(0) - i\text{tr}(e\mathbf{F})^{-1}(e^{2e\mathbf{F}s} - \mathbf{1})\mathbf{K} \\
&= -'' - i\text{tr}\left[(e\mathbf{F})^{-1}(e^{2e\mathbf{F}s} - \mathbf{1})\frac{1}{4}e^2\mathbf{F}^2\sinh(e\mathbf{F}s)^{-2}\right] \\
&= -'' - \frac{i}{4}\text{tr}\left[e\mathbf{F}e^{e\mathbf{F}s}(e^{e\mathbf{F}s} - e^{-e\mathbf{F}s})\sinh(e\mathbf{F}s)^{-2}\right] \\
&= -'' - \frac{i}{2}\text{tr}\left[e\mathbf{F}e^{e\mathbf{F}s}\sinh(e\mathbf{F}s)^{-1}\right] \\
&= -'' - \frac{i}{2}\text{tr}\left[e\mathbf{F}\frac{2}{e^{2e\mathbf{F}s} - \mathbf{1}}\right] \\
\stackrel{\text{tr}\mathbf{F}=0}{=} &= -'' - \frac{i}{2}\text{tr}\left[e\mathbf{F}\frac{2}{e^{2e\mathbf{F}s} - \mathbf{1}} + e\mathbf{F}\right] \\
&= \mathbf{x}^\top(s)\mathbf{K}\mathbf{x}(s) - 2\mathbf{x}^\top(s)\mathbf{K}\mathbf{x}(0) + \mathbf{x}^\top(0)\mathbf{K}\mathbf{x}(0) - \frac{i}{2}\text{tr}[e\mathbf{F}\coth(e\mathbf{F}s)]. \quad (2.95)
\end{aligned}$$

Inserting this into (2.61) yields

$$\begin{aligned}
i\partial_s\langle\mathbf{x}_i(s)|\mathbf{x}_f(0)\rangle &= \langle\mathbf{x}_i(s)|\mathcal{H}|\mathbf{x}_f(0)\rangle \\
&= \left[-\frac{e}{2}\sigma^{\mu\nu}F_{\mu\nu} + \frac{e^2}{4}\Delta\mathbf{x}^\top\mathbf{F}^2\sinh(e\mathbf{F}s)^{-2}\Delta\mathbf{x} - \frac{i}{2}\text{tr}e\mathbf{F}\coth(e\mathbf{F}s)\right]. \quad (2.96)
\end{aligned}$$

The differential equation is solved using an integration factor. The solution becomes

$$\langle\mathbf{x}_i(s)|\mathbf{x}_f(0)\rangle = C(\mathbf{x}_i, \mathbf{x}_f) e^{\frac{ie}{2}\sigma^{\mu\nu}F_{\mu\nu}s} e^{\frac{i}{4}\Delta\mathbf{x}^\top e\mathbf{F}\coth(e\mathbf{F}s)\Delta\mathbf{x}} e^{-L(s)}s^{-2}, \quad (2.97)$$

where

$$L(s) = \frac{1}{2}\text{tr}\ln[(e\mathbf{F}s)^{-1}\sinh(e\mathbf{F}s)]. \quad (2.98)$$

The remaining integration constant can now be determined using (2.62), (2.63) and (2.65). To do that, first the equations (2.92) and (2.93) are rewritten as

$$\begin{aligned}
\Pi(0) &= \frac{1}{2}e\mathbf{F}e^{-e\mathbf{F}s}\sinh(e\mathbf{F}s)^{-1}(\mathbf{x}(s) - \mathbf{x}(0)) \\
&= e\mathbf{F}\frac{1}{e^{2e\mathbf{F}s} - \mathbf{1}}(\mathbf{x}(s) - \mathbf{x}(0)) \\
&= e\mathbf{F}\left[-\frac{1}{2} + \frac{1}{2}\left(1 + \frac{1}{e^{e\mathbf{F}s} - \mathbf{1}}\right)\right](\mathbf{x}(s) - \mathbf{x}(0)) \\
&= e\mathbf{F}\left[-\frac{1}{2} + \frac{1}{2}\coth(2e\mathbf{F}s)\right](\mathbf{x}(s) - \mathbf{x}(0)), \quad (2.99)
\end{aligned}$$

$$\Pi(s) = \frac{1}{2}e\mathbf{F}e^{e\mathbf{F}s}\sinh(e\mathbf{F}s)^{-1}(\mathbf{x}(s) - \mathbf{x}(0))$$

2. *State of the art*

$$\stackrel{s.a.}{=} e\mathbf{F} \left[ \frac{1}{2} + \frac{1}{2} \coth(e\mathbf{F}s) \right] (\mathbf{x}(s) - \mathbf{x}(0)). \quad (2.100)$$

Inserting (2.99) and (2.100) into (2.63) results in

$$\begin{aligned} & (i\partial_\mu^f - eA_\mu(\mathbf{x}_f)) \langle \mathbf{x}_i(s) | \mathbf{x}_f(0) \rangle \\ &= -i(\partial_\mu^f C(\mathbf{x}_i, \mathbf{x}_f)) \frac{\langle \mathbf{x}_i(s) | \mathbf{x}_f(0) \rangle}{C(\mathbf{x}_i, \mathbf{x}_f)} + \frac{1}{2} e\mathbf{F} \coth(e\mathbf{F}s) |_\mu^\nu \Delta x_\nu \langle \mathbf{x}_i(s) | \mathbf{x}_f(0) \rangle \\ &\quad - eA_\mu(\mathbf{x}_f) \langle \mathbf{x}_i(s) | \mathbf{x}_f(0) \rangle \\ &\stackrel{!}{=} \langle \mathbf{x}_i(s) | \Pi_\mu(s) | \mathbf{x}_f(0) \rangle \\ &= \left[ \frac{1}{2} e\mathbf{F} + \frac{1}{2} e\mathbf{F} \coth(e\mathbf{F}s) \right] |_\mu^\nu \Delta x_\nu \langle \mathbf{x}_i(s) | \mathbf{x}_f(0) \rangle \end{aligned} \quad (2.101)$$

and thus

$$-i\partial_\mu^f C(\mathbf{x}_i, \mathbf{x}_f) - \frac{1}{2} eF_{\mu\nu} \Delta x^\nu C(\mathbf{x}_i, \mathbf{x}_f) - eA_\mu(\mathbf{x}_f) C(\mathbf{x}_i, \mathbf{x}_f) = 0. \quad (2.102)$$

Doing the same with (2.62) ends in

$$i\partial_\mu^i C(\mathbf{x}_i, \mathbf{x}_f) - \frac{1}{2} eF_{\mu\nu} \Delta x^\nu C(\mathbf{x}_i, \mathbf{x}_f) - eA_\mu(\mathbf{x}_i) C(\mathbf{x}_i, \mathbf{x}_f) = 0. \quad (2.103)$$

Equations (2.102) and (2.103) can then be solved using an integration factor

$$C(\mathbf{x}_i, \mathbf{x}_f) = ce^{ie \int_{\mathbf{x}_i}^{\mathbf{x}_f} dx^\mu (A_\mu(\mathbf{x}) + \frac{1}{2} F_{\mu\nu} (x^\nu - x_i^\nu))}. \quad (2.104)$$

As the field is constant and as such has a vanishing curl, the integration path in the equation (2.104) may be chosen freely. Selecting it to be a straight line between  $\mathbf{x}_i$  and  $\mathbf{x}_f$  causes the  $F_{\mu\nu}$  contribution to vanish due to symmetry and as such the solution becomes

$$C(\mathbf{x}_i, \mathbf{x}_f) = c\phi(\mathbf{x}_i, \mathbf{x}_f), \quad (2.105)$$

where  $c$  is a constant and

$$\phi(\mathbf{x}_i, \mathbf{x}_f) = e^{ie \int_{\mathbf{x}_f}^{\mathbf{x}_i} dx^\mu A_\mu(\mathbf{x})} = e^{-ie \int_{\mathbf{x}_i}^{\mathbf{x}_f} dx^\mu A_\mu(\mathbf{x})}. \quad (2.106)$$

Note, that (2.106) has the same form as for the zero background case. As such the constant  $c$  determined by the requirement of continuity of  $U(s)$  becomes

$$c = -\frac{i}{16\pi^2} \quad (2.107)$$

The closed expression for  $\langle \mathbf{x}_i(s) | \mathbf{x}_f(0) \rangle$  thus becomes

$$\langle \mathbf{x}_i(s) | \mathbf{x}_f(0) \rangle$$

## 2.2. Schwinger's proper time formalism

$$= -\frac{i}{16\pi^2} e^{-ie \int_{\mathbf{x}_i}^{\mathbf{x}_f} dx^\mu A_\mu(\mathbf{x})} e^{\frac{ie}{2} \sigma^{\mu\nu} F_{\mu\nu} s} e^{\frac{i}{4} \Delta \mathbf{x}^\top e \mathbf{F} \coth(e \mathbf{F} s) \Delta \mathbf{x}} e^{-L(s)} s^{-2} \quad (2.108)$$

The Green's function and Lagrangian are once again given by

$$G(\mathbf{x}_i, \mathbf{x}_f) = i \int_0^\infty ds e^{-im^2 s} (m \langle \mathbf{x}_i(s) | \mathbf{x}_f(0) \rangle - \gamma^\mu \langle \mathbf{x}_i(s) | \Pi_\mu(0) | \mathbf{x}_f(0) \rangle) \quad (2.109)$$

or

$$G(\mathbf{x}_i, \mathbf{x}_f) = i \int_0^\infty ds e^{-im^2 s} (m \langle \mathbf{x}_i(s) | \mathbf{x}_f(0) \rangle + \gamma^\mu \langle \mathbf{x}_i(s) | \Pi_\mu(s) | \mathbf{x}_f(0) \rangle) \quad (2.110)$$

and

$$\begin{aligned} \mathcal{L}^{(1)}(\mathbf{x}) &= \frac{i}{2} \int_0^\infty ds \frac{e^{-im^2 s}}{s} \text{tr} \langle \mathbf{x}_i(s) | \mathbf{x}_f(0) \rangle \Big|_{\mathbf{x}_i, \mathbf{x}_f \rightarrow \mathbf{x}} \\ &= \frac{i}{2} \int_0^\infty ds \frac{e^{-im^2 s}}{s} \text{tr} \left( -\frac{i}{16\pi^2} e^{\frac{ie}{2} \sigma^{\mu\nu} F_{\mu\nu} s} e^{-L(s)} s^{-2} \right) \\ &= \frac{1}{32\pi^2} \int_0^\infty ds \frac{e^{-im^2 s}}{s^3} e^{-L(s)} \text{tr} e^{\frac{ie}{2} \sigma^{\mu\nu} F_{\mu\nu} s} \\ &= \frac{-1}{32\pi^2} \int_0^\infty ds \frac{e^{-m^2 s}}{s^3} e^{-l(s)} \text{tr} e^{\frac{e}{2} \sigma^{\mu\nu} F_{\mu\nu} s}, \end{aligned} \quad (2.111)$$

where the last line in (2.111) is simply a deformation of the integration path and

$$l(s) = \frac{1}{2} \text{tr} \ln[(e \mathbf{F} s)^{-1} \sin(e \mathbf{F} s)]. \quad (2.112)$$

From the definition of the  $\sigma$  matrices given by (2.58) it follows that

$$\frac{1}{2} \{\sigma_{\mu\nu}, \sigma_{\lambda\kappa}\} = \delta_{\mu\lambda} \delta_{\nu\kappa} - \delta_{\mu\kappa} \delta_{\nu\lambda} - i \varepsilon_{\mu\nu\lambda\kappa} \gamma_5, \quad (2.113)$$

where

$$\gamma_5 = i\gamma_0\gamma_1\gamma_2\gamma_3, \quad (\gamma_5)^2 = \mathbf{1}, \quad (2.114)$$

and

$$\varepsilon_{\mu\nu\lambda\kappa} = \begin{cases} 1 & , \text{ for } (\mu\nu\lambda\kappa) \text{ even permutation of } (0123) \\ -1 & , \text{ for } (\mu\nu\lambda\kappa) \text{ odd permutation of } (0123) \\ 0 & , \text{ else} \end{cases}. \quad (2.115)$$

With the help of (2.115) the dual field tensor may be written as

$$F_{\mu\nu}^* = \frac{1}{2} \varepsilon_{\mu\nu\lambda\kappa} F^{\lambda\kappa}. \quad (2.116)$$

## 2. State of the art

Using (2.113) and (2.116) the expression  $(\frac{1}{2}\sigma_{\mu\nu}\mathcal{F}^{\mu\nu})^2$  takes on the form

$$\begin{aligned}
\left(\frac{1}{2}\sigma_{\mu\nu}F^{\mu\nu}\right)^2 &= \frac{1}{4}\sigma_{\mu\nu}F^{\mu\nu}\sigma_{\tilde{\mu}\tilde{\nu}}F^{\tilde{\mu}\tilde{\nu}} \\
&= \frac{1}{8}(\sigma_{\mu\nu}\sigma_{\tilde{\mu}\tilde{\nu}} + \sigma_{\tilde{\mu}\tilde{\nu}}\sigma_{\mu\nu})F^{\mu\nu}F^{\tilde{\mu}\tilde{\nu}} \\
&= \frac{1}{4}(\delta_{\mu\tilde{\mu}}\delta_{\nu\tilde{\nu}} - \delta_{\mu\tilde{\nu}}\delta_{\nu\tilde{\mu}} - i\varepsilon_{\mu\nu\tilde{\mu}\tilde{\nu}}\gamma_5)F^{\mu\nu}F^{\tilde{\mu}\tilde{\nu}} \\
&= \frac{1}{4}(F^{\mu\nu}F_{\mu\nu} - F^{\mu\nu}F_{\nu\mu} - iF^{\mu\nu}\varepsilon_{\mu\nu\tilde{\mu}\tilde{\nu}}\gamma_5F^{\tilde{\mu}\tilde{\nu}}) \\
&= \frac{1}{4}(F^{\mu\nu}F_{\mu\nu} + F^{\mu\nu}F_{\mu\nu} - 2i\gamma_5F^{\mu\nu}F_{\mu\nu}^*) \\
&= \frac{1}{2}F^{\mu\nu}F_{\mu\nu} - i\gamma_5F^{\mu\nu}F_{\mu\nu}^*. \tag{2.117}
\end{aligned}$$

Defining the *electromagnetic invariants*  $\mathcal{F}$  and  $\mathcal{G}$  as

$$\mathcal{F} = \frac{1}{4}F^{\mu\nu}F_{\mu\nu} = \frac{1}{2}(\vec{E}^2 - \vec{B}^2), \quad \mathcal{G} = -\frac{1}{4}F^{\mu\nu}F_{\mu\nu}^* = \vec{E} \cdot \vec{B} \tag{2.118}$$

and combining them with the equation (2.117) results in

$$\left(\frac{1}{2}\sigma_{\mu\nu}F^{\mu\nu}\right)^2 = 2(\mathcal{F} + i\gamma_5\mathcal{G}). \tag{2.119}$$

As both sides of (2.119) have to share eigenvectors and eigenvalues and as stated in (2.114)  $\gamma_5^2 = 1$  it follows that

$$\text{Eig} \left[ \left( \frac{1}{2}\sigma_{\mu\nu}F^{\mu\nu} \right)^2 \right] = 2 \text{Eig}(\mathcal{F} + i\gamma_5\mathcal{G}) = 2(\mathcal{F} \pm i\mathcal{G}) \tag{2.120}$$

and thus

$$\text{Eig} \left[ \frac{1}{2}\sigma_{\mu\nu}F^{\mu\nu} \right] = \pm \sqrt{2(\mathcal{F} \pm i\mathcal{G})}. \tag{2.121}$$

The right hand side of (2.121) can then be rewritten in terms of the *secular invariants*

$$a = \sqrt{\sqrt{\mathcal{F}^2 - \mathcal{G}^2} - \mathcal{F}}, \tag{2.122}$$

$$b = \sqrt{\sqrt{\mathcal{F}^2 - \mathcal{G}^2} + \mathcal{F}}, \tag{2.123}$$

where

$$(b \pm ia)^2 = b^2 - a^2 \pm 2iab$$

## 2.2. Schwinger's proper time formalism

$$\begin{aligned}
&= 2\mathcal{F} \pm 2i\sqrt{(\mathcal{F}^2 - \mathcal{G}^2) - \mathcal{F}^2} \\
&= 2(\mathcal{F} \mp i\mathcal{G})
\end{aligned} \tag{2.124}$$

and therefore

$$\text{Eig} \left[ \frac{1}{2} \sigma_{\mu\nu} F^{\mu\nu} \right] = \pm(b \pm ia). \tag{2.125}$$

Now, since the trace of an operator is equal to the sum of its eigenvalues it is found that

$$\begin{aligned}
\text{tr} e^{\frac{e}{2} \sigma^{\mu\nu} F_{\mu\nu} s} &= \sum_{x \in \text{Eig}[e^{\frac{e}{2} \sigma^{\mu\nu} F_{\mu\nu} s}]} x = \sum_{x \in \text{Eig}[\frac{1}{2} \sigma_{\mu\nu} F^{\mu\nu}]} e^{esx} \\
&= e^{es(b+ia)} + e^{-es(b+ia)} + e^{es(b-ia)} + e^{-es(b-ia)} \\
&= 2 \cosh(es(b+ia)) + 2 \cosh(es(b-ia)) \\
&= 2 \cosh(esb) \cosh(iesa) + 2 \sinh(esb) \sinh(iesa) \\
&\quad + 2 \cosh(esb) \cosh(iesa) - 2 \sinh(esb) \sinh(iesa) \\
&= 4 \cosh(esb) \cosh(iesa) = 4 \cosh(esb) \cos(esa).
\end{aligned} \tag{2.126}$$

To compute the trace in (2.112), the eigenvalues of  $\mathcal{F} = (F_{\mu\nu})^2/4$  are required. Starting with the relations

$$F_{\mu\lambda} F^{*\lambda\nu} = -\delta_{\mu}^{\nu} \mathcal{G} \tag{2.127}$$

and

$$F_{\mu\lambda}^* F^{*\lambda\nu} - F_{\mu\lambda} F^{\lambda\nu} = 2\delta_{\mu}^{\nu} \mathcal{F}, \tag{2.128}$$

it is found, that if  $f \in \text{Eig}[\mathcal{F}]$ , i.e.,

$$F^{\mu\nu} \psi_{\nu} = f \psi^{\mu}, \tag{2.129}$$

then

$$F^{*\mu\nu} \psi_{\nu} = \frac{-\mathcal{G}}{f} \psi^{\mu} \tag{2.130}$$

and therefore

$$F_{\mu\lambda}^* F^{*\lambda\nu} \psi_{\nu} = \frac{\mathcal{G}^2}{f^2} \psi_{\mu}, \quad F_{\mu\lambda} F^{\lambda\nu} \psi_{\nu} = f^2 \psi_{\mu}. \tag{2.131}$$

Combining (2.131) with (2.128), it follows

$$\begin{aligned}
&\left( \frac{\mathcal{G}^2}{f^2} - f^2 \right) \psi_{\mu} = 2\mathcal{F} \psi_{\mu} \\
&\stackrel{\psi_{\mu} \neq 0}{\Leftrightarrow} f^4 + 2\mathcal{F} f^2 + \mathcal{G}^2 = 0,
\end{aligned}$$

## 2. State of the art

which has the solution

$$f^2 = \frac{-2\mathcal{F} \pm \sqrt{4\mathcal{F}^2 - 4\mathcal{G}^2}}{2} = a^2 / -b^2 \quad (2.132)$$

and thus

$$\text{Eig}(\mathbf{F}) = \{\pm a, \pm ib\}. \quad (2.133)$$

Using these eigenvalues (2.112) can be evaluated, yielding

$$\begin{aligned} l(s) &= \frac{1}{2} \text{tr} \ln[(e\mathbf{F}s)^{-1} \sin(e\mathbf{F}s)] \\ &= \frac{1}{2} \sum_{x \in \text{Eig}(\mathbf{F})} \ln[(exs)^{-1} \sin(exs)] \\ &= \frac{1}{2} \sum_{x \in \text{Eig}(\mathbf{F})} \ln[\text{sinc}(exs)] \\ &= \ln[\text{sinc}(eas)] + \ln[\text{sinc}(iebs)]. \end{aligned} \quad (2.134)$$

Inserting this into the exponential results in

$$e^{-l(s)} = \frac{1}{\text{sinc}(eas)\text{sinc}(iebs)} = \frac{ie^2s^2ab}{\sin(eas)\sin(iebs)} = \frac{e^2s^2ab}{\sin(eas)\sinh(ebs)}. \quad (2.135)$$

Combining the results of the trace operations (2.135) and (2.126) with the Lagrangian in (2.111) gives the expression

$$\begin{aligned} \mathcal{L}^{(1)} &= \frac{-1}{32\pi^2} \int_0^\infty ds \frac{e^{-m^2s}}{s^3} \frac{e^2s^2ab}{\sin(eas)\sinh(ebs)} 4 \cosh(ebs) \cos(eas) \\ &= \frac{-1}{8\pi^2} \int_0^\infty ds \frac{e^{-m^2s}}{s^3} e^2s^2ab \coth(ebs) \cot(eas). \end{aligned} \quad (2.136)$$

Since  $\mathcal{L}^{(1)}$  is computed using a variation calculus, it is determined up to a constant. This constant is chosen, such that  $\mathcal{L}^{(1)}$  vanishes in the absence of fields, i.e.,  $a = b = 0$ .  $\mathcal{L}^{(1)}$  takes the form

$$\mathcal{L}^{(1)} = \frac{-1}{8\pi^2} \int_0^\infty ds s^{-3} e^{-m^2s} (e^2s^2ab \coth(ebs) \cot(eas) - 1). \quad (2.137)$$

Performing a Taylor series with respect to  $s$  around zero shows that the lowest order term

$$-\frac{1}{8\pi^2} \int_0^\infty ds s^{-3} e^{-m^2s} \frac{a^2 - b^2}{3} e^2s^2 = \frac{e^2}{12\pi^2} \int_0^\infty ds s^{-1} e^{-m^2s} \mathcal{F} \quad (2.138)$$

diverges around 0. This singularity can be mended by re-normalizing the charge. To do so the full Lagrangian is considered

$$\begin{aligned}\mathcal{L} &= \mathcal{L}^{(0)} + \mathcal{L}^{(1)} \\ &= -\mathcal{F} + \frac{e^2}{12\pi^2} \int_0^\infty ds s^{-1} e^{-m^2 s} \mathcal{F} \\ &\quad - \frac{1}{8\pi^2} \int_0^\infty ds s^{-3} e^{-m^2 s} \left( e^2 s^2 ab \coth(esb) \cot(esa) - 1 + \frac{2}{3} e^2 s^2 \mathcal{F} \right)\end{aligned}\tag{2.139}$$

and rescaled making use of

$$\begin{aligned}a_{Renorm} &= a\sqrt{1 + Ce^2}, \\ b_{Renorm} &= b\sqrt{1 + Ce^2}, \\ e_{Renorm}^2 &= \frac{e^2}{1 + Ce^2}, \\ C &= -\frac{1}{12\pi^2} \int_0^\infty ds s^{-1} e^{-m^2 s},\end{aligned}\tag{2.140}$$

which, dropping the *Renorm* subscript, results in

$$\begin{aligned}\mathcal{L} &= -\mathcal{F} \\ &\quad - \frac{1}{8\pi^2} \int_0^\infty ds s^{-3} e^{-m^2 s} \left( e^2 s^2 ab \coth(esb) \cot(esa) - 1 + \frac{2}{3} e^2 s^2 \mathcal{F} \right).\end{aligned}\tag{2.141}$$

Finally, in order to make the integration variable dimensionless the new variable  $\tilde{s} = m^2 s$  is introduced, resulting in

$$\begin{aligned}\mathcal{L}^{(1)} &= -\frac{m^4}{8\pi^2} \int_0^\infty d\tilde{s} \tilde{s}^{-3} e^{-\tilde{s}} \left[ \frac{e^2 \tilde{s}^2}{m^4} ab \coth\left(\frac{e\tilde{s}b}{m^2}\right) \cot\left(\frac{e\tilde{s}a}{m^2}\right) \right. \\ &\quad \left. - 1 + \frac{2}{3} \frac{e^2}{m^2} \tilde{s}^2 \mathcal{F} \right],\end{aligned}\tag{2.142}$$

which upon dropping the tilde and using the relation  $E_{cr} = m^2/e$  becomes the well know Heisenberg-Euler Lagrangian

$$\mathcal{L}_{HE} = -\frac{m^4}{8\pi^2} \int_0^\infty ds s^{-3} e^{-s} \left[ \frac{s^2 ab}{E_{cr}^2} \coth\left(\frac{sb}{E_{cr}}\right) \cot\left(\frac{sa}{E_{cr}}\right) - 1 + \frac{2}{3} \frac{s^2 \mathcal{F}}{E_{cr}^2} \right].\tag{2.143}$$

### 2.2.3. Beyond the constant field approximation

For the study of all possible effects the Lagrangian would have to be rederived for non-constant quantum fields. It has, however, been shown both analytically

## 2. State of the art

[17] and numerically [18] that effects of variations in non-constant background quantum-fields are negligible when the variations of the field strengths are on a much larger scale than the Compton wavelength  $\lambda_C = \frac{h}{mc} = 2.426 \times 10^{-12}\text{m}$  [19]. Thus, for the simulation of all relevant nonlinear optical effects with the exception of those involving frequencies in the  $\gamma$  energy range, the Lagrangian as given in (2.143) can be used.

## 2.3. Non-pertubative pair production

The question addressed now, is to which extent particle production and the propagation of charged particles are relevant for the physics in strong em-backgrounds. This question can be answered by computing the pair production rate in the quantum vacuum. Starting from the vacuum persistence amplitude [20]

$$\langle 0|0\rangle = e^{iW^{(1)}}, \quad (2.144)$$

which states, that the ingoing and outgoing states are both vacuum states. This can be reformulated as

$$\langle 0|0\rangle = e^{i\mathcal{L}^{(1)}VT}, \quad (2.145)$$

where  $VT$  is the space-time volume as the fields are assumed to be constant. Thus, the probability for the vacuum to remain particle free is given by

$$|\langle 0|0\rangle|^2 = e^{-2\Im[\mathcal{L}^{(1)}VT]}. \quad (2.146)$$

Here  $\Im$  is used to refer to the imaginary part. The probability, that the vacuum is broken due to pair creation is therefore given by

$$P_{e^+e^-} = 1 - |\langle 0|0\rangle|^2 = 1 - e^{-2\Im[\mathcal{L}^{(1)}VT]}. \quad (2.147)$$

For the pair creation rate it is obtained

$$R_{e^+e^-} = \frac{P_{e^+e^-}}{VT} = \frac{1 - e^{-2\Im[\mathcal{L}^{(1)}VT]}}{VT}. \quad (2.148)$$

In this context the term *pair creation* is used to refer to the creation of an arbitrary number of pairs. In order to better visualize this quantity the case of a purely electric field, where  $|\vec{E}| \ll E_{cr}$  is considered. This implies that  $\Im[\mathcal{L}^{(1)}VT] \ll 1$  and therefore the exponential can be replaced with the first two terms of its Taylor series around  $|\vec{E}| = 0$

$$R_{e^+e^-} = \frac{1 - 1 - 2\Im[\mathcal{L}^{(1)}VT]}{VT} = -2\Im[\mathcal{L}^{(1)}]$$

$$= \Im \left[ \frac{m^4}{4\pi^2} \int_0^\infty ds s^{-3} e^{-s} \left( \frac{s^2 ab}{E_{cr}^2} \coth \left( \frac{sb}{E_{cr}} \right) \cot \left( \frac{sa}{E_{cr}} \right) - 1 + \frac{2}{3} \frac{s^2 \mathcal{F}}{E_{cr}^2} \right) \right]. \quad (2.149)$$

Since the em-field is assumed to be purely electric it follows

$$\mathcal{F} = \frac{\vec{E}^2}{2}, \quad \mathcal{G} = 0, \quad a = |\vec{E}| = E, \quad b = 0. \quad (2.150)$$

With the help of (2.150) equation (2.148) simplifies to

$$R_{e^+e^-} = \frac{m^4}{4\pi^2} \Im \left[ \int_0^\infty ds s^{-3} e^{-s} \left( \frac{sE}{E_{cr}} \cot \left( \frac{sE}{E_{cr}} \right) - 1 + \frac{1}{3} \frac{s^2 E^2}{E_{cr}^2} \right) \right]. \quad (2.151)$$

It can now be seen that the integrand in (2.151) has poles at  $s = n\pi E_{cr}/E$ . By using the residuum theorem it is thus obtained that

$$\begin{aligned} \int_0^\infty ds s^{-3} e^{-s} \left( \frac{sE}{E_{cr}} \cot \left( \frac{sE}{E_{cr}} \right) - 1 + \frac{1}{3} \frac{sE^2}{E_{cr}^2} \right) \\ = \pi i \sum_{n=1}^{\infty} \text{Res} \left( s = \frac{n\pi E_{cr}}{E} \right), \end{aligned} \quad (2.152)$$

With the help of

$$\text{Res}_a \left( \frac{g}{f} \right) = \frac{g(a)}{f'(a)}, \quad (2.153)$$

the residuum in the right hand side of (2.152) can be computed

$$\text{Res} \left( s = \frac{n\pi E_{cr}}{E} \right) = \frac{E^2}{n^2 \pi^2 E_{cr}^2} e^{-n\pi E_{cr}/E}. \quad (2.154)$$

Inserting (2.154) into (2.152), the pair production rate becomes

$$R_{e^+e^-} = \frac{m^4 E^2}{4\pi^3 E_{cr}^2} \sum_{n=1}^{\infty} \frac{1}{n^2} e^{-n\pi E_{cr}/E} = \frac{E^2 \alpha}{\pi^2} \sum_{n=1}^{\infty} \frac{1}{n^2} e^{-n\pi E_{cr}/E}. \quad (2.155)$$

Equation (2.155) shows that the electron pair production is exponentially suppressed for  $E < E_{cr}$ . This implies, that for  $E < E_{cr}$  pair creation can be safely neglected without altering the physical response of the system.

## 2.4. The weak field expansion

It is useful to normalize the electromagnetic invariants  $\mathcal{F}, \mathcal{G}$  and the secular invariants  $a, b$  to the critical field strength as:

$$\mathcal{F} = -\frac{F^{\mu\nu} F_{\mu\nu}}{4E_{cr}^2}, \quad \mathcal{G} = -\frac{F^{\mu\nu} F_{\mu\nu}^*}{4E_{cr}^2}, \quad (2.156)$$

## 2. State of the art

$$a = \sqrt{\sqrt{\mathcal{F}^2 + \mathcal{G}^2} + \mathcal{F}}, \quad b = \sqrt{\sqrt{\mathcal{F}^2 + \mathcal{G}^2} - \mathcal{F}}, \quad (2.157)$$

where  $F$  is the electromagnetic tensor and  $F^*$  its dual. Using these definitions the effective Lagrangian takes the form

$$\mathcal{L}_{\text{HE}} = -\frac{m^4}{8\pi^2} \int_0^\infty ds \frac{e^{-s}}{s^3} \left( \frac{s^2}{3} (a^2 - b^2) - 1 + abs^2 \cot(as) \coth(bs) \right). \quad (2.158)$$

### Taylor series

The functions  $\coth$  and  $\cot$  can now be Taylor expanded around  $as = bs = 0$  yielding

$$bs \coth(bs) = 1 + \frac{(bs)^2}{3} - \frac{(bs)^4}{45} + \frac{2(bs)^6}{945} - \frac{(bs)^8}{4725} + O[(bs)^9], \quad (2.159)$$

$$as \cot(as) = 1 - \frac{(as)^2}{3} - \frac{(as)^4}{45} - \frac{2(as)^6}{945} - \frac{(as)^8}{4725} + O[(as)^9]. \quad (2.160)$$

Putting (2.159) and (2.160) into the integrand  $I$  in (2.158) results in

$$I = e^{-s} \left[ s \left( -\frac{a^4}{45} - \frac{a^2 b^2}{9} - \frac{b^4}{45} \right) + s^3 \left( -\frac{2a^6}{945} - \frac{a^4 b^2}{135} + \frac{a^2 b^4}{135} + \frac{2b^6}{945} \right) + s^5 \left( -\frac{a^8}{4725} - \frac{2a^6 b^2}{2835} + \frac{a^4 b^4}{2025} - \frac{2a^2 b^6}{2835} - \frac{b^8}{4725} \right) + \dots \right]. \quad (2.161)$$

Performing the integration in (2.158) making use of (2.161) results in

$$\mathcal{L}_{HE} \approx \frac{m^4}{360\pi^2} (4\mathcal{F}^2 + 7\mathcal{G}^2) \quad (2.162a)$$

$$+ \frac{m^4}{630\pi^2} (8\mathcal{F}^3 + 13\mathcal{F}\mathcal{G}^2) \quad (2.162b)$$

$$+ \frac{m^4}{945\pi^2} (48\mathcal{F}^4 + 88\mathcal{F}^2\mathcal{G}^2 + 19\mathcal{G}^4) \quad (2.162c)$$

$$+ \frac{4m^4}{1485\pi^2} (160\mathcal{F}^5 + 332\mathcal{F}^3\mathcal{G}^2 + 127\mathcal{F}\mathcal{G}^4). \quad (2.162d)$$

Note, that the terms (2.162a), (2.162b), (2.162c), ... correspond to the seeded processes with 4, 6, 8, ... photons as depicted in figure 2.1. This result is to be expected as by Furry's theorem [21] as interactions with odd number of external photons have to vanish due to the invariance of the vacuum under charge conjugation.

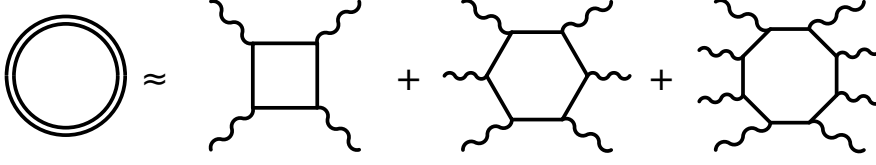


**Figure 2.1.:** Depiction of the weak field Feynman diagram loop expansion for the Heisenberg-Euler Lagrangian. To the left the full seeded loop and on the right the 4, 6 and 8 photon box diagrams are shown. Note that these correspond to (2.162a), (2.162b) and (2.162c) respectively.

## 2.5. The nonlinear Maxwell equations

### Field tensor definitions

The electromagnetic field tensors  $F^{\mu\nu}$  and  $F^{*\mu\nu}$  are given by

$$F^{\mu\nu} = \begin{pmatrix} 0 & -E_x/c & -E_y/c & -E_z/c \\ E_x/c & 0 & -B_z & B_y \\ E_y/c & B_z & 0 & -B_x \\ E_z/c & -B_y & B_x & 0 \end{pmatrix}, \quad (2.163)$$

$$F^{*\mu\nu} = \begin{pmatrix} 0 & -B_x & -B_y & -B_z \\ B_x & 0 & E_z/c & -E_y/c \\ B_y & -E_z/c & 0 & E_x/c \\ B_z & E_y/c & -E_x/c & 0 \end{pmatrix}, \quad (2.164)$$

when using the metric

$$\eta_{ab} = \begin{pmatrix} 1 & 0 & 0 & 0 \\ 0 & -1 & 0 & 0 \\ 0 & 0 & -1 & 0 \\ 0 & 0 & 0 & -1 \end{pmatrix} \quad F_{\mu\nu} = \eta_{\mu\alpha} F^{\alpha\beta} \eta_{\beta\nu}. \quad (2.165)$$

The field strength tensor in (2.163) can be represented in terms of the electromagnetic 4-potential  $A$  as

$$F^{\mu\nu} = \partial^\mu A^\nu - \partial^\nu A^\mu, \quad F_{\mu\nu} = \partial_\mu A_\nu - \partial_\nu A_\mu. \quad (2.166)$$

With the help of the Levi-Civita tensor  $\epsilon$  the dual tensor  $F^{*\mu\nu}$  given in (2.164) can be written as

$$F^{*\mu\nu} = \frac{1}{2} \epsilon^{\mu\nu\sigma\gamma} F_{\sigma\gamma}. \quad (2.167)$$

## 2. State of the art

### Electromagnetic invariants

Recalling the first electromagnetic Lorentz  $\mathcal{F}$  invariant given by

$$\mathcal{F} = -\frac{1}{4}F^{\mu\nu}F_{\mu\nu} = \frac{1}{2}\left(\frac{\vec{E}^2}{c^2} - \vec{B}^2\right), \quad (2.168)$$

the derivatives can be computed to be

$$\frac{\partial\mathcal{F}}{\partial\vec{E}} = \frac{1}{c^2}\vec{E}, \quad \frac{\partial\mathcal{F}}{\partial\vec{B}} = -\vec{B} \quad (2.169)$$

and

$$\begin{aligned} \frac{\partial\mathcal{F}}{\partial(\partial_{\bar{\mu}}A_{\bar{\nu}})} &= -\frac{1}{4}\frac{\partial}{\partial(\partial_{\bar{\mu}}A_{\bar{\nu}})}(\partial^{\mu}A^{\nu} - \partial^{\nu}A^{\mu})(\partial_{\mu}A_{\nu} - \partial_{\nu}A_{\mu}) \\ &= -\frac{1}{4}\frac{\partial}{\partial(\partial_{\bar{\mu}}A_{\bar{\nu}})}(\partial^{\mu}A^{\nu}\partial_{\mu}A_{\nu} - \partial^{\mu}A^{\nu}\partial_{\nu}A_{\mu} - \partial^{\nu}A^{\mu}\partial_{\mu}A_{\nu} + \partial^{\nu}A^{\mu}\partial_{\nu}A_{\mu}) \\ &= -\frac{1}{4}\frac{\partial}{\partial(\partial_{\bar{\mu}}A_{\bar{\nu}})}2(\partial^{\mu}A^{\nu}\partial_{\mu}A_{\nu} - \partial^{\mu}A^{\nu}\partial_{\nu}A_{\mu}) \\ &= -\frac{1}{2}(2\partial^{\mu}A^{\nu}\delta_{\mu\bar{\mu}}\delta_{\nu\bar{\nu}} - 2\partial^{\mu}A^{\nu}\delta_{\mu\bar{\nu}}\delta_{\nu\bar{\mu}}) \\ &= -(\partial^{\bar{\mu}}A^{\bar{\nu}} - \partial^{\bar{\nu}}A^{\bar{\mu}}) = -F^{\bar{\mu}\bar{\nu}}. \end{aligned} \quad (2.170)$$

Also, recalling that the second electromagnetic Lorentz invariant  $\mathcal{G}$  can be computed using the dual field strength tensor

$$\mathcal{G} = -\frac{1}{4}F^{\mu\nu}F_{\mu\nu}^* = \frac{1}{c}\vec{E} \cdot \vec{B} \quad (2.171)$$

its derivatives can be computed yielding

$$\frac{\partial\mathcal{G}}{\partial\vec{E}} = \frac{1}{c}\vec{B}, \quad \frac{\partial\mathcal{G}}{\partial\vec{B}} = \frac{1}{c}\vec{E} \quad (2.172)$$

and

$$\begin{aligned} \frac{\partial\mathcal{G}}{\partial(\partial_{\bar{\mu}}A_{\bar{\nu}})} &= -\frac{1}{4}\frac{\partial}{\partial(\partial_{\bar{\mu}}A_{\bar{\nu}})}(\partial^{\mu}A^{\nu} - \partial^{\nu}A^{\mu})\epsilon_{\mu\nu}^{\alpha\beta}(\partial_{\alpha}A_{\beta} - \partial_{\beta}A_{\alpha}) \\ &= -\frac{\epsilon_{\mu\nu}^{\alpha\beta}}{4}\frac{\partial}{\partial(\partial_{\bar{\mu}}A_{\bar{\nu}})}(\partial^{\mu}A^{\nu}\partial_{\alpha}A_{\beta} - \partial^{\mu}A^{\nu}\partial_{\beta}A_{\alpha} - \partial^{\nu}A^{\mu}\partial_{\alpha}A_{\beta} + \partial^{\nu}A^{\mu}\partial_{\beta}A_{\alpha}) \\ &= -\frac{\epsilon_{\mu\nu}^{\alpha\beta}}{4}\frac{\partial}{\partial(\partial_{\bar{\mu}}A_{\bar{\nu}})}2(\partial^{\mu}A^{\nu}\partial_{\alpha}A_{\beta} - \partial^{\nu}A^{\mu}\partial_{\alpha}A_{\beta}) \\ &= -\frac{\epsilon^{\mu\nu\alpha\beta}}{2}\frac{\partial}{\partial(\partial_{\bar{\mu}}A_{\bar{\nu}})}(\partial_{\mu}A_{\nu}\partial_{\alpha}A_{\beta} - \partial_{\nu}A_{\mu}\partial_{\alpha}A_{\beta}) \end{aligned}$$

$$\begin{aligned}
 &= -\frac{\epsilon^{\mu\nu\alpha\beta}}{2} (\delta_{\mu\tilde{\mu}}\delta_{\nu\tilde{\nu}}\partial_\alpha A_\beta + \delta_{\alpha\tilde{\mu}}\delta_{\beta\tilde{\nu}}\partial_\mu A_\nu - \delta_{\nu\tilde{\mu}}\delta_{\mu\tilde{\nu}}\partial_\alpha A_\beta - \delta_{\alpha\tilde{\mu}}\delta_{\beta\tilde{\nu}}\partial_\nu A_\mu) \\
 &= -\epsilon^{\mu\nu\alpha\beta} (\delta_{\alpha\tilde{\mu}}\delta_{\beta\tilde{\nu}}\partial_\mu A_\nu - \delta_{\alpha\tilde{\mu}}\delta_{\beta\tilde{\nu}}\partial_\nu A_\mu) \\
 &= -\epsilon^{\mu\nu\tilde{\mu}\tilde{\nu}} (\partial_\mu A_\nu - \partial_\nu A_\mu) = -F^{*\tilde{\mu}\tilde{\nu}}.
 \end{aligned} \tag{2.173}$$

### 2.5.1. Euler-Lagrange formalism

The *Euler-Lagrange* formalism as derived from the least action principle is given by

$$\partial_\mu \left( \frac{\partial \mathcal{L}}{\partial (\partial_\mu A_\nu)} \right) - \frac{\partial \mathcal{L}}{\partial A_\nu} = 0. \tag{2.174}$$

Since in the quantum vacuum the Lagrange function is the sum of the Maxwell and Heisenberg-Euler Lagrangian it holds

$$\mathcal{L} = \mathcal{L}_{\text{MW}} + \mathcal{L}_{\text{HE}} = \mathcal{F} + \mathcal{L}_{\text{HE}}. \tag{2.175}$$

Since  $\mathcal{L}_{\text{MW}}$  and  $\mathcal{L}_{\text{HE}}$  solely depend on the electromagnetic field strengths the second term in (2.174) vanishes leaving

$$\partial_\mu \left( \frac{\partial \mathcal{L}_{\text{MW}}}{\partial (\partial_\mu A_\nu)} \right) + \partial_\mu \left( \frac{\partial \mathcal{L}_{\text{HE}}}{\partial (\partial_\mu A_\nu)} \right) = 0, \tag{2.176}$$

which in turn can be rewritten as

$$\begin{aligned}
 &-\partial_\mu \left( \frac{\partial \mathcal{L}_{\text{MW}}}{\partial (\partial_\mu A_\nu)} \right) = \partial_\mu \left( \frac{\partial \mathcal{L}_{\text{HE}}}{\partial (\partial_\mu A_\nu)} \right) \\
 \Leftrightarrow &-\partial_\mu \left( \frac{\partial \mathcal{F}}{\partial (\partial_\mu A_\nu)} \right) = \partial_\mu \left( \frac{\partial \mathcal{L}_{\text{HE}}}{\partial \mathcal{F}} \frac{\partial \mathcal{F}}{\partial (\partial_\mu A_\nu)} + \frac{\partial \mathcal{L}_{\text{HE}}}{\partial \mathcal{G}} \frac{\partial \mathcal{G}}{\partial (\partial_\mu A_\nu)} \right) \\
 \Leftrightarrow &-\partial_\mu F^{\mu\nu} = \partial_\mu (\partial_{\mathcal{F}} \mathcal{L}_{\text{HE}} F^{\mu\nu} + \partial_{\mathcal{G}} \mathcal{L}_{\text{HE}} F^{*\mu\nu}) \\
 \Leftrightarrow &-\partial_t F^{0\nu} - \partial_i F^{i\nu} = \partial_t (\partial_{\mathcal{F}} \mathcal{L}_{\text{HE}} F^{0\nu} + \partial_{\mathcal{G}} \mathcal{L}_{\text{HE}} F^{*0\nu}) \\
 &\quad + \partial_i (\partial_{\mathcal{F}} \mathcal{L}_{\text{HE}} F^{i\nu} + \partial_{\mathcal{G}} \mathcal{L}_{\text{HE}} F^{*i\nu}),
 \end{aligned} \tag{2.177}$$

which is a system of 4 independent partial differential equations. Using the definition of the field strength tensor (2.163) and its dual (2.164), (2.177) may be reformulated for the case that  $\nu \neq 0$  as

$$\begin{aligned}
 &-\partial_t F^{0j} - \partial_i F^{ij} = \partial_t (\partial_{\mathcal{F}} \mathcal{L}_{\text{HE}} F^{0j} + \partial_{\mathcal{G}} \mathcal{L}_{\text{HE}} F^{*0j}) + \partial_i (\partial_{\mathcal{F}} \mathcal{L}_{\text{HE}} F^{ij} + \partial_{\mathcal{G}} \mathcal{L}_{\text{HE}} F^{*ij}) \\
 \Leftrightarrow &-\frac{1}{c} \partial_t E_j + \partial_i \epsilon^{ijk} B_k = \partial_t \left( \frac{1}{c} \partial_{\mathcal{F}} \mathcal{L}_{\text{HE}} E_j + \partial_{\mathcal{G}} \mathcal{L}_{\text{HE}} B_j \right) \\
 &\quad + \partial_i \left( -\partial_{\mathcal{F}} \mathcal{L}_{\text{HE}} \epsilon^{ijk} B_k + \frac{1}{c} \partial_{\mathcal{G}} \mathcal{L}_{\text{HE}} \epsilon^{ijk} E_k \right)
 \end{aligned}$$

## 2. State of the art

$$\begin{aligned}
\Leftrightarrow -\frac{1}{c}\partial_t\vec{E} + \nabla \times \vec{B} &= \partial_t \left( \frac{1}{c}\partial_{\mathcal{F}}\mathcal{L}_{\text{HE}}\vec{E} + \partial_{\mathcal{G}}\mathcal{L}_{\text{HE}}\vec{B} \right) \\
&\quad + \left( -\partial_{\mathcal{F}}\mathcal{L}_{\text{HE}}\nabla \times \vec{B} + \frac{1}{c}\partial_{\mathcal{G}}\mathcal{L}_{\text{HE}}\nabla \times \vec{E} \right) \\
\Leftrightarrow -\frac{1}{c}\partial_t\vec{E} + \nabla \times \vec{B} &= \partial_t (c\partial_{\mathcal{F}}\mathcal{L}_{\text{HE}}\partial_{\vec{E}}\mathcal{F} + c\partial_{\mathcal{G}}\mathcal{L}_{\text{HE}}\partial_{\vec{B}}\mathcal{G}) \\
&\quad - \nabla \times (-\partial_{\mathcal{F}}\mathcal{L}_{\text{HE}}\partial_{\vec{B}}\mathcal{F} - \partial_{\mathcal{G}}\mathcal{L}_{\text{HE}}\partial_{\vec{E}}\mathcal{G}) \\
\Leftrightarrow -\frac{1}{c}\partial_t\vec{E} + \nabla \times \vec{B} &= c\partial_t\partial_{\vec{E}}\mathcal{L}_{\text{HE}} + \nabla \times \partial_{\vec{B}}\mathcal{L}_{\text{HE}}. \tag{2.178}
\end{aligned}$$

Reordering of the terms in (2.178) yields

$$\frac{1}{c}\partial_t \left( \vec{E} + c^2\partial_{\vec{E}}\mathcal{L}_{\text{HE}} \right) = \nabla \times \left( \vec{B} - \partial_{\vec{B}}\mathcal{L}_{\text{HE}} \right). \tag{2.179}$$

### 2.5.2. Comparison with the classical Maxwell equations

The macroscopic formulation of Ampère law in Maxwells formulation is

$$\frac{1}{c}\partial_t \left( \vec{E} + \vec{P} \right) = \nabla \times \left( \vec{B} - \vec{M} \right). \tag{2.180}$$

Comparing this to (2.179) results in

$$\vec{P} = c^2\frac{\partial\mathcal{L}_{\text{HE}}}{\partial\vec{E}}, \quad \vec{M} = \frac{\partial\mathcal{L}_{\text{HE}}}{\partial\vec{B}}. \tag{2.181}$$

If the normalization of the em-fields to the critical field strength is done as described section 2.4 the electric and magnetic fields in (2.180) get a factor  $m^4/4\pi\alpha$ . In order to leave the  $\vec{E}$  and  $\vec{B}$  fields in (2.180) prefactor free the whole equation has to be multiplied by  $4\pi\alpha/m^4$  leaving

$$\vec{P} = \frac{4\pi\alpha}{m^4}\frac{\partial\mathcal{L}_{\text{HE}}}{\partial\vec{E}}, \quad \vec{M} = \frac{4\pi\alpha}{m^4}\frac{\partial\mathcal{L}_{\text{HE}}}{\partial\vec{B}}, \tag{2.182}$$

where the  $c$  factor is negelected as it is set to 1.

## 2.6. The probe in a constant field case

In [13, 22] the vacuum birefringence is derived from the inhomogeneous wave equation caused by a background field. In the case of a probe that co-axially counter-propagates through a linear polarized em-background, the change of the refractive index is given by

$$n_{\pm} = 1 + \frac{\alpha}{45\pi}(11 \pm 3)\frac{E^2}{E_{cr}^2}, \tag{2.183}$$

## 2.6. The probe in a constant field case

where  $n_+$  is the refractive index for a probe whose polarization is parallel to the polarization of the strong background.  $n_-$  is the refractive index for a probe whose polarization vector is orthogonal to the polarization vector of the strong background. Note, that once again the  $E_{cr}$  term can be absorbed into the electric field strength through normalization.

The refractive indices (2.183) affect the propagation of a light probe in multiple ways. In one dimension they cause waves to have different phase and group velocities in dependence of their polarization,

$$v_g = v_{ph} = \frac{1}{n}, \quad (2.184)$$

which leads to the well-known vacuum birefringence [23, 24, 25, 26]. The latter leads will lead among other effects to polarization flipping and light by light focusing.

### Polarization flipping

As the components of an initially linearly polarized probe pulse propagate at different speeds its polarization vector is rotated.

For illustration the case of a plane wave probe with  $\vec{k} = (k_x, 0, 0)$  propagating through a strong electric field is considered. The fields are given by

$$\vec{E}_p(x) = \vec{e}_y \cos(k_x x) + \vec{e}_z \cos(k_x x), \quad \vec{B}_p = -\hat{k} \times \vec{E}_p, \quad \vec{E}_b = A\vec{e}_z. \quad (2.185)$$

It holds that

$$E_{\parallel}(x) = \vec{E}_p(x) \cdot (\vec{e}_y + \vec{e}_z) = 2 \cos(k_x x), \quad E_{\perp}(x) = \vec{E}_p(x) \cdot (\vec{e}_y - \vec{e}_z) = 0, \quad (2.186)$$

implying that the probe is linearly polarized at an angle of  $45^\circ$  with respect to the polarization of the background. At time  $t$  the probe wave has the form

$$\vec{E}_p(x, t) = \vec{e}_y \cos\left(k_x x + \frac{k_x t}{n_-}\right) + \vec{e}_z \cos\left(k_x x + \frac{k_x t}{n_+}\right), \quad \vec{B}_p = -\hat{k} \times \vec{E}_p, \quad (2.187)$$

where the different refractive indices (2.183) cause a phase shift of

$$2\Delta_{\Phi} = k_x |v_{ph,+} - v_{ph,-}| t \stackrel{\text{weak f.}}{\approx} \frac{2\alpha}{15} \frac{1}{\lambda} \frac{A^2}{E_{cr}^2} t \quad (2.188)$$

between  $E_{\parallel}$  and  $E_{\perp}$ . The factor 2 in (2.188) is introduced for convenience. Using trigonometric relations it is obtained

$$\vec{E}_p(x, t) = \vec{e}_y \cos(x_0 - \Delta_{\Phi}) + \vec{e}_z \cos(x_0 + \Delta_{\Phi})$$

## 2. State of the art

$$\begin{aligned}
&= \vec{e}_y (\cos(x_0) \cos(\Delta_\Phi) - \sin(x_0) \sin(\Delta_\Phi)) \\
&\quad + \vec{e}_z (\cos(x_0) \cos(\Delta_\Phi) + \sin(x_0) \sin(\Delta_\Phi)) \\
&= (\vec{e}_y + \vec{e}_z) \cos(x_0) \cos(\Delta_\Phi) - (\vec{e}_y - \vec{e}_z) \sin(x_0) \sin(\Delta_\Phi), \tag{2.189}
\end{aligned}$$

where  $x_0 = x + t$ . Computing the projections anew yields

$$E_{\parallel}(x, t) = 2 \cos(x_0) \cos(\Delta_\Phi), \quad E_{\perp}(x, t) = -2 \sin(x_0) \sin(\Delta_\Phi). \tag{2.190}$$

Equation (2.190) clearly shows how the birefringence is transporting energy from one polarization direction to the other. Since the classical field amplitude  $E_{\perp}$  can be translated into quantum dynamical probabilities by considering the probability to find a flipped photon in an originally linear polarized pulse. This quantity is equal to the ratio of orthogonal polarized photons to the total number of photons and thus

$$\begin{aligned}
P_{\text{flip}} &= \frac{N_{\perp}}{N} = \frac{N_{\perp} \hbar f}{n \hbar f} = \frac{\int dx E_{\perp}(x)^2}{\int dx (E_{\parallel}(x)^2 + E_{\perp}(x)^2)} \\
&= \frac{\sin(\Delta_\Phi)^2 \int dx_0 \sin(x_0)^2}{\cos(\Delta_\Phi)^2 \int dx_0 \cos(x_0)^2 + \sin(\Delta_\Phi)^2 \int dx_0 \sin(x_0)^2} \\
&= \frac{\sin(\Delta_\Phi)^2}{\cos(\Delta_\Phi)^2 + \sin(\Delta_\Phi)^2} = \sin(\Delta_\Phi)^2 \stackrel{\text{weak f.}}{\approx} \frac{\alpha^2 t^2}{225 \lambda^2} \left( \frac{A}{E_{cr}} \right)^4. \tag{2.191}
\end{aligned}$$

Expression (2.191) can be generalized for arbitrary angles  $\sigma$  between background and probe polarizations, as well as for arbitrary backgrounds (see [13]),

$$P_{\text{flip}} = \frac{\alpha^2}{225 \lambda^2} \sin^2(2\sigma) \left( \int_{-\infty}^{\infty} dx_0 \frac{A(x_0)^2}{E_{cr}^2} \right)^2. \tag{2.192}$$

## 2.7. The case of two colliding plane wave pulses

Measuring the birefringence (2.192) for constant fields has been tried on scaled down experiments [27], which have yielded upper bounds for  $P_{\text{flip}}$ . However, the regime for which polarization flipping becomes directly measurable is hard to reach. It has been suggested that appropriate strengths for polarization flipping can be encountered in the vicinity of magnetic cosmological bodies [28].

A way to achieve high intensities in the lab is through tightly focused laser beams. As (2.192) shows the resulting polarization flip of the probe pulse does not depend on the form of the background field but on the squared field intensity integrated along the probe propagation direction. Due (2.192) it is more efficient for polarization flipping to have high intensities than long optical paths. The resulting setup

## 2.7. The case of two colliding plane wave pulses

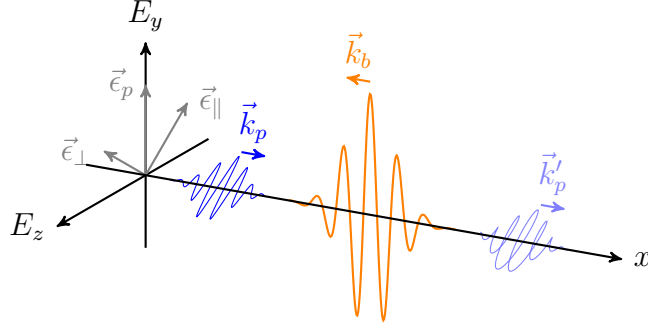


**Figure 2.2.:** Qualitative sketch of the electric fields in a coaxial background-probe experiment for measuring vacuum birefringence. The probe (blue) travels through the counter-propagating background (orange) experiencing a polarisation flip due to the different refractive indices for different polarization directions (2.184).

for two co-axially counter-propagating plane wave pulses with  $\hat{k}_p = -\hat{k}_b$  can be seen in figure 2.2.

As subsection 2.7.3 shows, it is possible to iteratively solve such a problem using approximations such as neglecting the pulse envelope function. To gain insight into the physics of the interaction of two pulses the diagrammatic representation of the weak-field expansion is used (see figure 2.1) in combination with energy and momentum conservation.

### 2.7.1. Contributions from 4-photon interaction

Starting with the 4-photon diagram, the first thing to note is that a linearly polarized propagating pulse cannot interact with itself. This is a triviality in the quantum picture and is also expressed in the effective action representation by the fact that both  $\mathcal{F}$  and  $\mathcal{G}$  will become zero. Thus, it can be concluded that the scattering processes have to include at least one photon from the background and one photon from the probe.

As the 4-photon diagram has for legs two degrees of freedom are left. Due to charge parity, the processes at the vertices have to be creation or annihilation and not scattering of the electrons and positrons. As a consequence, the energy of all the participating photon is given by

$$\varepsilon_{\gamma_j} = n\hbar\omega_p + m\hbar\omega_b, \quad (2.193)$$

where  $\varepsilon_{\gamma_j}$  with  $j \in \{1, 2, 3, 4\}$  are the energies of the four photons and  $n, m$  are integer numbers. Due to energy conservation the total sum of the energies of

## 2. State of the art

incoming minus outgoing photons has to be zero

$$\sum_{j=1}^4 \varepsilon_{\gamma_j} = 0 \quad (2.194)$$

An example for a diagram fulfilling (2.193) and (2.194) can be seen in figure 2.3.

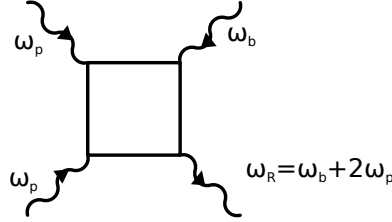


**Figure 2.3.:** High harmonic generation by 4-photon interaction. It consist of two incoming photons from the probe  $p$ , one incoming photon from the strong background  $b$  and an exiting photon whose frequency has to be  $\omega_b + 2\omega_p$  due to energy conservation.

Furthermore the 4-vector momenta of the photons for probe and background pulses have the form

$$\mathbf{k}_p = \omega_p \begin{pmatrix} 1 \\ \hat{k}_p \end{pmatrix}, \quad \mathbf{k}_b = \omega_b \begin{pmatrix} 1 \\ -\hat{k}_p \end{pmatrix}. \quad (2.195)$$

They satisfy the on shell condition

$$(k_{p,\mu})^2 = (k_{b,\mu})^2 = k_{b,\mu} k_{b,\nu} \eta^{\mu\nu} = \omega_b^2 (1 - \hat{k}_p \cdot \hat{k}_p) = 0. \quad (2.196)$$

By momentum conservation the momenta of the photons resulting from the interaction are given by

$$\mathbf{k}_R = m\mathbf{k}_p + n\mathbf{k}_b \quad (2.197)$$

and thus

$$0 \stackrel{!}{=} (k_{R,\mu})^2 = (mk_{p,\mu} + nk_{b,\mu})^2 = 2mn k_{p,\mu} k_{b,\nu} \eta^{\mu\nu} = 4mn \omega_p \omega_b. \quad (2.198)$$

Equation (2.198) implies that as soon as the pulses do not overlap anymore, only contributions where  $m$  or  $n$  is zero can remain. A summary of all the 4-photon processes that are allowed in first order can be found in table 2.1.

### Second order contributions

It is possible that, the photons created in a 4-photon interaction are subject to 4-photon interaction again. As the intensity of these photons is orders of magnitude below the initial field intensity in the weak field case only processes involving one such photon need to be considered. The results can be seen in table (2.2).

## 2.7. The case of two colliding plane wave pulses

1st order 4-photon mixing processes						
(1)	(2)	(3)	(4)	Asymptotically allowed	Physical meaning	
$(\pm 1, 0)$	$(0, \pm 1)$	$(\mp 1, 0)$	$(0, \mp 1)$	y	scattering	
$(\pm 1, 0)$	$(0, \pm 1)$	$(\pm 1, 0)$	$(\mp 2, \mp 1)$	n	HH generation	
$(\pm 1, 0)$	$(0, \pm 1)$	$(0, \pm 1)$	$(\mp 1, \mp 2)$	n	HH generation	

**Table 2.1.:** Table of all the allowed 4-photon mixing possibilities in first order. The first four columns describe the contributions from each of the legs (number 1 to 4) in the interaction diagram. The notation  $(m, n)$  with  $m$  and  $n$  as defined in (2.193) is used, implying that, e.g.,  $(-1, -2)$  represents an outgoing photon with an energy equal to  $\omega_b + 2\omega_p$ . The column "Asymptotically allowed" indicates if the process is allowed in the asymptotic field according to (2.198).

It can be seen that once again most signals will disappear after the nonlinear interaction is as can be inferred from the asymptotically allowed column. Note however that there is a term that can theoretically enable the 4-photon interaction to create higher harmonics, see the last entry in table 2.2. However, this process is extremely suppressed since it requires photon splitting and high harmonic generation in the same step.

### 2.7.2. Contributions from 6-photon interaction

The same analysis can be performed for the 6-photon diagram resulting in table 2.3.

Here the computation of higher orders is omitted as they are orders of magnitude below even the 2nd order 4-photon scattering processes.

### 2.7.3. Analytical solution

Tables 2.1-2.3 list all relevant physical processes. However, not all processes contained can be observed due to further constraints in the underlying PDE. The work in [10] presents a calculation for first order corrections in the case, where the background pump pulse has near 0 frequency. A complete derivation of the solution can be found in [29] and thus is omitted here.

Recalling the Maxwell-Ampère law (2.180) and combining it with the Maxwell-Faraday law

$$\partial_t \vec{B} = -c \nabla \times \vec{E}, \quad (2.199)$$

## 2. State of the art

2nd order 4-photon mixing processes						
(1)	(2)	(3)	(4)	Asymptotically allowed	Physical meaning	
(±2, ±1)	(±1, 0)	(0, ±1)	(∓3, ∓2)	n	HH generation	
(±2, ±1)	(±1, 0)	(0, ∓1)	(∓3, 0)	y	HH g. + split	
(±2, ±1)	(∓1, 0)	(0, ±1)	(∓1, ∓2)	n	HH g. + split	
(±2, ±1)	(∓1, 0)	(0, ∓1)	(∓1, 0)	y	photon splitting	
(±2, ±1)	(±1, 0)	(±1, 0)	(∓4, ∓1)	n	HH generation	
(±2, ±1)	(±1, 0)	(∓1, 0)	(∓2, ∓1)	n	scattering on HH	
(±2, ±1)	(0, ±1)	(0, ∓2)	(∓2, 0)	y	split + HH g.	

Note: Symmetric processes that are obtained by exchanging  $m$  and  $n$  are omitted

**Table 2.2.:** Table of all the allowed 4-photon mixing possibilities in second order. The first four columns describe the contributions from each of the legs (number 1 to 4) in the interaction diagram. The notation  $(m, n)$  with  $m$  and  $n$  as defined in (2.193) is used, implying that, e.g.,  $(-1, -2)$  represents an outgoing photon with an energy equal to  $\omega_b + 2\omega_p$ . The column "Asymptotically allowed" indicates if the process is allowed in the asymptotic field according to (2.198).

it is found that  $\vec{E}$  must satisfy

$$\square \vec{E} = \vec{T}[\vec{E}, \vec{B}] = 4\pi \left[ \nabla \times \partial_t \vec{M} + \partial_t^2 \vec{P} - \nabla(\nabla \cdot \vec{P}) \right]. \quad (2.200)$$

Now, if only first order contributions from the scattering diagrams are considered (2.200) simplifies to

$$\square \vec{E} = \vec{T} \left[ \vec{E}^{(0)} \right], \quad (2.201)$$

where  $\vec{E}^{(0)}$  is the vacuum solution satisfying  $\square \vec{E}^{(0)} = 0$ . The resulting solution must therefore satisfy

$$\square \vec{E}^{(1)} = T \left[ E^{(0)} \right], \quad (2.202)$$

where

$$\vec{E} = \vec{E}^{(0)} + \vec{E}^{(1)}. \quad (2.203)$$

Equation (2.202) can be solved using a Green's function for the case of the collision between two coaxially counter-propagating Gaussian plane wave fields with a strong background, that does not oscillate, i.e.,

$$\vec{E}_p(\mathbf{x}) = \hat{p}_p A_p e^{-\left(k_p^\mu x_\mu / \omega_p \tau_p\right)^2} \cos k_p^\mu x_\mu, \quad (2.204)$$

2.7. The case of two colliding plane wave pulses

1st order 6-photon mixing processes							
(i)	(i)	(i)	(i)	(i)	(o)	Asympt. allowed	Physical meaning
(1, 0)	(0, 1)	(1, 0)	(1, 0)	(1, 0)	(4, 1)	n	HH generation
(1, 0)	(0, 1)	(1, 0)	(1, 0)	(0, 1)	(3, 2)	n	HH generation
(1, 0)	(0, 1)	(1, 0)	(0, 1)	(0, 1)	(2, 3)	n	HH generation
(1, 0)	(0, 1)	(0, 1)	(0, 1)	(0, 1)	(1, 4)	n	HH generation
(i)	(i)	(i)	(i)	(o)	(o)	Asympt. allowed	Physical meaning
(1, 0)	(0, 1)	(1, 0)	(1, 0)	(1, 0)	(2, 1)	n	HH gen. + scat.
(1, 0)	(0, 1)	(1, 0)	(1, 0)	(0, 1)	(3, 0)	y	HH gen. + scat.
(1, 0)	(0, 1)	(1, 0)	(0, 1)	(1, 0)	(1, 2)	n	HH gen. + scat.
(1, 0)	(0, 1)	(1, 0)	(0, 1)	(0, 1)	(2, 1)	n	HH gen. + scat.
(1, 0)	(0, 1)	(0, 1)	(0, 1)	(1, 0)	(0, 3)	y	HH gen. + scat.
(1, 0)	(0, 1)	(0, 1)	(0, 1)	(0, 1)	(1, 2)	n	HH gen. + scat.
(1, 0)	(0, 1)	(1, 0)	(1, 0)	(2, 0)	(1, 1)	n	HH gen. + merge
(1, 0)	(0, 1)	(1, 0)	(0, 1)	(2, 0)	(0, 2)	y	double HH gen.
(1, 0)	(0, 1)	(0, 1)	(0, 1)	(0, 2)	(1, 1)	n	HH gen. + merge
(i)	(i)	(i)	(o)	(o)	(o)	Asympt. allowed	Physical meaning
(1, 0)	(0, 1)	(1, 0)	(1, 0)	(1, 0)	(0, 1)	y	scattering
(1, 0)	(0, 1)	(0, 1)	(1, 0)	(0, 1)	(0, 1)	y	scattering

**Table 2.3.:** Table of all the allowed 6-photon mixing possibilities in first order. The first six columns describe the contributions from each of the legs in the interaction diagram. They are labeled (i) for an incoming and (o) for an outgoing photon. The notation  $(m, n)$  with  $m$  and  $n$  as defined in (2.193) has been used. Symmetric process, i.e., processes obtained by exchanging the (i) and (o) photons are omitted. The column "Asymptotically allowed" indicates if the process is allowed in the asymptotic field according to (2.198).

$$\vec{E}_b(\mathbf{x}) = \hat{p}_b A_b e^{-\left(k_b^\mu x_\mu / \omega_b \tau_b\right)^2}, \quad (2.205)$$

where the  $\hat{p}$  denote the normalized polarization vectors,  $A$  the amplitudes and  $\tau$  the width of the pulse. To do so it is required that  $A_b, A_p \ll E_{cr}$  and that it is valid to neglect the changes in the field strengths due to the frequency of the

## 2. State of the art

background, i.e.,  $\omega_p \tau_b \gg 1$ . Now, the solution of (2.202) takes on the form

$$\begin{aligned} \vec{E}^{(1)} = & A_p^2 \left[ \mathbf{C}_0 + \tilde{\mathbf{C}}_0 \right] \\ & + \sum_{l=1}^3 A_p^l e^{-l(k_p^\mu x_\mu / \omega_p \tau_p)^2} \left[ \mathbf{C}_l \sin(l k_p^\mu x_\mu) + \tilde{\mathbf{C}}_l \cos(l k_p^\mu x_\mu) \right], \end{aligned} \quad (2.206)$$

where

$$\begin{aligned} \mathbf{C}_0 &= -\frac{\alpha m^4}{180} \frac{1}{\sqrt{2\pi}} \vec{p}_{p,1} A_b \frac{\tau_p}{\tau_b} \phi_b e^{-\phi_b^2} (1 + \operatorname{erf}(\sqrt{2}\phi_b)), \\ \tilde{\mathbf{C}}_0 &= -\frac{\alpha m^4}{180\pi} \vec{p}_{p,1} E_b(k_b^\mu x_\mu) e^{-2\phi_p^2}, \\ \mathbf{C}_1 &= -\frac{\alpha m^4}{90\pi} \vec{p}_{b,1} A_b^2 \frac{\omega_p \tau_b \sqrt{\pi}}{\sqrt{2}} \frac{1 + \operatorname{erf}(\sqrt{2}\phi_b)}{2}, \\ \tilde{\mathbf{C}}_1 &= -\frac{\alpha m^4}{90\pi} \vec{p}_{b,1} E_b^2(k_b^\mu x_\mu), \\ \mathbf{C}_2 &= -\frac{\alpha m^4}{315\pi} \vec{p}_{b,2} A_b^3 \frac{\omega_p \tau_b \sqrt{\pi}}{\sqrt{3}} \frac{1 + \operatorname{erf}(\sqrt{3}\phi_b)}{2}, \\ \tilde{\mathbf{C}}_2 &= -\frac{\alpha m^4}{180\pi} \vec{p}_{p,1} E_b(k_b^\mu x_\mu) - \frac{\alpha m^4}{630\pi} \vec{p}_{b,2} E_b^3(k_b^\mu x_\mu), \\ \mathbf{C}_3 &= 0, \\ \tilde{\mathbf{C}}_3 &= -\frac{\alpha m^4}{1260\pi} \vec{p}_{p,2} E_b^2(k_b^\mu x_\mu), \end{aligned} \quad (2.207)$$

with  $\phi_i = k_i^\mu x_\mu / \omega_i \tau_i$  and the polarizations given by

$$\begin{aligned} \vec{p}_{b,1} &= c_{1,1} \hat{p}_b + c_{1,2} \hat{k}_b \times \hat{p}_b, \\ \vec{p}_{p,1} &= c_{1,1} \hat{p}_p + c_{1,2} \hat{k}_p \times \hat{p}_p, \\ \vec{p}_{b,2} &= c_{2,1} \hat{p}_b + c_{2,2} \hat{k}_b \times \hat{p}_b, \\ \vec{p}_{p,2} &= c_{2,1} \hat{p}_p + c_{2,2} \hat{k}_p \times \hat{p}_p, \end{aligned} \quad (2.208)$$

with the constants

$$\begin{aligned} c_{1,1} &= 8 \hat{p}_b \cdot \hat{p}_p, \\ c_{1,2} &= 14 \hat{p}_b \cdot \hat{k}_p \times \hat{p}_p, \\ c_{2,1} &= \frac{3}{2} c_{1,1}^2 + \frac{13}{49} c_{1,2}^2, \\ c_{2,2} &= \frac{13}{14} c_{1,1} c_{1,2}. \end{aligned} \quad (2.209)$$

### *2.7. The case of two colliding plane wave pulses*

As to be expected only the signals contained in table 2.1 and table 2.3 are present. From (2.206) it is understood that some processes listed in tables 2.1 and 2.3 are not present in the asymptotic field, even though in the tables these processes are considered viable in the far field. It is clearly visible in the factors above that only the scattering signal and the second harmonic will survive asymptotically.



# 3. State of the art in numerical mathematics

Having defined the problem of the nonlinear vacuum in a framework of partial differential equations it is time to turn to the solution of these. There are a myriad of algorithms to solve PDEs [30]. In this chapter a short introduction to a set of the most prominent numerical algorithms with examples in 1D is given and their suitability for the solution of the nonlinear Maxwell equations in vacuum is discussed.

## 3.1. Classification of PDE

Before the PDE solving algorithms are introduced it is important to understand the basic types of PDEs and their properties, as their behavior heavily influences the suitability of the schemes. In this section only a short overview of the relevant properties for the problem of the QED vacuum is discussed. For a more in depth discussion of the topic see for example [31].

### Linear vs. nonlinear PDEs

If  $T[u, t]$  represents the time evolution of a function  $f(x, t)$  such that

$$f(x, t) = T[f(x, 0), t], \quad (3.1)$$

then a PDE is called linear if and only if for all of its solutions  $u_i$  it holds that

$$T \left[ \sum_i a_i u_i(x, 0), t \right] = \sum_i a_i T[u_i(x, 0), t] = \sum_i a_i u_i(x, t) \quad \forall a_i \in \mathbb{R}. \quad (3.2)$$

Equation (3.2) implies, that if  $u_1$  and  $u_2$  are solutions to the PDE then  $u_1 + u_2$  is also a solution. An example of such a behavior are the Maxwell equations in classical vacuum.

### 3. State of the art in numerical mathematics

#### Elliptic, parabolic and hyperbolic PDEs

Linear PDEs are further classified into one of three classes: elliptic, parabolic and hyperbolic. To classify the PDEs are written as

$$0 = A \frac{\partial^2 u}{\partial t^2} + 2B \frac{\partial^2 u}{\partial t \partial x} + C \frac{\partial^2 u}{\partial x^2} + \text{Lower order terms}. \quad (3.3)$$

With these parameters at hand the classification becomes

- i.  $B^2 - AC < 0$ : Elliptic PDE. An example of a elliptic PDE is the the Helmholtz equation.
- ii.  $B^2 - AC = 0$ : Parabolic PDE. An example of a parabolic PDE is the heat diffusion equation.
- iii.  $B^2 - AC > 0$ : Hyperbolic PDE. An example of hyperbolic PDEs are the time dependent Maxwell equations.

Steady state solutions to elliptic equations are completely described by their boundary values ( $u(0), u(T)$ ). They react immediately to perturbations of boundaries. Similarly, solutions to parabolic equations depend on the boundary values, but they also require an initial setup from which they will diffuse to the steady state solution. Finally, hyperbolic equations do not have steady state solutions apart from a constant background ( $u(x, t) = c \in \mathbb{R}$ ), as any perturbation propagates. For example consider the differential equation

$$\partial_t u + a \partial_x u = 0. \quad (3.4)$$

Using the substitution  $\tilde{x} = x - at$  it is obtained that

$$\partial_{\tilde{x}} u = 0 \quad (3.5)$$

and thus the solution remains constant along the characteristic line  $c = x - at$ . In other words, this implies that the initial form  $u(x, 0)$  will travel in  $x$ -direction with a ‘speed’ of  $a$ ,

$$u(x, t) = u(x - at, 0). \quad (3.6)$$

#### Mixed PDE types

Nonlinear PDEs cannot be categorized as neatly as linear ones due to the fact that their properties may change during time integration. For example consider the equation

$$\partial_t^2 u + u \partial_x^2 u = 0. \quad (3.7)$$

### 3.2. The finite element method (FEM)

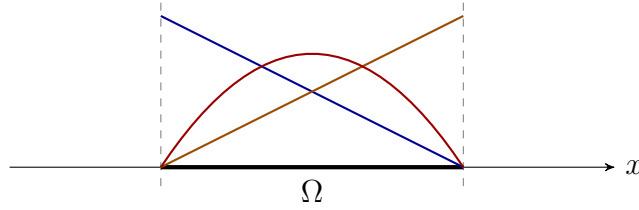


**Figure 3.1.:** Sketch of the domain on which the FEM is used and the corresponding basis functions.

If  $u$  is negative (3.7) is hyperbolic and if  $u$  is positive it is parabolic. This leads to several effects, such as, self-steepening. However, nonlinearity does not necessarily imply that the equation is of mixed type. For example, the modified Maxwell equations described in chapter 2 remain hyperbolic, since the nonlinear corrections derived from the Heisenberg-Euler Lagrangian are not strong enough to significantly influence the  $B^2 - AC$  property.

## 3.2. The finite element method (FEM)

The most commonly used algorithm for solving PDEs is the finite element method. While it is a strong formalism that can handle multiple dimensions its main properties can be already understood in the 1D case. As such only its implementation on a 1 dimensional problem is discussed here.

In its most elementary form the finite element method projects a given function  $f$  onto a set of basis functions  $b_i$ , such that

$$f(x) \approx \sum_i a_i b_i(x) \quad (3.8)$$

in a given domain  $\Omega \subset \mathbb{R}$  with  $a_i \in \mathbb{R}$ . The basis functions are chosen in such a way that

$$\frac{\partial b_i}{\partial x} = \sum_j c_{j,i} b_j. \quad (3.9)$$

In matrix notation  $f(x) \approx \vec{a} \cdot \vec{b}(x)$  it is obtained that

$$\partial_x f(x) \approx (\mathbf{C} \vec{a}) \cdot \vec{b}(x), \quad (3.10)$$

where  $\mathbf{C}$  is the matrix containing the  $c_{i,j}$  and thus a simple partial differential equation of the form

$$\partial_t f = \partial_x f \quad (3.11)$$

becomes

$$\partial_t \vec{a} = \mathbf{C} \vec{a}, \quad (3.12)$$

### 3. State of the art in numerical mathematics

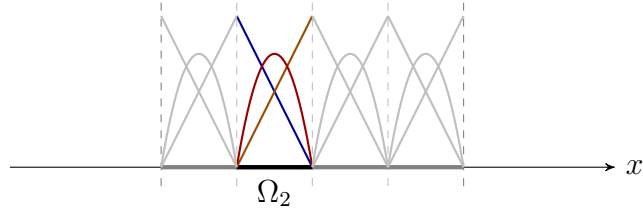


**Figure 3.2.:** Sketch of a subdivided domain on which the FEM is used and the corresponding basis functions for each sub-domain.

when the time independence of the basis functions is taken into account. This final ODE (3.12) can now be solved by any standard numerical algorithm. The main problem that arises when transforming a PDE to an ODE in this manner is that the accuracy of the projection is limited by the number of basis functions being considered. To increase the accuracy without increasing the amount of basis functions the domain is divided into smaller sub-domains with each having its own set of basis polynomials.

This method avoids the quadratic scaling of including a larger number of basis functions at the cost of having to deal with the boundary exchanges between the different subdomains. The boundary exchange is not problematic for elliptic and parabolic equations, since the transport of intensity from one cell to the next is either nonexistent or severely limited. In the case of hyperbolic equations, however, stiffening becomes a relevant factor as the correct projection onto finite elements is less important than the correct transport along the characteristic lines.

Furthermore, one of the main advantages of using the FEM is its adaptability to any shape and size of the problem to be simulated. For example, adaptability is useful when simulating the heat distribution in a solid piece of machinery, as the domains can be adapted to the shape of the machine. The shape adaptability of the FEM algorithm is, however, useless when simulating structure free settings such as the nonlinear vacuum.

Lastly, nonlinearities tend to cause the system to get out of bound, i.e., the nonlinearity caused by the field configuration is not contained in the basis. For example the PDE

$$\partial_t f = (1 + \epsilon f^2) \partial_x f, \quad (3.13)$$

when projected onto  $[0, 1]$  using the basis  $\mathfrak{B} = \{x, 1 - x, x(1 - x)\}$  gives rise to a nonlinearity of magnitude  $a_3 \epsilon x^2(1 - x)^2 \notin \mathfrak{B}$ . Thus, in every step new projections are needed for every subdomain. While feasible this results in an considerable increase in computational load.

### 3.3. The three wave mixing method

Another way to approach a nonlinear PDE is to attempt to choose the basis functions in dependence of the initial setup. An example is the so called three wave mixing method. The easiest way to understand three wave mixing is to consider a nonlinear crystal. A seed and a pump laser beam are inserted into it and interact with the crystal generating a third beam of an energy specified by the nature of nonlinearities of the crystal. It is therefore sufficient to consider the three waves as basis elements as the interaction does not generate any other effects. All that remains is to obtain the ordinary differential equations describing the interactions between the different beam strengths and solve them.

The ability to simplify a problem to the interaction of a few amplitudes is the strongest and at the same time weakest feature of the algorithm, as the allowed channels will be in stone thus requiring a large amount of knowledge at the beginning of the simulation.

Furthermore, when considering finite width pulses instead of beams the problem becomes more complex, as the dynamics of the envelope needs to be taken account. Also, simulating in higher dimensions is problematic as effects such as dispersion and diffraction need to be considered. They require that a considerably large basis taking into account all the possible directions a wave may take is used. Alternatively, degrees of freedom to account for the direction of the pulses can be introduced. This requires the amplitudes to become complex for the propagation in 2D and quaternions for the propagation in 3D.

### 3.4. The Yee algorithm

The Yee algorithm, as published in 1966 by Kane S. Yee [32], is designed for second order integration of the Maxwell equations. This is achieved by both time- and space-staggering of the electromagnetic fields. The main idea of the algorithm is to use central differences for the finite difference operations instead of forward or backwards propagators.

The staggering in time is realized by computing the electric and displacement fields at full time-steps, and the magnetizing and magnetic fields at half-steps. The staggering in space is achieved by displacing the grid point position of the fields. The result of staggering can be seen in figure 3.3.

The second order accuracy can now be easily obtained since, e.g., the representation of the derivation of  $H_y$  in  $x$ -direction required for the computation of  $E_z$  now becomes:

$$\frac{H_y|_{x_0+0.5\Delta} - H_y|_{x_0-0.5\Delta}}{\Delta} = \frac{\sum_{n=0}^{\infty} \frac{(0.5\Delta)^n}{n!} \partial_x^{(n)} H_y|_{x_0} - \sum_{n=0}^{\infty} \frac{(-0.5\Delta)^n}{n!} \partial_x^{(n)} H_y|_{x_0}}{\Delta}$$

### 3. State of the art in numerical mathematics

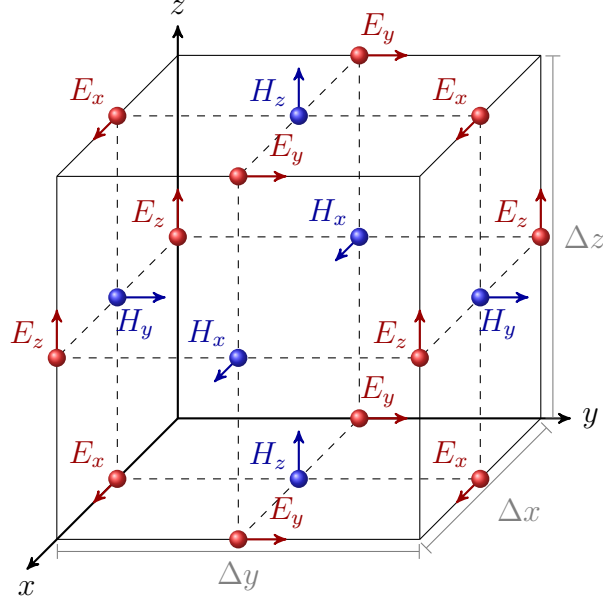


**Figure 3.3.:** Sketch of the positioning of the field data points in the Yee algorithm.

$$= \frac{\partial_x H_y \Delta + \mathcal{O}(\Delta^3)}{\Delta} = \frac{\partial H_y}{\partial x} \Big|_{x_0} + \mathcal{O}(\Delta^2). \quad (3.14)$$

While the Yee algorithm is a popular choice when simulating electromagnetic waves due to its implicitness and relative stability [33] it cannot easily reproduce nonlinearities. The difficulties to reproduce nonlinearities are not only due to the implicitness of the Yee scheme not correctly reproducing the propagation of said nonlinearities, as this may be solved by the use of a sub-cycling scheme. Mainly, the problem resides in the fact that due to the staggering computing the nonlinearities at any given point requires several interpolations in space and extrapolations in time.

## 3.5. The general finite difference case

The Yee algorithm can be generalized onto a non-staggered grid by approximating the differential operators in space using the Taylor series and solving the resulting ODE using an implicit solver. The Taylor series of the function  $f(x + k \Delta x)$  is

$$f(x + k \Delta x) = f(x) + \Delta x k f'(x) + \frac{1}{2} \Delta x^2 k^2 f''(x) + \frac{1}{6} \Delta x^3 k^3 f^{(3)}(x) + \dots, \quad (3.15)$$

### 3.5. The general finite difference case

in matrix notation it becomes

$$\begin{pmatrix} f(x-4\Delta x) \\ f(x-3\Delta x) \\ f(x-2\Delta x) \\ f(x-\Delta x) \\ f(x) \\ f(x+\Delta x) \\ f(x+2\Delta x) \\ f(x+3\Delta x) \\ f(x+4\Delta x) \end{pmatrix} \approx \frac{1}{120} \begin{pmatrix} 120 & -480 & 960 & -1280 & 1280 & -1024 \\ 120 & -360 & 540 & -540 & 405 & -243 \\ 120 & -240 & 240 & -160 & 80 & -32 \\ 120 & -120 & 60 & -20 & 5 & -1 \\ 120 & 0 & 0 & 0 & 0 & 0 \\ 120 & 120 & 60 & 20 & 5 & 1 \\ 120 & 240 & 240 & 160 & 80 & 32 \\ 120 & 360 & 540 & 540 & 405 & 243 \\ 120 & 480 & 960 & 1280 & 1280 & 1024 \end{pmatrix} \begin{pmatrix} f(x) \\ \Delta x f'(x) \\ \Delta x^2 f''(x) \\ \Delta x^3 f^{(3)}(x) \\ \Delta x^4 f^{(4)}(x) \\ \Delta x^5 f^{(5)}(x) \end{pmatrix}. \quad (3.16)$$

This formulation is over-defined. Thus there is no expression for the first derivative  $f'$  that is independent of the position  $x+k\Delta x$  of the values  $f(x+k\Delta x)$  considered. For example considering the quadratic matrix relating  $f(x)$  and  $f(x+\Delta x)$  to  $f(x)$  and  $f'(x)$

$$\begin{pmatrix} \vdots \\ f(x) \\ f(x+\Delta x) \\ \vdots \end{pmatrix} \approx \frac{1}{120} \begin{pmatrix} \vdots & \vdots & \ddots \\ 120 & 0 & \dots \\ 120 & 120 & \dots \\ \vdots & \vdots & \ddots \end{pmatrix} \begin{pmatrix} f(x) \\ f'(x) \\ \vdots \end{pmatrix} \quad (3.17)$$

and solving for  $f'(x)$  results in the well-known upwind biased finite difference approximation for the first derivative

$$f'_{(1,0)}(x) = \frac{f(x+\Delta x) - f(x)}{\Delta x} \quad (3.18)$$

and considering the quadratic matrix relating  $f(x)$  and  $f(x-\Delta x)$  to  $f(x)$  and  $f'(x)$  results in the downwind biased finite difference approximation for the first derivative

$$f'_{(0,-1)}(x) = \frac{f(x) - f(x-\Delta x)}{\Delta x} \quad (3.19)$$

Note the notation  $f'_{(n,m)}(x)$ , where  $m$  denotes the lowest  $k$  considered and  $n$  the highest. These approximations for  $f'$  can be generally be written as

$$\mathcal{D}f = f'_{(n,m)}(x) = \frac{1}{\Delta x} \sum_{i=n}^m \mathcal{S}_i f(x+i\Delta x) \quad (3.20)$$

where  $\vec{\mathcal{S}}$  is the derivative stencil.  $\vec{\mathcal{S}}$  depends solely on the choice of  $n$  and  $m$  (see table 3.1).

Note, that for all symmetric stencils  $n = -m$  the relation  $\mathcal{S}_0 = 0$  holds. This implies that the derivative  $f'_{(n,m)}$  at position  $x$  does not involve  $f(x)$ . This in turn this causes the system to become numerically unstable. As a consequence a biased scheme or a staggered grid have to be used.

3. State of the art in numerical mathematics

$\mathcal{O} = 1$	-1	0	1		
	-1	1			
		-1	1		

$\mathcal{O} = 2$	-2	-1	0	1	2		
	$\frac{1}{2}$	-2	$\frac{3}{2}$				
		$-\frac{1}{2}$	0	$\frac{1}{2}$			
			$-\frac{3}{2}$	2	$-\frac{1}{2}$		

$\mathcal{O} = 3$	-3	-2	-1	0	1	2	3		
	$-\frac{1}{3}$	$\frac{3}{2}$	-3	$\frac{11}{6}$					
		$\frac{1}{6}$	-1	$\frac{1}{2}$	$\frac{1}{3}$				
			$-\frac{1}{3}$	$-\frac{1}{2}$	1	$-\frac{1}{6}$			
				$-\frac{11}{6}$	3	$-\frac{3}{2}$	$\frac{1}{3}$		

$\mathcal{O} = 4$	-4	-3	-2	-1	0	1	2	3	4		
	$\frac{1}{4}$	$-\frac{4}{3}$	3	-4	$\frac{25}{12}$						
		$-\frac{1}{12}$	$\frac{1}{2}$	$-\frac{3}{2}$	$\frac{5}{6}$	$\frac{1}{4}$					
			$\frac{1}{12}$	$-\frac{2}{3}$	0	$\frac{2}{3}$	$-\frac{1}{12}$				
				$-\frac{1}{4}$	$-\frac{5}{6}$	$\frac{3}{2}$	$-\frac{1}{2}$	$\frac{1}{12}$			
					$-\frac{25}{12}$	4	-3	$\frac{4}{3}$	$-\frac{1}{4}$		

$\mathcal{O} = 5$	-5	-4	-3	-2	-1	0	1	2	3	4	5		
	$-\frac{1}{5}$	$\frac{5}{4}$	$-\frac{10}{3}$	5	-5	$\frac{137}{60}$							
		$\frac{1}{20}$	$-\frac{1}{3}$	1	-2	$\frac{13}{12}$	$\frac{1}{5}$						
			$-\frac{1}{30}$	$\frac{1}{4}$	-1	$\frac{1}{3}$	$\frac{1}{2}$	$-\frac{1}{20}$					
				$\frac{1}{20}$	$-\frac{1}{2}$	$-\frac{1}{3}$	1	$-\frac{1}{4}$	$\frac{1}{30}$				
					$-\frac{1}{5}$	$-\frac{13}{12}$	2	-1	$\frac{1}{3}$	$-\frac{1}{20}$			
						$-\frac{137}{60}$	5	-5	$\frac{10}{3}$	$-\frac{5}{4}$	$\frac{1}{5}$		

**Table 3.1.:** Stencils for derivatives for finite differences up to 5-th order.

### 3.5. The general finite difference case

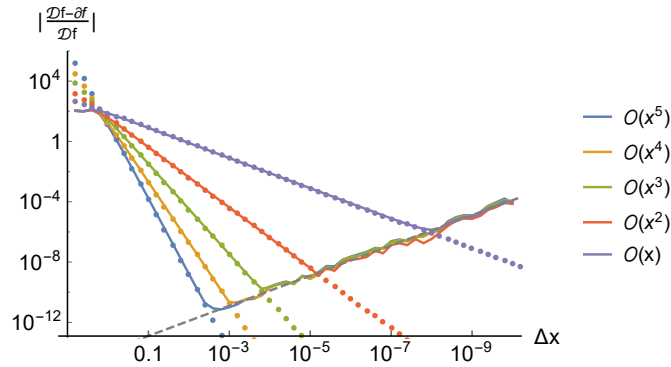


**Figure 3.4.:** Evolution of the relative error for the different order stencils for the first derivatives (solid lines). For comparison the evolution of the basic powers normed to fit exactly at  $\Delta x = 1$  (dotted). The gray dashed line represents the round off error, which grows in  $\mathcal{O}(x)$  and the prefactor was manually fitted to the data. The test case function was  $f(x) = \sin(x)$  on the domain  $[0, \pi]$

A result of the application of these stencils on the computation of the derivative can be seen in figure 3.4 for the case of  $f(x) = \sin(x)$  and  $\Delta x$  variable.

Two things are worth noting here, first for  $\Delta x > 1$  the relative error is of order 1. This is to be expected since at this point the Taylor series does not converge. Second, the computation does not improve infinitely according to the order of the remainder in the Taylor series, but has a hard limit due to the “round off” error. A similar investigation can be made within the same parameters but now varying the bias  $n - m$  instead of the order of the stencil. The results can be seen in figure 3.5.

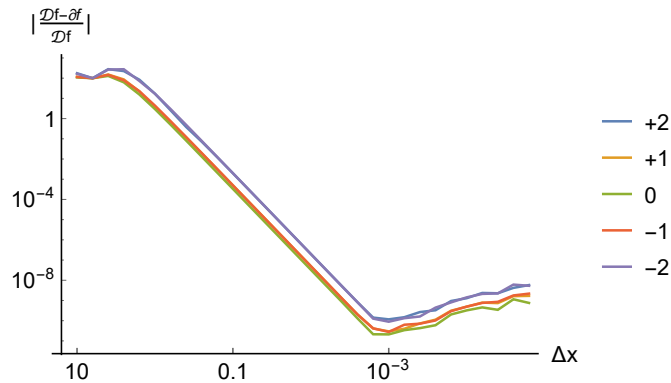


**Figure 3.5.:** Evolution of the relative error for the different biased stencils for the first derivatives of order 4. The test case function was  $f(x) = \sin(x)$  on the domain  $[0, \pi]$

In figure 3.5 it can be seen that the errors all scale the same but the stronger the bias the more susceptible to numerical instabilities the latter become. The

### 3. State of the art in numerical mathematics

analysis, however, do not reflect the systematic phase velocity error that is also introduced by the usage of biased stencils. The clearest way of seeing this is considering the fully unilateral stencil (w.l.o.g.  $n = 0$ ). Since then the computation of the derivative using (3.20) does not consider the values of the wave to the right of the lattice point where the derivative is being computed, it is mathematically impossible for it to propagate finite pulses traveling from right to left. This may be useful to suppress reflection caused by non-homogeneous lattices but is non-physical.

#### 3.5.1. The Nyquist frequency

While it can be shown that (3.15) converges for any  $\Delta x < 1$ , it can converge to a value that is not the derivative at that point. The problem resides in the fact that given a fixed sampling rate, two distinct sinusoidal waves can have the exact same values. To illustrate this the example of a sine with a wavelength of 0.5 and a negative sine with a wavelength of 0.125, both sampled with a frequency of 0.1 (see figure 3.6), can be considered. With these parameters the values for both sines are the same at all sample points and the Taylor series converges against the value of the derivative of the sine wave with wavelength 0.5.

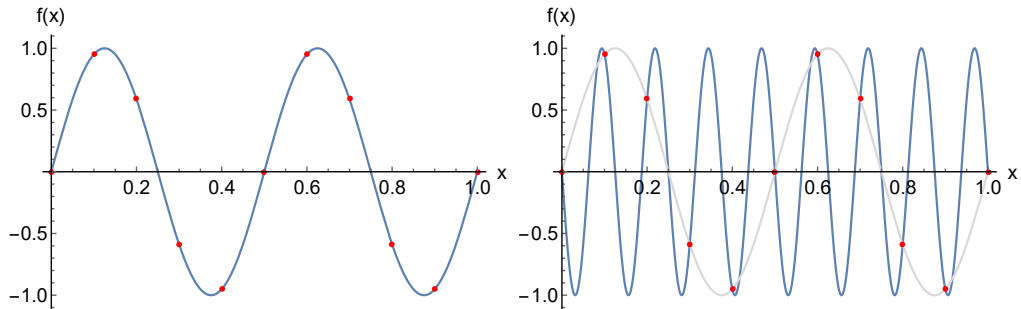


**Figure 3.6.:** **Left:** Plot of a sinus function (solid) fitting a set of 11 data points. **Right:** Plot of an alternative higher frequency sinus function (solid) fitting a set of the same 11 data points.

Further analysis show that the Taylor series will only converges against the derivative of the function if the additional restriction

$$f \leq f_{Ny} = \frac{f_{\text{Sampling}}}{2} \quad (3.21)$$

is fulfilled for all involved frequencies  $f$ . Thus, it makes no sense to improve the stencils beyond the point, where the "round-off" error dominates the error when computing the derivative for  $\Delta x/k = 0.5$ .

### 3.5.2. Consistency, stability, convergence

In order to prove the consistency, stability and convergence of the finite difference scheme the assumption is made, that the algorithm used for the time integration of the ODEs is consistent and stable.

The requirement of consistency is fulfilled for all analytic functions as can be read in any introductory analysis book, e.g. [34],

$$\begin{aligned} \lim_{\Delta x \rightarrow 0} f'_{(n,m)}(x) &= \lim_{\Delta x \rightarrow 0} \frac{1}{\Delta x} \sum_{i=n}^m \mathcal{S}_i f(x + i\Delta x) \\ &\stackrel{(3.16)}{=} \lim_{\Delta x \rightarrow 0} \frac{1}{\Delta x} (\Delta x f'(x) + \mathcal{O}(\Delta x^{n-m})) = f'(x). \end{aligned} \quad (3.22)$$

Consistency however is only fulfilled for the analytical properties of the numerical scheme but not for its implementation on the computer due to the round-off error

$$roE(x) \sim f(x) - rd(f(x)), \quad (3.23)$$

where  $rd(f(x))$  is the rounding of  $f(x)$  to the working precision of the computer. Inserting this error function (3.23) into (3.22) leads to

$$\begin{aligned} \lim_{\Delta x \rightarrow 0} f'_{(n,m)}(x) &= \lim_{\Delta x \rightarrow 0} \frac{1}{\Delta x} \sum_{i=n}^m \mathcal{S}_i f(x + i\Delta x) \\ &= \lim_{\Delta x \rightarrow 0} \frac{1}{\Delta x} (\Delta x f'(x) \pm roE(x) + \mathcal{O}(\Delta x^{n-m})) \\ &= f'(x) \pm \lim_{\Delta x \rightarrow 0} \frac{roE(x)}{\Delta x} = \pm\infty. \end{aligned} \quad (3.24)$$

Thus, the expression for  $f'_{(n,m)}(x)$  is only consistent to the point, where the round-off error becomes dominant, see figure 3.4. Stability, i.e., the fact that the time propagation values at the sample points are bound by a constant  $C(T)$  meaning

$$\sum_i f(i \Delta x, t)^2 \leq C(T)^2 \sum_i f(i \Delta x, 0)^2 \quad \forall t < T \quad (3.25)$$

is a bit more complicated to prove. For simplicity the periodic boundary case is considered. Then,

$$\begin{aligned} \partial_t \sum_i f(i \Delta x, t)^2 &= 2 \sum_i f(i \Delta x, t) \partial_t f(i \Delta x, t) \\ &\leq \sum_i f(i \Delta x, t) K \sum_{j=m}^n \mathcal{S}_j f(i\Delta x + j\Delta x, t) \end{aligned}$$

### 3. State of the art in numerical mathematics

$$\begin{aligned}
&= K \sum_{j=m}^n \mathcal{S}_j \sum_i f(i \Delta x, t) f(i \Delta x + j \Delta x, t) \\
&\leq K \sum_{j=m}^n \mathcal{S}_j \sum_i \max_i f(i \Delta x, t)^2 \\
&= K \sum_i \max_i f(i \Delta x, t)^2 \sum_{j=m}^n \mathcal{S}_j \\
&= K \sum_i \max_i f(i \Delta x, t)^2 0 \\
&= 0.
\end{aligned} \tag{3.26}$$

Performing an analogous computation for the lower bound results in

$$\partial_t \sum_i f(i \Delta x, t)^2 \geq 0 \tag{3.27}$$

and thus

$$\partial_t \sum_i f(i \Delta x, t)^2 = 0. \tag{3.28}$$

This implies

$$\sum_i f(i \Delta x, t)^2 = \text{const.}, \tag{3.29}$$

implying, that nothing is created or destroyed by the scheme through derivation. Thus, the use of stencils results in a stable scheme.

With stability and consistency insured it follows that the scheme converges against the analytic solution and thus the results obtained by the finite difference algorithm can be taken as valid within the errors  $\epsilon$  introduced by the approximations. This means, that if  $f(x, t)$  is the solution to the PDE and  $f_{fd}(x, t)$  is the result of the finite difference algorithm, then

$$|f(x, t) - f_{fd}(x, t)| \leq \epsilon t \quad \forall t, x \in \mathbb{R}. \tag{3.30}$$

## 4. Programming concepts

There are several considerations to be made and constraints that need to be taken into account when implementing numerical algorithms on the computer. This chapter gives a brief description of the concepts that are relevant for the numerical algorithm presented in chapter 5 and that are used in later chapters.

### 4.1. Key computational concepts

**Finite digit representation:** While most real numbers possess an infinite number of digits in their decimal representation, a computer can hold a finite number of digits. For the data type used throughout this thesis (long double in the IEEE 64 bit standard) it is 19 digits. The finite number of digits has two consequences. Firstly, no matter how good the numerical algorithm or the analytic work done beforehand the results never have a better relative precision than  $10^{-19}$ . Secondly, computing the difference between two largely equal numbers causes the relative error of the difference w.r.t. the exact difference to increase exponentially with the number of digits that are the same.

**Core hours:** As larger simulations run on multiple cores the absolute time needed for a simulation depends on the number of cores that are used. To enable a mostly core number independent measurement of the run-time the total simulation time is multiplied by the total number of cores used, yielding the run time in so called core hours. Note, that this is not an ideal measurement as it strongly depends on the CPU used.

**Front end/back end:** When developing a larger algorithm it is crucial to differentiate between front end, the set of functions a user can use, and back end, the functions that run in the background. Ideally, the implementation architecture is devised so, that the user making use of the front end functions cannot do anything wrong and does not need any deeper understanding of the algorithm.

**C++ code vs. machine code:** There is a significant difference between C++ code and the set of instructions for the CPU derived from it. This difference between both codes becomes even more pronounced when the optimizer for the compiler is used. Ideas, that may only require a couple of lines to implement can result in long code and vice versa. A couple of examples are power, exponential and trigonometric functions or the multiplication of larger sets of data to compute

#### 4. Programming concepts

the inverse of a matrix. Thus, the latter operations and structures need to be avoided whenever possible.

**Computational load:** Every action performed on the computer result in a set of instructions, that need to be carried out by the CPU. There is a correlation between how many actions have to be performed for each step and how long it takes the CPU to perform them. An example for such a correlation is the order of a stencil used for a derivative vs. the number of points used in the discretization. Different combinations of grid size and stencil order result in the same numerical accuracy at different operational costs. It is thus important to find the best combination for the desired parameters.

**Scaling:** When designing an algorithm it is important to also consider how its computational load scales with increasing problem size. Consider for example charged particle interaction. If only two particles are present their interaction can be computed without problems. However, more and more particles cause the number of interactions to be computed to grow faster than exponentially. This is always the case for problems with infinite interaction range, i.e., each data point influences every other data point. It is thus very important to avoid such couplings in the implemented numerical scheme.

### 4.2. Parallel machines

To develop efficient code the first thing that needs to be taken into consideration is that a computer is not a single unit, but rather a set of communicating components (see figure 4.1). For example, the addition of two numbers requires the control unit in the CPU to load the two numbers into the cache, order the arithmetic logical unit to add them together and finally order the display of the result.

Ideally all the data would be always stored in the cache, such that the communication in and out of the CPU would be limited to the input at the beginning and output at the end of the simulation. Sadly, the storage capacity of the cache is severely limited (on modern computers it is about 3-4 MB). Thus, it is required to load and save data through the BUS into the RAM. The main point to consider is, that the cache loading is not performed for each value, but for entire data and instruction batches at a time. Therefore, it is efficient to store data for a set of operations that are performed in chronological order as close as possible in memory space.

The data management in the memory becomes more complex when the concept of multiple CPUs working at the same time is introduced. Even if they all have access to the same set of RAM, which is not always the case, they may want to access and modify the same set of data at the same time, which leads to undefined behavior. This is remedied by making redundant copies of data required by more

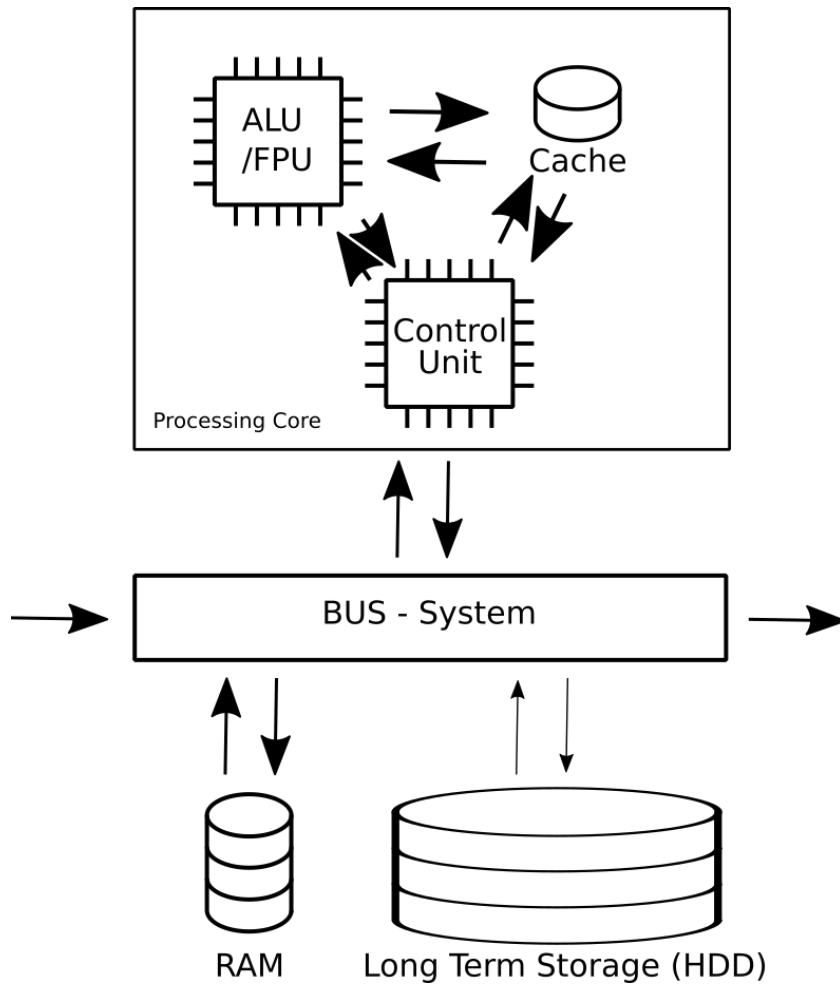


**Figure 4.1.:** Sketch of the strongly simplified basic architecture of a modern computer

#### *4. Programming concepts*

than one thread and forcing synchronicity at certain steps in the simulation. It is thus a key aspect of any algorithm designed to run on larger sets of interdependent data to have the ability to incorporate synchronization barriers.

# 5. The quantum vacuum simulation algorithm for the Heisenberg-Euler Lagrangian

An efficient numerical scheme is derived starting from the modified Maxwell equations as derived in section 2.5, and using a variation of the algorithm presented in 3.5. The analytic properties of the resulting algorithm are derived and discussed. The specific difficulties concerning the implementation of the algorithm are briefly discussed.

## 5.1. Reformulation of the Maxwell equations

The first step is to merge the two modified Maxwell equations derived in 2.5 and turn them into one single PDE, that describes the whole dynamics of the system. Recalling (2.179) it is known that

$$\partial_t \vec{B} = -\nabla \times \vec{E}, \quad (5.1)$$

$$\partial_t (\vec{E} + \vec{P}) = \nabla \times (\vec{B} - \vec{M}). \quad (5.2)$$

For the time derivative of  $\vec{P}$  in (5.2), using the chain rule, it is obtained that

$$\partial_t \vec{P} = \mathbf{J}_{\vec{P}}(\vec{E}) \partial_t \vec{E} + \mathbf{J}_{\vec{P}}(\vec{B}) \partial_t \vec{B}, \quad (5.3)$$

where  $\mathbf{J}$  is the Jacobi matrix, which is defined as

$$\mathbf{J}_{\vec{P}}(\vec{E}) = \begin{pmatrix} \frac{\partial P_x}{\partial E_x} & \frac{\partial P_x}{\partial E_y} & \frac{\partial P_x}{\partial E_z} \\ \frac{\partial P_y}{\partial E_x} & \frac{\partial P_y}{\partial E_y} & \frac{\partial P_y}{\partial E_z} \\ \frac{\partial P_z}{\partial E_x} & \frac{\partial P_z}{\partial E_y} & \frac{\partial P_z}{\partial E_z} \end{pmatrix}. \quad (5.4)$$

With the rotation of  $\vec{M}$  rewritten as

$$\nabla \times \begin{pmatrix} M_x \\ M_y \\ M_z \end{pmatrix} = \begin{pmatrix} \partial_y M_z - \partial_z M_y \\ \partial_z M_x - \partial_x M_z \\ \partial_x M_y - \partial_y M_x \end{pmatrix} \quad (5.5)$$

5. The quantum vacuum simulation algorithm for the Heisenberg-Euler Lagrangian

$$\begin{aligned}
&= \underbrace{\begin{pmatrix} 0 & 0 & 0 \\ 0 & 0 & -1 \\ 0 & 1 & 0 \end{pmatrix}}_{\mathbf{Q}_x} \partial_x \vec{M} + \underbrace{\begin{pmatrix} 0 & 0 & 1 \\ 0 & 0 & 0 \\ -1 & 0 & 0 \end{pmatrix}}_{\mathbf{Q}_y} \partial_y \vec{M} + \underbrace{\begin{pmatrix} 0 & -1 & 0 \\ 1 & 0 & 0 \\ 0 & 0 & 0 \end{pmatrix}}_{\mathbf{Q}_z} \partial_z \vec{B} \\
&= \sum_{j \in \{x,y,z\}} \mathbf{Q}_j \partial_j \vec{M}, \tag{5.6}
\end{aligned}$$

the chain rule can be used to rewrite the derivative in space yielding

$$\nabla \times \vec{M} = \sum_{j \in \{x,y,z\}} \mathbf{Q}_j \left[ \mathbf{J}_{\vec{M}}(\vec{E}) \partial_j \vec{E} + \mathbf{J}_{\vec{M}}(\vec{B}) \partial_j \vec{B} \right]. \tag{5.7}$$

Inserting (5.3) and (5.7) in (5.2) results in

$$\begin{aligned}
&\partial_t \vec{E} + \mathbf{J}_{\vec{P}}(\vec{E}) \partial_t \vec{E} + \mathbf{J}_{\vec{P}}(\vec{B}) \partial_t \vec{B} \\
&= \sum_{j \in \{x,y,z\}} \mathbf{Q}_j \left[ -\mathbf{J}_{\vec{M}}(\vec{E}) \partial_j \vec{E} + (\mathbf{1}_3 - \mathbf{J}_{\vec{M}}(\vec{B})) \partial_j \vec{B} \right]. \tag{5.8}
\end{aligned}$$

Introducing the electromagnetic vector  $\vec{u}$  as

$$\vec{u} = \begin{pmatrix} \vec{E} \\ \vec{B} \end{pmatrix}, \tag{5.9}$$

equation (5.8) can be written as

$$(\mathbf{1}_3 + \mathbf{J}_{\vec{P}}(\vec{E}) \quad \mathbf{J}_{\vec{P}}(\vec{B})) \partial_t \vec{u} = \sum_{j \in \{x,y,z\}} \mathbf{Q}_j (\mathbf{J}_{\vec{M}}(\vec{E}) \quad \mathbf{1}_3 - \mathbf{J}_{\vec{M}}(\vec{B})) \partial_j \vec{u}. \tag{5.10}$$

Making use of (5.9) equation (5.1) can be reformulated as

$$(\mathbf{0}_3 \quad \mathbf{1}_3) \partial_t \vec{u} = \sum_{j \in \{x,y,z\}} -\mathbf{Q}_j (\mathbf{1}_3 \quad \mathbf{0}_3) \partial_j \vec{u}, \tag{5.11}$$

which combined with (5.10) results in the PDE

$$\begin{aligned}
&\left[ \mathbf{1}_6 + \begin{pmatrix} \mathbf{J}_{\vec{P}}(\vec{E}) & \mathbf{J}_{\vec{P}}(\vec{B}) \\ \mathbf{0}_3 & \mathbf{0}_3 \end{pmatrix} \right] \partial_t \vec{u} \\
&= \sum_{j \in \{x,y,z\}} \begin{pmatrix} -\mathbf{Q}_j \mathbf{J}_{\vec{M}}(\vec{E}) & \mathbf{Q}_j - \mathbf{Q}_j \mathbf{J}_{\vec{M}}(\vec{B}) \\ -\mathbf{Q}_j & \mathbf{0}_3 \end{pmatrix} \partial_j \vec{u}. \tag{5.12}
\end{aligned}$$

Equation (5.12) contains the full dynamics of the em-fields. For simplicity the matrices

$$\mathbf{A} = \begin{pmatrix} \mathbf{J}_{\vec{P}}(\vec{E}) & \mathbf{J}_{\vec{P}}(\vec{B}) \\ \mathbf{0}_3 & \mathbf{0}_3 \end{pmatrix} \quad (5.13)$$

$$\mathbf{B}_i = \begin{pmatrix} -\mathbf{Q}_i \mathbf{J}_{\vec{M}}(\vec{E}) & \mathbf{Q}_i (\mathbf{1} - \mathbf{J}_{\vec{M}}(\vec{B})) \\ -\mathbf{Q}_i & \mathbf{0}_3 \end{pmatrix}, \quad (5.14)$$

are introduced. With the help of (5.13) and (5.14) equation (5.12) becomes

$$(\mathbf{1} + \mathbf{A}) \partial_t \vec{u} = \sum_j \mathbf{B}_j \partial_j \vec{u}. \quad (5.15)$$

## 5.2. From PDE to ODE

Equation (5.12) can theoretically be solved using a generic PDE solver for nonlinear equations. However doing so results in an extremely costly simulation scheme [30]. In order to improve the efficiency an ODE is derived from (5.12) by exchanging the derivatives in space with finite difference approximations.

the first step required is to transform the PDE (5.12) into the form described in section 3.5. To do so both sides of equation (5.12) are multiplied by  $(\mathbf{1}_6 + \mathbf{A})^{-1}$ , resulting in

$$\partial_t \vec{u} = (\mathbf{1}_6 + \mathbf{A})^{-1} \sum_j \mathbf{B}_j \partial_j \vec{u}. \quad (5.16)$$

Recalling the discussion in 3.5 the replacement of the differential operator with a finite difference will result in either a bias in the propagation speed depending on the propagation direction or in numerical mesh drift. Since staggering the grid is not an option as it would make the numerical computation of the nonlinearities extremely difficult, a biased space has to be used.

By diagonalizing the  $\mathbf{B}_i$  and performing the derivation in their linear eigenspace the effect of the bias can be minimized. To do this the rotation matrices

$$\mathbf{R}_x = \frac{1}{\sqrt{2}} \begin{pmatrix} 0 & 0 & 0 & 0 & 0 & 1 \\ -1 & 0 & 1 & 0 & 0 & 0 \\ 0 & 1 & 0 & -1 & 0 & 0 \\ 0 & 0 & 0 & 0 & 1 & 0 \\ 0 & 1 & 0 & 1 & 0 & 0 \\ 1 & 0 & 1 & 0 & 0 & 0 \end{pmatrix}, \quad \mathbf{R}_y = \frac{1}{\sqrt{2}} \begin{pmatrix} 1 & 0 & -1 & 0 & 0 & 0 \\ 0 & 0 & 0 & 0 & 0 & 1 \\ 0 & -1 & 0 & 1 & 0 & 0 \\ 0 & 1 & 0 & 1 & 0 & 0 \\ 0 & 0 & 0 & 0 & 1 & 0 \\ 1 & 0 & 1 & 0 & 0 & 0 \end{pmatrix}$$

5. *The quantum vacuum simulation algorithm for the Heisenberg-Euler Lagrangian*

and

$$\mathbf{R}_z = \frac{1}{\sqrt{2}} \begin{pmatrix} -1 & 0 & 1 & 0 & 0 & 0 \\ 0 & 1 & 0 & -1 & 0 & 0 \\ 0 & 0 & 0 & 0 & 0 & 1 \\ 0 & 1 & 0 & 1 & 0 & 0 \\ 1 & 0 & 1 & 0 & 0 & 0 \\ 0 & 0 & 0 & 0 & 1 & 0 \end{pmatrix} \quad (5.17)$$

are defined such that

$$\begin{pmatrix} \mathbf{0}_3 & \mathbf{Q}_i \\ -\mathbf{Q}_i & \mathbf{0}_3 \end{pmatrix} = \mathbf{R}_i \text{diag}(1, 1, -1, -1, 0, 0) \mathbf{R}_i^T. \quad (5.18)$$

Making use of (5.17) the derivation of the em-vector  $\vec{u}$  can be rewritten as

$$\partial_i \vec{u} = \mathbf{R}_i \partial_i \mathbf{R}_i^T \vec{u}. \quad (5.19)$$

While this does not make any difference analytically it does so numerically. To illustrate this the 1 dimensional linear case is considered. In absence of nonlinearities in 1D (5.12) becomes without loss of generality

$$\begin{aligned} \partial_t \vec{u} &= \begin{pmatrix} \mathbf{0}_3 & \mathbf{Q}_x \\ -\mathbf{Q}_x & \mathbf{0}_3 \end{pmatrix} \partial_x \vec{u} = \begin{pmatrix} \mathbf{0}_3 & \mathbf{Q}_x \\ -\mathbf{Q}_x & \mathbf{0}_3 \end{pmatrix} \mathbf{R}_x \partial_x \mathbf{R}_x^T \vec{u} \\ &= \mathbf{R}_x \text{diag}(1, 1, -1, -1, 0, 0) \mathbf{R}_x^T \mathbf{R}_x \partial_x \mathbf{R}_x^T \vec{u} \\ &= \mathbf{R}_x \text{diag}(1, 1, -1, -1, 0, 0) \partial_x \mathbf{R}_x^T \vec{u}, \end{aligned} \quad (5.20)$$

which, when multiplied with  $\mathbf{R}_x^T$  from the left becomes

$$\partial_t \mathbf{R}_x^T \vec{u} = \text{diag}(1, 1, -1, -1, 0, 0) \partial_x \mathbf{R}_x^T \vec{u}. \quad (5.21)$$

With the help of (5.21) it is appreciated, that  $\mathbf{R}_x^T \vec{u}$  contains two components that will propagate to the right, two components that will propagate to the left and two components that will not propagate at all. This agrees with the physical necessity that there are always two modes of propagation in any given direction. Since the nonlinearities neglected in the derivation of (5.21) are extremely small, the same rotation matrices  $\mathbf{R}_i$  can be used in the full nonlinear case.

Next the derivation operator in (5.19) is substituted by finite sum weighted by stencils as described in section 3.5. This results, without loss of generality, in

$$\partial_x \vec{u}(x, y, z) \approx \mathbf{R}_x \mathcal{D}_x \mathbf{R}_x^T \vec{u}(x, y, z) = \mathbf{R}_x \sum_{\nu} \frac{1}{\Delta_x} \mathcal{S}_{\nu} \mathbf{R}_x^T \vec{u}(x + \nu \Delta_x, y, z), \quad (5.22)$$

### 5.3. Analytical properties of the numerical scheme

where the  $\mathcal{S}_\nu$  are now diagonal matrices which contain an upwind biased stencil in the backward components (the first and the second), a downwind biased stencil in forward components (the third and fourth), and an unbiased one for the last two entries in (5.22). For the two last components in (5.22) unbiased stencils can be safely used, since the value of the derivative is required for the computation of the nonlinearities only and therefore will not cause numerical mesh drifting. Note that while the rotation matrices are different for each direction, the stencil matrices for the derivatives do not, since for all directions the eigenvalues are sorted in the same fashion (as seen in (5.18)).

In the lowest possible order of accuracy (see Table 3.1) the stencil matrices are

$$\begin{aligned}\mathcal{S}_{-1} &= \text{diag}(-1, -1, 0, 0, -1/2, -1/2), & \mathcal{S}_0 &= \text{diag}(1, 1, -1, -1, 0, 0) \\ \mathcal{S}_1 &= \text{diag}(0, 0, 1, 1, 1/2, 1/2), & \mathcal{S}_\nu &= 0 \quad \forall \nu : |\nu| > 1\end{aligned}$$

Inserting (5.22) into (5.16) results in the following system of ODEs

$$\partial_t \vec{u} = (\mathbf{1}_6 + \mathbf{A})^{-1} \sum_{j \in \{x, y, z\}} \mathbf{B}_j \mathbf{R}_j \sum_{\nu} \frac{1}{\Delta_j} \mathcal{S}_\nu \mathbf{R}_j^T \vec{u}_{j+\nu}. \quad (5.23)$$

These ODEs can be evolved efficiently in time by using optimized ODE solvers. In this thesis the Adams-Moulton solver from the CVODE library was used. The CVODE library is part of the *Sundials* distribution [35].

## 5.3. Analytical properties of the numerical scheme

### Plane wave case

In order to derive the analytical properties of the scheme the plane wave case is considered implying

$$\vec{E}(\vec{x}, t) = \vec{E}_0 e^{-i(\omega t - \vec{k} \cdot \vec{r})}, \quad \vec{B}(\vec{x}, t) = \hat{k} \times \vec{E}(\vec{x}, t), \quad (5.24)$$

where  $\hat{k}$  is the normalized  $\vec{k}$  vector and  $\vec{E}_0$  the amplitude and polarization vector. For a single such wave the nonlinearities disappear since

$$\vec{B}^2 = \vec{E}^2, \quad \vec{E} \cdot \vec{B} = 0. \quad (5.25)$$

Thus  $\mathcal{F} = \mathcal{G} = 0$  and therefore  $\mathcal{L}_{\text{HE}}$  vanishes. Then (5.23) takes the form

$$\partial_t \vec{u} = \sum_{j \in \{x, y, z\}} \begin{pmatrix} \mathbf{0}_3 & \mathbf{Q}_j \\ -\mathbf{Q}_j & \mathbf{0}_3 \end{pmatrix} \mathbf{R}_j \sum_{\nu} \frac{1}{\Delta_j} \mathcal{S}_\nu \mathbf{R}_j^T \vec{u}_{j+\nu}. \quad (5.26)$$

### Error and load scaling for plane waves

Using an implicit ODE solver such as the ones provided by the *Sundials CVODE* library, results in fully controllable integration errors in time. Unlike the situation for time integration, the error in the space derivatives is carried over from the stencils derived in section 3.5 and is incremented by one to two orders of magnitude due to error propagation.

Before the predicted error scaling is verified, the stiffness of the problem is considered. Since for the eigenvalues  $\lambda_k$  of the ODEs system

$$\lim_{\Delta_j \rightarrow 0} \lambda_k = 1 \quad (5.27)$$

holds, ODEs will become stiffer with increasing numerical accuracy. This can be seen in figure 5.1. It shows that for big relative resolutions (8-500 points per wavelength) the Adams-Moulton method [36] beats backwards differentiation BDF [37]. However, past the 500 points per wavelength mark the ODEs become so stiff, that backwards differentiation is better suited.

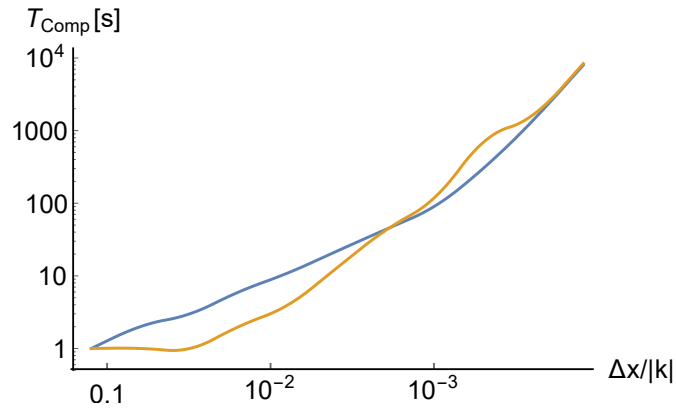


**Figure 5.1.:**  $\Delta x/|\vec{k}|$  vs. computation time for the 1D propagation of 10 periods of a cosine wave. The lines correspond to using the Adams-Moulton method (orange) and Backwards differentiation (blue).

With this in mind the answer to the question, which solver to use, becomes evident when observing the error evolution, see figure 5.2.

Comparison of Figs. 5.1 and 5.2 shows, that the Adams-Moulton solver is superior to the BDF solver when using the ISOC++14 long double precision, since it is faster for practical numerical resolutions (see 5.1). Thus, the default ODE solver for the QVS algorithm is Adams-Moulton.

With the question of what solver to use answered the different stencil orders can be compared against each other. Figure 5.3 shows that, as expected, the error of the simulation scales like the error of the derivatives caused by the finite differences.

### 5.3. Analytical properties of the numerical scheme

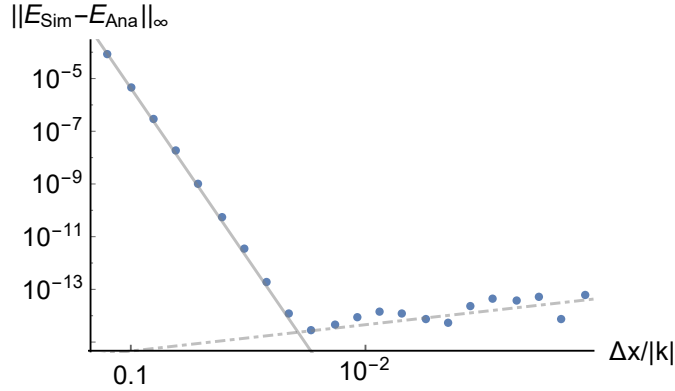


**Figure 5.2.:** Highest absolute deviation of the simulation results from the analytic calculations vs relative resolution. Note that the time integration error is held below  $10^{-17}$ . The grey continuous line represents a fitted  $x^{-13}$  function for the expected error scaling from the finite difference approximation in space. The grey dashdotted line is a fitted  $x$  function for the expected round off error. The data was obtained using ISOC++14 long double precision for the lattice values.

It is worth noting that the error increment with respect to the error order of the finite differences (see 3.5) is to be expected due to error propagation.

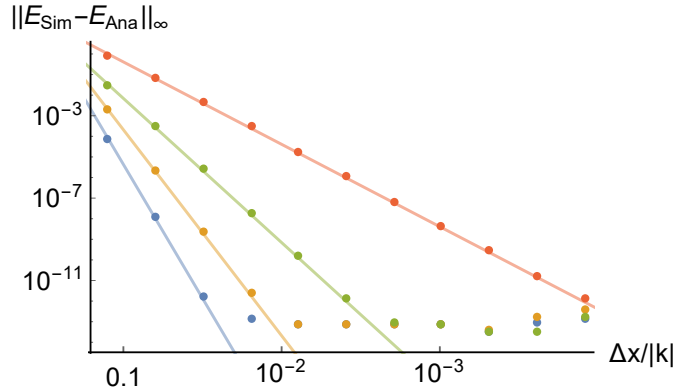


**Figure 5.3.:** Highest absolute deviation of the simulation results from the analytic expectancy vs relative resolution for different stencils [ s13(blue)/ s10(orange)/ s7(green)/ s4(red)] and backwards differentiation. Note that the time integration error is held below  $10^{-15}$ . The continuous line represents a fitted  $x^{-13}/x^{-10}/x^{-7}/x^{-4}$  function for the expected error scaling from the finite difference approximation in space. The data was obtained using ISOC++14 long double precision for the lattice values.

At the same time the investigation of the computing time for a given numerical error threshold for the temporal integration is almost independent of the stencil as figure 5.4 illustrates. This is what is expected since speed of convergence in the underlying adaptive time integration scheme scales inversely with stencil accuracy.

## 5. The quantum vacuum simulation algorithm for the Heisenberg-Euler Lagrangian

However, convergence to a given error threshold during temporal integration does not imply convergence to the correct physical solution. As figure 5.3 shows high orders of the stencil are required to converge to the correct physical solution.

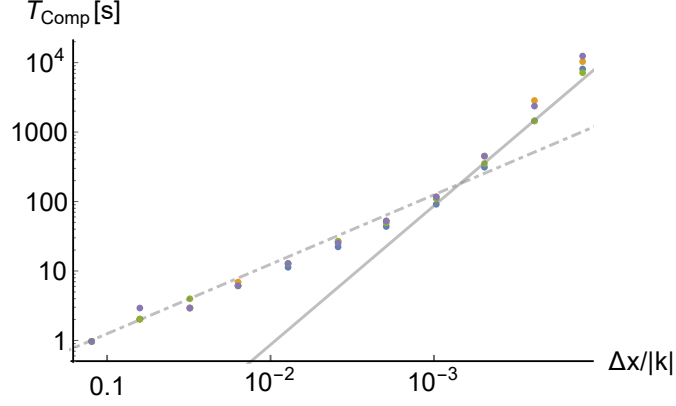


**Figure 5.4.:** Computation time vs. number of points for discretizations of the same physical space using stencil of order 13(blue) / 10(orange) / 7(green) / 4(red). Note that the initial linear slope (dashed line) is due to the fact that the stiffness is not yet present and thus the time-step is severely underestimated. At smaller relative differences the stiffness comes into play and the computation time scales quadratic as expected.

### Dispersion relation

Inserting (5.24) into (5.26) and assuming that the derivative in time is performed exactly by the CVODE solver yields

$$-i\omega \vec{E}_0 e^{-i(\omega t - \vec{k} \cdot \vec{r})} = \sum_{j \in \{x, y, z\}} \begin{pmatrix} \mathbf{0}_3 & \mathbf{Q}_j \\ -\mathbf{Q}_j & \mathbf{0}_3 \end{pmatrix} \mathbf{R}_j \sum_{\nu} \frac{1}{\Delta_j} \mathcal{S}_{\nu} \mathbf{R}_j^{\top} \vec{E}_0 e^{-i(\omega t - \vec{k} \cdot (\vec{r} + \nu \vec{e}_j))}. \quad (5.28)$$

The assumption that the time derivative is exact is valid since the ODE solver uses an implicit algorithm and checks convergence to the order of the working precision, as consequence any errors that may arise from the latter are not be observable in the simulation. Simplifying (5.28) ends in

$$0 = \left[ i\omega \mathbf{1}_6 + \sum_{j \in \{x, y, z\}} \begin{pmatrix} \mathbf{0}_3 & \mathbf{Q}_j \\ -\mathbf{Q}_j & \mathbf{0}_3 \end{pmatrix} \mathbf{R}_j \sum_{\nu} \frac{1}{\Delta_j} \mathcal{S}_{\nu} \mathbf{R}_j^{\top} e^{i\nu k_j} \right] \vec{E}_0, \quad (5.29)$$

which can only be satisfied in the nontrivial case, i.e.,  $\vec{E}_0 \neq 0$  if and only if

$$0 = \det \left( i\omega \mathbf{1}_6 + \sum_{j \in \{x, y, z\}} \begin{pmatrix} \mathbf{0}_3 & \mathbf{Q}_j \\ -\mathbf{Q}_j & \mathbf{0}_3 \end{pmatrix} \mathbf{R}_j \sum_{\nu} \frac{1}{\Delta_j} \mathcal{S}_{\nu} \mathbf{R}_j^{\top} e^{i\nu k_j} \right). \quad (5.30)$$

### 5.3. Analytical properties of the numerical scheme

Solving (5.30) for  $\omega$  as shown in B for  $\vec{k} = k_j \vec{e}_j$  results in

$$\omega = \sum_{\nu} s_{\nu}^f \sin(\nu k_j \Delta_j) - i \sum_{\nu} s_{\nu}^f \cos(\nu k_j \Delta_j). \quad (5.31)$$

A plot of  $\omega$  as a function of  $\vec{k}$  for  $\vec{k}$ -vectors of the form  $\vec{k} = (k_x \ 0 \ 0)$  is shown in figure 5.5. In the figure it can be seen that the more points are taken into account by the stencil, the longer the dispersion relation stays similar to the classical vacuum dispersion. Furthermore, all the stencils result in a symmetric dispersion relation, which means that all of them will propagate with the same phase velocity for both directions. Finally it can be observed that due to the occurrence of an imaginary part in  $\omega$  unphysical modes of the wave are absorbed. However, the higher the order of the stencil the later (in terms of  $k_x \Delta_x$ ) mode absorption appears and the weaker it is.

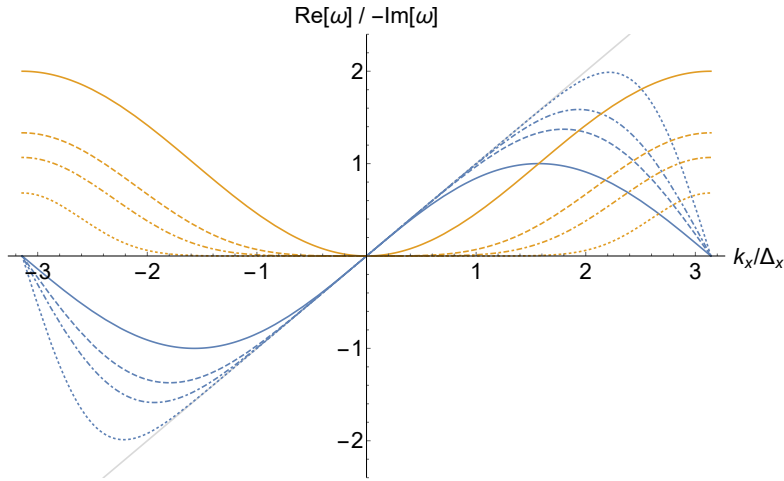


**Figure 5.5.:** Plot of the real (blue) and imaginary (orange) parts of omega for different stencils  $[s^{[-1,0]}$  (solid),  $s^{[-2,1]}$  (dashed),  $s^{[-3,2]}$  (dot-dashed),  $s^{[-7,6]}$  (dotted)]. The gray line in the left plot represents the dispersion relation in the classical vacuum.

A similar plot can be found in figure 5.6 where instead of the total number of points used by the stencil the bias has been modified.

Here it can be seen that a stronger bias causes the absorption to become stronger and the phase velocity becomes faster, even superluminal. Note though that the points of inflection for the in 5.6 for the real and imaginary parts of  $\omega$  is the same independently of the bias chosen.

#### Dispersion relation in higher dimensions

The same analysis can be performed in more than one dimension. While there is no longer a closed expression for  $\omega$ , a computer algebra system can still solve (5.30)

## 5. The quantum vacuum simulation algorithm for the Heisenberg-Euler Lagrangian

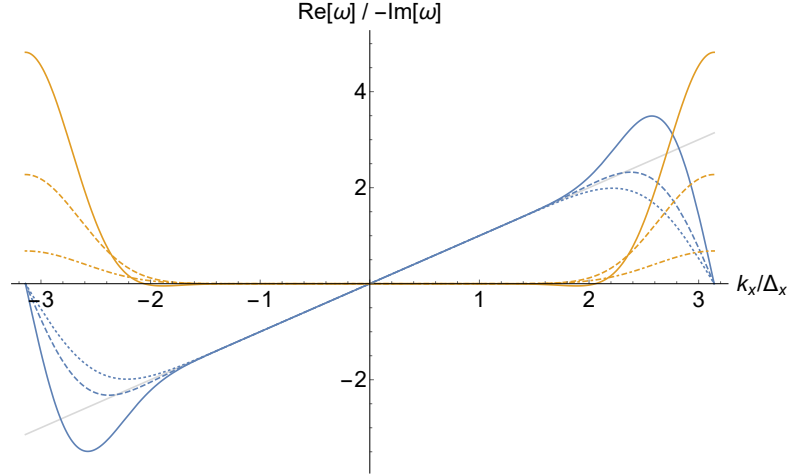


**Figure 5.6.:** Plot of the real (blue) and imaginary (orange) parts of omega for different stencils [ $\vec{s}^{[-9,4]}$  (solid),  $\vec{s}^{[-8,5]}$  (dashed),  $\vec{s}^{[-7,6]}$  (dot-dashed)]. The gray line in the left plot represents the dispersion relation in the classical vacuum.

numerically. The results can be seen in Figure 5.7. As before, mode absorption is limited to unphysical modes well past the Nyquist limit. The error in the real part of  $\omega$  however depends on the propagation direction of the modes as for all the Cartesian methods that decompose space along the  $x, y, z$ -axes. This error is independent of the choice of bias and to a large degree of the choice of size of the stencil.

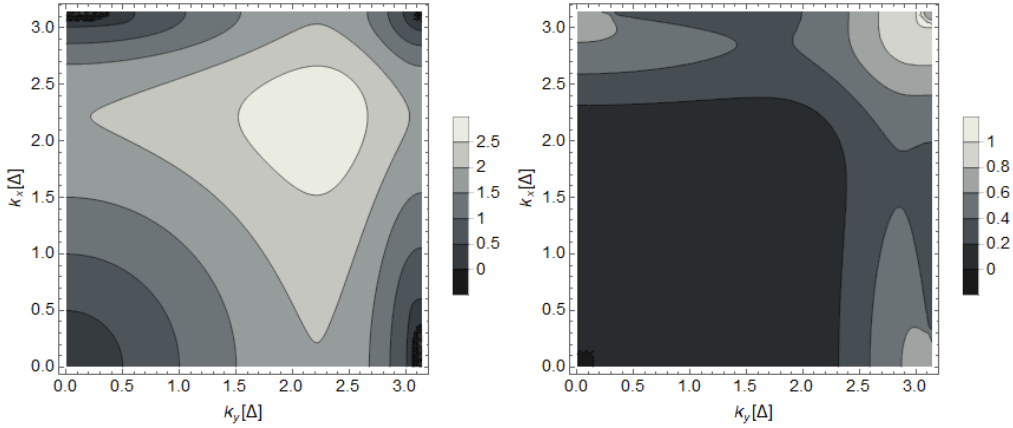


**Figure 5.7.:** Contour plot of the real (left) and imaginary (right) parts of  $\omega_{Sim}[\Delta]$  for  $\vec{k} = (k_x, k_y, 0)$ .  $\vec{s}^{[-7,6]}$  where used. Note that the results are independent of the choice of delta. The dispersion relation  $\omega_{Sim}$  is computed using the formula in appendix B.

Note, however, that even though a direction dependent error is still there, it is better than the corresponding error in the Yee scheme. Figure 5.8, shows how the

## 5.4. Remarks on the implementation

dispersion relation error is several orders of magnitude below the one of the Yee scheme [33].

The way to remedy this problem would be to use a different set of points and basis functions which combine a nonlinear combination of  $x$  and  $y$ , for example  $\sqrt{x^2 + y^2}$ , as an extra basis coordinate. This is, however, beyond the scope of this thesis.

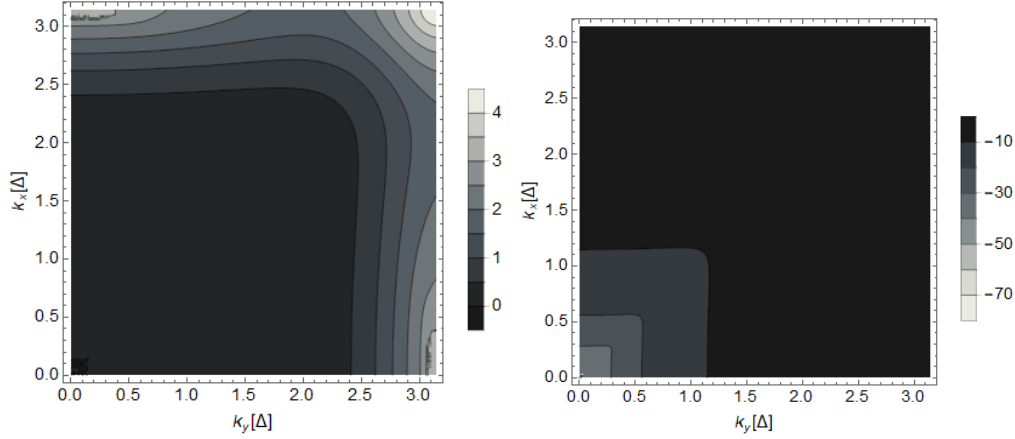


**Figure 5.8.:** Contour plot of the real (left) part of  $\omega_{Sim} - \omega_{Ana}[\Delta]$  for  $\vec{k} = (k_x, k_y, 0)$ . The plot to the left is in normal scale and the one on the right is in logarithmic scale.  $\vec{s}^{[-7,6]}$  where used. Note that the results are independent of the choice of delta. The dispersion relation  $\omega_{Sim}$  is computed using the formula in appendix B and  $\omega_{Ana}$  corresponds to the classical vacuum dispersion relation.

## 5.4. Remarks on the implementation

### Inversion of the matrix

The most expensive operation in the computation of the right hand side of (5.23) is the inversion of the  $6 \times 6$  matrix  $(\mathbf{1}_6 + \mathbf{A})^{-1}$  [38]. In order to avoid having to invert the whole matrix the block-form properties of the matrix are used to simplify the inversion

$$(\mathbf{1}_6 + \mathbf{A})^{-1} = \begin{pmatrix} \underbrace{\mathbf{1}_3 + \mathbf{J}_{\vec{P}}(\vec{E})}_{\mathbf{C}} & \mathbf{J}_{\vec{P}}(\vec{B}) \\ \mathbf{0}_3 & \mathbf{1}_3 \end{pmatrix}^{-1} = \begin{pmatrix} \mathbf{C}^{-1} & -\mathbf{C}^{-1}\mathbf{J}_{\vec{P}}(\vec{B}) \\ \mathbf{0}_3 & \mathbf{1}_3 \end{pmatrix}, \quad (5.32)$$

## 5. The quantum vacuum simulation algorithm for the Heisenberg-Euler Lagrangian

which reduces the dimension of the matrix to be inverted to 3. This inversion is then performed using the explicit inverse

$$\begin{pmatrix} a & b & c \\ d & e & f \\ g & h & k \end{pmatrix}^{-1} = \frac{1}{\det} \begin{pmatrix} ek - fh & ch - bk & bf - ce \\ fg - dk & ak - cg & cd - af \\ dh - eg & bg - ah & ae - bd \end{pmatrix}. \quad (5.33)$$

Furthermore, in order to avoid performing the multiplication with  $\mathbf{C}^{-1}$  twice, the computation of  $(\mathbf{1}_6 + \mathbf{A})^{-1}\vec{v}$  is performed using the scheme

$$(\mathbf{1}_6 + \mathbf{A})^{-1} \begin{pmatrix} v_1 \\ v_2 \\ v_3 \\ v_4 \\ v_5 \\ v_6 \end{pmatrix} = \begin{pmatrix} \mathbf{C}^{-1} \left( \begin{pmatrix} v_1 \\ v_2 \\ v_3 \end{pmatrix} - \mathbf{J}_{\vec{P}}(\vec{B}) \begin{pmatrix} v_4 \\ v_5 \\ v_6 \end{pmatrix} \right) \\ \begin{pmatrix} v_4 \\ v_5 \\ v_6 \end{pmatrix} \end{pmatrix}. \quad (5.34)$$

Another approach would be to use the geometric expansion

$$(\mathbf{1}_6 + \mathbf{A})^{-1} = \mathbf{1}_6 - \mathbf{A} + \mathbf{A}^2 - \dots, \quad (5.35)$$

and truncate the expansion after the first order in  $\mathbf{A}$ , arguing that the corrections from higher order terms are negligible due to the smallness of the nonlinearities. However, even though this method has been successfully tested in benchmarks it has two main issues that have to be considered. Firstly, equation (5.35) will lose validity when the nonlinearities become big, which in turn unnecessarily imposes another constraint on the simulation settings. Secondly, the ability to ascertain errors is lost as technically the contributions by the 6 photon scattering diagram would be of the same order as the corrections to the 4 photon diagram contribution of the  $\mathbf{A}^2$  term. Thus, while theoretically faster, this method will not be used.

### Translocation for faster derivation

As noted in chapter 4 computers have multiple levels of storage for operation. When computing the finite difference expression of the derivative in time it is important to keep the access operations to data stored outside of the cache to a minimum. The reason why this becomes of utmost importance is, that while 2 points in the 3D lattice can be quite close to one another in the physical space they might be quite distant from one another in the memory space. This is due to the fact that a computer uses a long one dimensional array to store the data. Thus a 3D lattice is projected onto a 1D array using a so called space filling curve (see figure 5.9). The problem with this is that no matter how the curve is chosen

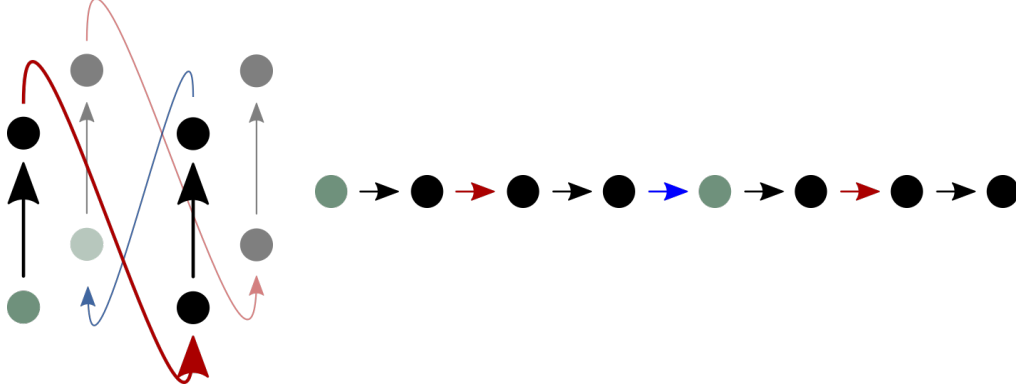


**Figure 5.9.:** Representations of the same space filling curve for a  $2 \times 2 \times 2$  lattice in physical (left) and memory space (right). Note that the two green points are neighbors in the physical space but they are 3 spaces apart in the memory space. A cache of size 4 would not be able to store both green points at the same time.

the average distances in memory-space will always be at least  $1, N, N \cdot M$ , where  $M$  and  $N$  are, e.g., the length and width of the lattice. For a cache with size  $< N$  this leads to cache misses.

As a consequence, when the code requires next neighbor data for the computation of the finite difference the data might not be in the cache in for two out of three directions. When using a order 13 stencil for the derivative as in the QVS algorithm, the program will then realize 13 slow calls to the RAM per point. In order to circumvent this problem the data needs to be rearranged such that the direction in which the differentiation is being computed is the direction in which the distance in storage between next neighbors is 1. Thereby, the 13 slow calls per point are reduced to 1 single call per point. In order to avoid copying the same data twice the translocation of the data in memory space is performed at the same time as the rotation in (5.22).

Tests with  $10 \times 10 \times 10^5$  lattices show that the total computation time when using the translocation of the data points outlined above is up to 2 times faster when using 13th order stencils, see figure 5.10.

### Optimization of the computation of the nonlinear matrices

The brute force computation of  $\mathbf{J}_{\vec{M}}(\vec{E})$  consists of 125 additions/subtractions and 284 multiplications/divisions, if 4 and 6 photon scattering diagrams are being considered. However, the functional may be rewritten using the usual derivation rules as follows:

$$\mathbf{J}_{\vec{M}}(\vec{E}) = \frac{\partial \vec{M}}{\partial \vec{E}} = \frac{\partial}{\partial \vec{E}} \frac{\partial \mathcal{L}_{HE}}{\partial \vec{B}} = \frac{\partial}{\partial \vec{E}} \frac{\partial \mathcal{L}_{HE}}{\partial (\mathcal{F}, \mathcal{G})} \cdot \frac{\partial (\mathcal{F}, \mathcal{G})}{\partial \vec{B}}$$

## 5. The quantum vacuum simulation algorithm for the Heisenberg-Euler Lagrangian

```
Arnau@platans2 /.../Rotated Derivation Test
$ c++ -O2 3DRotateDerivationWithTranslocation.cpp -pg

Arnau@platans2 .../Rotated Derivation Test
$ ./a.exe
1e-05 2.10552e-10
...

Arnau@platans2 .../Rotated Derivation Test
$ gprof ./a.exe gmon.out -p -b
Flat profile:

Each sample counts as 0.01 seconds.
 %   cumulative   self           self         total
time  seconds    seconds   calls   ms/call  ms/call  name
44.21    9.04      9.04         20    452.00   452.00  leiteFeldAb(...)
43.81   18.00     8.96         40    224.00   224.00  rotiereZuEigenrichtung(...)
...

Arnau@platans2 .../Rotated Derivation Test
$ c++ -O2 3DRotateDerivationWithoutTranslocation.cpp -pg

Arnau@platans2 .../Rotated Derivation Test
$ ./a.exe
1e-05 2.10552e-10
...

Arnau@platans2 .../Rotated Derivation Test
$ gprof ./a.exe gmon.out -p -b
Flat profile:

Each sample counts as 0.01 seconds.
 %   cumulative   self           self         total
time  seconds    seconds   calls   s/call   s/call  name
83.39   36.20     36.20         20     1.81     1.81  leiteFeldAb(...)
10.73   40.86     4.66         40     0.12     0.12  rotiereZuEigenrichtung(...)
...
```

**Figure 5.10.:** Copy of the console output for the benchmarking of rotated derivative computation improvement. Here it can be seen how the computational time per call improves from 2050 ms per call to 900 ms per call when using the trans-location. Note that it has been shortened at some points in order to improve visibility.

#### 5.4. Remarks on the implementation

$$\begin{aligned}
&= \frac{\partial^2 \mathcal{L}_{HE}}{\partial^2(\mathcal{F}, \mathcal{G})} \cdot \frac{\partial(\mathcal{F})}{\partial \vec{E}} \cdot \frac{\partial(\mathcal{G})}{\partial B} + \frac{\partial \mathcal{L}_{HE}}{\partial(\mathcal{F}, \mathcal{G})} \frac{\partial}{\partial \vec{E}} \frac{\partial(\mathcal{F})}{\partial \vec{B}} \\
&= \frac{\partial^2 \mathcal{L}_{HE}}{\partial^2(\mathcal{F}, \mathcal{G})} \cdot \begin{pmatrix} \vec{E} \\ \vec{B} \end{pmatrix} \cdot \begin{pmatrix} -\vec{B} \\ \vec{E} \end{pmatrix} + \frac{\partial \mathcal{L}_{HE}}{\partial(\mathcal{F}, \mathcal{G})} \frac{\partial}{\partial \vec{E}} \begin{pmatrix} -\vec{B} \\ \vec{E} \end{pmatrix} \\
&= (\vec{E}, \vec{B}) \begin{pmatrix} \partial_{\mathcal{F}\mathcal{F}}^2 \mathcal{L}_{HE} & \partial_{\mathcal{F}\mathcal{G}}^2 \mathcal{L}_{HE} \\ \partial_{\mathcal{F}\mathcal{G}}^2 \mathcal{L}_{HE} & \partial_{\mathcal{G}\mathcal{G}}^2 \mathcal{L}_{HE} \end{pmatrix} \begin{pmatrix} -\vec{B} \\ \vec{E} \end{pmatrix} + \mathbf{1}_3 \partial_{\mathcal{G}} \mathcal{L}_{HE}. \quad (5.36)
\end{aligned}$$

With the help of 5.36 and implementing the computation of the derivatives of the HE-Lagrangian wrt.  $\mathcal{F}$  and  $\mathcal{G}$  instead of  $\vec{E}$  and  $\vec{B}$  the computation of  $\mathbf{J}_{\vec{M}}(\vec{E})$  now requires only to 37 additions/subtractions and 66 multiplications/divisions.

The computational load improves even further when the steps in (5.36) are applied to all the required Jacobi matrices as  $\mathcal{F}, \mathcal{G}$  and the derivatives of  $\mathcal{L}_{HE}$  only need to be computed once. An analogous computation to the one above yields the required formulas

$$\mathbf{J}_{\vec{P}}(\vec{E}) = (\vec{E}, \vec{B}) \begin{pmatrix} \partial_{\mathcal{F}\mathcal{F}}^2 \mathcal{L}_{HE} & \partial_{\mathcal{F}\mathcal{G}}^2 \mathcal{L}_{HE} \\ \partial_{\mathcal{F}\mathcal{G}}^2 \mathcal{L}_{HE} & \partial_{\mathcal{G}\mathcal{G}}^2 \mathcal{L}_{HE} \end{pmatrix} \begin{pmatrix} \vec{E} \\ \vec{B} \end{pmatrix} + \mathbf{1}_3 \partial_{\mathcal{F}} \mathcal{L}_{HE}, \quad (5.37)$$

$$\mathbf{J}_{\vec{P}}(\vec{B}) = (-\vec{B}, \vec{E}) \begin{pmatrix} \partial_{\mathcal{F}\mathcal{F}}^2 \mathcal{L}_{HE} & \partial_{\mathcal{F}\mathcal{G}}^2 \mathcal{L}_{HE} \\ \partial_{\mathcal{F}\mathcal{G}}^2 \mathcal{L}_{HE} & \partial_{\mathcal{G}\mathcal{G}}^2 \mathcal{L}_{HE} \end{pmatrix} \begin{pmatrix} \vec{E} \\ \vec{B} \end{pmatrix} + \mathbf{1}_3 \partial_{\mathcal{G}} \mathcal{L}_{HE}, \quad (5.38)$$

$$\mathbf{J}_{\vec{M}}(\vec{B}) = (-\vec{B}, \vec{E}) \begin{pmatrix} \partial_{\mathcal{F}\mathcal{F}}^2 \mathcal{L}_{HE} & \partial_{\mathcal{F}\mathcal{G}}^2 \mathcal{L}_{HE} \\ \partial_{\mathcal{F}\mathcal{G}}^2 \mathcal{L}_{HE} & \partial_{\mathcal{G}\mathcal{G}}^2 \mathcal{L}_{HE} \end{pmatrix} \begin{pmatrix} -\vec{B} \\ \vec{E} \end{pmatrix} - \mathbf{1}_3 \partial_{\mathcal{F}} \mathcal{L}_{HE}. \quad (5.39)$$

Furthermore the matrix

$$\begin{pmatrix} \mathbf{J}_{\vec{P}}(\vec{E}) & \mathbf{J}_{\vec{P}}(\vec{B}) \\ \mathbf{J}_{\vec{M}}(\vec{E}) & \mathbf{J}_{\vec{M}}(\vec{B}) \end{pmatrix} \quad (5.40)$$

is symmetric and thus the upper right half of it does not have to be computed.

Using all optimizations discussed the operation count for computing (5.40) is now (90, 156) vs. the original count of (699, 1488). The improvements by this scheme are illustrated by computing the expression  $(\mathbf{Q} + \mathbf{B})\mathbf{D}_i$  for a  $10^4 \times 10 \times 10$  lattice 20 times by the brute force versus by method (5.36). This results in a reduction of computing time of 61% (see figure 5.11).

It may also be noted that the terms are not only analytically equal but also numerically.

## 5. The quantum vacuum simulation algorithm for the Heisenberg-Euler Lagrangian

```
Arnaud@platans2 /.../Nonlinear Calculations Improvement Test
$ c++ -O2 NonlinearityCalculationTests.cpp -pg

Arnaud@platans2 /.../Nonlinear Calculations Improvement Test
$ ./a.exe
0.0001,0
...

Arnaud@platans2 /.../Nonlinear Calculations Improvement Test
$ gprof ./a.exe gmon.out
Flat profile:

Each sample counts as 0.01 seconds.
%   cumulative   self           self         total
time  seconds    seconds   calls  ms/call  ms/call  name
66.92    3.58      3.58         20    179.00   179.00  BruteForceNonlinearity(...)
25.79    4.96      1.38         20     69.00    69.00  VarianteMit2(...)
...
```

**Figure 5.11.:** Copy of the console output for the benchmarking of nonlinear computation improvement. Here it can be seen how the computational time per call improves from 179 ms per call to 69 ms per call when using memorization to reduce the computational load for the determination of the nonlinearities. Note that it has been shortened at some points in order to improve visibility.

## 6. Benchmarks

The implementation of the QVS algorithm as presented in chapter 5 is used to simulated some of the already proposed scenarios for the measurement of vacuum nonlinearities [8, 10, 13], and the simulation results are compared to the analytic predictions done in said publications.

### 6.1. The constant background case

The simplest thing to verify is the change of the refractive index through an external electric field. To this end, a plane wave  $\vec{E}(x, t)$  traveling in  $x$ -direction through the quantum vacuum is considered, where  $E_x = E_y = 0$ . Its time evolution can be written as

$$E_z(x, t) = E \cos(\lambda^{-1}x - t v_{ph} 2\pi \lambda^{-1}), \quad (6.1)$$

where  $E$  is the amplitude of the electric field  $\vec{E}$ . The phase speed can be decomposed into the classical vacuum speed plus the nonlinear contribution given in (2.183) as

$$v_{ph} = v_{vac} + v_{nli} = 1 - \frac{\frac{\alpha}{45\pi}(11 \pm 3) \frac{E^2}{E_{cr}^2}}{1 + \frac{\alpha}{45\pi}(11 \pm 3) \frac{E^2}{E_{cr}^2}}. \quad (6.2)$$

If the time of measurement  $t_m$  is chosen such that  $t_m = m \lambda$  for  $m \in \mathbb{N}$ , (6.1) can be rewritten as

$$E_z(x, t_m) = A \cos(\lambda^{-1}x - 2\pi m v_{nli}), \quad (6.3)$$

which after Fourier transformation in space yields

$$\text{FT}[E_z(x, t_m)](k) = A \sqrt{\frac{\pi}{2}} \left( e^{-i2\pi m v_{nli}} \delta(k - \lambda^{-1}) + e^{i2\pi m v_{nli}} \delta(k + \lambda^{-1}) \right). \quad (6.4)$$

The evaluation at  $k = \lambda^{-1}$  gives

$$\text{FT}[E_z(x, t_m)](\lambda^{-1}) = A \sqrt{\frac{\pi}{2}} e^{-i2\pi m v_{nli}}. \quad (6.5)$$

Equation (6.5) can be solved for  $v_{nli}$  by making use of de Moivre's formula resulting in

$$v_{nli} = -\frac{1}{2\pi m} \arg \left( \text{FT}[E_z(x, t_m)](\lambda^{-1}) \right). \quad (6.6)$$

## 6. Benchmarks

The right hand side of equation (6.6) can be computed using the field values provided by the time evolution of the initial field  $E_z(x, 0)$  by just replacing the Fourier transformation with a discrete fast Fourier transform (FFT).

Simulation 1710120003		
Description:	Initial settings for the analysis of phase velocity variation in vacuum, by propagating a plane em-wave in a strong electric background	
Sim. Box	Size	100 $\mu\text{m}$
	# of points	1000
Plane wave	$\vec{E}_0$	$(0, 0, 1)\mu E_{cr}$
	$\vec{k}$	$(0.5, 0, 0) 1/\mu\text{m}$
Background	$\vec{E}_0$	$(0, 0, 1)\mu E_{cr} - (0, 0, 1)E_{cr}$
	$\vec{k}$	$(-1, 0, 0) 1/\text{Pm}$
Note:	Simulation 1710120019 is the same but the polarization of the background has been rotated by $\pi/2$	

**Table 6.1.:** Initial settings for the analysis of phase velocity variation in vacuum nonlinearities.

To verify that the QVS algorithm reproduces the  $v_{nli}$  in (6.2) a plane wave with  $\lambda = 2\mu\text{m}$  is propagated through a counter-propagating em-background of different field strengths for  $t = 200\mu\text{m}$  (see table 6.1). The results of these simulations can be seen in figure 6.1. The expected velocities  $v_{nli}$  (6.2) and the ones extracted via (6.6) are in agreement for  $E > 10^{-4}E_{cr}$ . For  $E < 10^{-4}E_{cr}$  the analytic prediction and the simulation results diverge. Further analysis however shows that this is due to the changes in the field data caused by the phase velocity difference to fall below the numerical accuracy of  $10^{-20}$ .

## 6.2. Vacuum birefringence

Recalling (2.192)

$$P_{\text{flip}} = \frac{\alpha^2}{225} \frac{1}{\lambda^2} \sin^2(2\sigma) \left( \int dx \frac{A(x)^2}{E_{cr}^2} \right)^2, \quad (6.7)$$

it can be seen that only a few parameters are relevant for the magnitude of the polarization flip probability. Most remarkably  $P_{\text{flip}}$  is independent of the shape of the interacting pulses. Equation (6.7) may thus be used to benchmark the QVS algorithm in multiple ways. First, the dependencies on the parameters  $\lambda$ ,  $\sigma$  and the integral over the strong pulse amplitude squared can be verified. Second, the independence of  $P_{\text{flip}}$  from the pulse shape can be checked. Third, the scaling properties can be used to verify published analytical expectations [8].

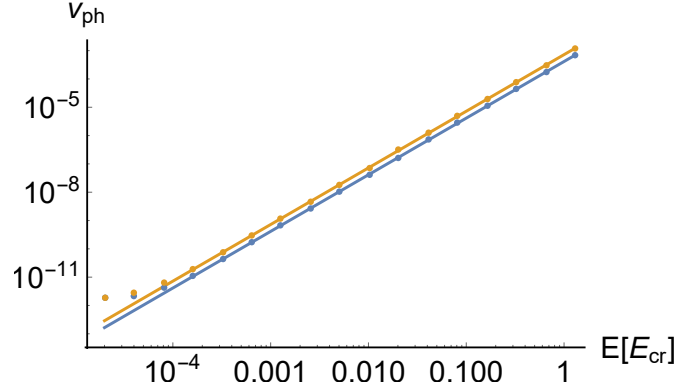


**Figure 6.1.:** Plot of the nonlinear phase velocity versus background field strength. The dots correspond to the values of  $v_{nli}$  retrieved from the simulations with the QVS algorithm using (6.6). The solid lines correspond to the values computed using (6.2). The two cases represented in the plot are parallel background and probe polarization ( $\sigma = 0$ , blue) and orthogonal polarization ( $\sigma = \pi/2$ , orange).

### Verification of published data

In order to benchmark the vacuum birefringence data against already peer reviewed results, the experiment of two counter-propagating pulses as presented in [8] is studied (see figure 6.4 top). To be more precise the ration of number of photons with perpendicular polarization to the total amount of photons  $N_{\perp}/N$  (see (2.191)) is considered for a probe pulse with tiny radius (case (a) in the aforementioned paper) and a duration of  $T = 30$ fs. The corresponding initial settings are given in table 6.2.

Note that the choice of amplitude for the probe is irrelevant as long as  $E_p \ll E_{cr}$ . Furthermore, due to the large difference between pulse duration and wavelength a large discretization is required in order for the pulse frequency to remain below the Nyquist frequency. In order to avoid this the simulations are performed using lower frequencies and the result is then extrapolated. Furthermore, since there is no diffusion in 1D and the intent is to model the 3D situation that has diffusion the peak field strength needs to be reduced to the average over the interaction time ( $t_i = 23.3$  fs see figure 6.3).

As em fields are simulated instead of single photons the only data accessible are the field values at any given time. To compare these results to the ones in [8] the energies in each polarization need to be computed as

$$\mathcal{E}_{\perp} = \sum_{x_i \in \text{Lattice}} \left( \vec{E}(x_i) \cdot \vec{\epsilon}_{\perp} \right)^2, \quad \mathcal{E}_{\parallel} = \sum_{x_i \in \text{Lattice}} \left( \vec{E}(x_i) \cdot \vec{\epsilon}_{\parallel} \right)^2, \\ \mathcal{E}_{tot} = \mathcal{E}_{\perp} + \mathcal{E}_{\parallel}. \quad (6.8)$$

## 6. Benchmarks

Simulation 1602081731		
Description:	Initial settings for the analysis of vacuum birefringence by coliding two em-pulses, as presented in [8].	
Sim. Box	Size	80 $\mu\text{m}$
	# of points	1000
Pump Pulse	$\vec{E}_0$	(0, 0, 0.34) $\text{m}E_{cr}$
	$\vec{k}$	(-1.25, 0, 0) $1/\mu\text{m}$
	$\vec{x}_0$	(22, 0, 0) $\mu\text{m}$
	$\Phi$	14.1 $\mu\text{m}$
Probe Pulse	$\vec{E}_0$	(0, 50, 50) $\mu E_{cr}$
	$\vec{k}$	(10.4, 0, 0) $1/\text{nm}$
	$\vec{x}_0$	(58, 0, 0) $\mu\text{m}$
	$\Phi$	10 $\mu\text{m}$

**Table 6.2.:** Initial settings for the analysis of vacuum birefringence as presented in [8].

Then, it can easily be checked, that

$$\frac{N_{\perp}}{N} = \frac{\hbar\omega N_{\perp}}{\hbar\omega N} = \frac{\mathcal{E}_{\perp}}{\mathcal{E}_{tot}}. \quad (6.9)$$

Note, that the constants neglected in the computation of the energy in (6.8) cancel out.

The simulation now allows to time resolve the flipping process (see figure 6.3 left) unlike in the reference paper [8]. Repeating the simulation for different pulse frequencies makes it possible to extrapolate the polarization flip values for  $\lambda_p = 96$  pm (see figure 6.3 right) as used in the reference [8].

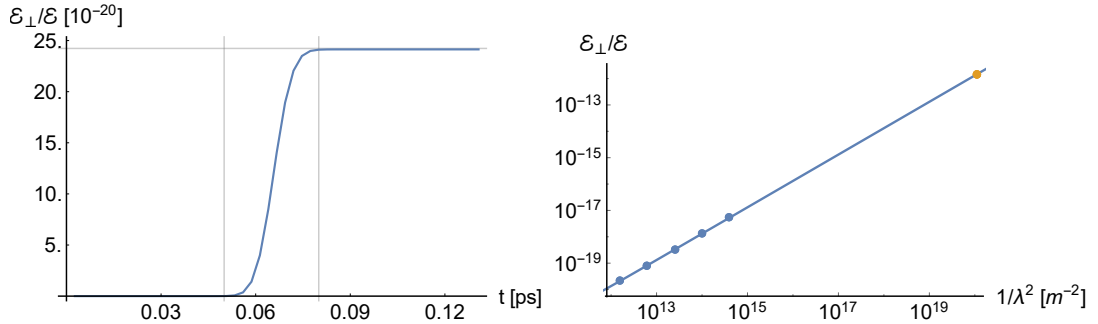


**Figure 6.2.:** To the left we have the time evolution of the polarisation flip in the case depicted on the top of figure 6.4. To the right we have the extrapolation of the wavelength dependent on the polarisation flip energy (blue) and the data point presented in [8] (orange).

The extrapolated values for  $\mathcal{E}_{\perp}/\mathcal{E}$  is  $1.416 \cdot 10^{-12}$  while the value given in the

reference paper is  $1.39 \cdot 10^{-12}$ . This error, while large, is to be expected due to the 1D approximation.

### Parametric scans

Using the simulation settings in table 6.2 with  $\lambda_{pr} = 400$  nm as a reference point, the parametric dependencies in (6.7) can be examined. The dependency of  $\mathcal{E}_\perp/\mathcal{E}$  on the wavelength  $\lambda_{pr}$  is shown in figure 6.2. The quantity  $\mathcal{E}_\perp/\mathcal{E}$  as a function of the relative angle  $\sigma$  between the polarizations of probe and pump and the amplitude  $A$  of the pump pulse are shown in figure 6.3.

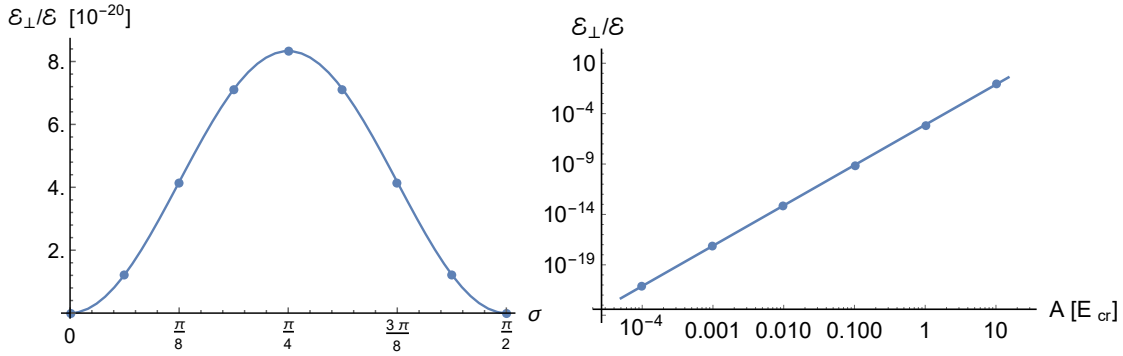


**Figure 6.3.:** **Left:** Plot of the relative polarization flipping vs. angle  $\sigma$  between probe and background pulse polarizations using the settings from table 6.2 with  $\lambda_p$  set to 400 nm. The dots are the values obtained via simulation and the solid line is the prediction using (6.7). Note that the relative error is less or equal to 0.3% for all data points. **Right:** Plot of relative polarization flipping vs. background pulse amplitude  $A$  using the parameters from table 6.2 with  $\lambda_p$  set to 400 nm. The dots are the values gained with the help of simulations and the solid line is the prediction using (6.7). The relative error is less or equal to 0.3% for all data points.

The error between numerical and analytic results is below 0.3% in all simulations. Besides that it is worth noting, that the flipping probability is  $1.2 \cdot 10^{-27}$  at  $\sigma = \pi/2$ , which is several orders of magnitude above the numerical noise. This signal should not be there according to (6.7). It is due to high harmonic generation which has been neglected in the analytic derivation of the flipping probability in (6.7). Furthermore, the algorithm fails to converge for  $A > 100 E_{cr}$ , which is expected as it is well beyond the limits set by the weak field expansion.

To verify that  $P_{flip}$  in (6.7) only depends on the total energy of the strong fields the probe pulse passes first different shapes of the strong field density and second different intensities for a given shape of strong field distributions are considered. Figures 6.3, 6.4 and 6.5 show that  $P_{flip}$  behave essentially (higher order processes excluded) as predicted by (6.7).

## 6. Benchmarks

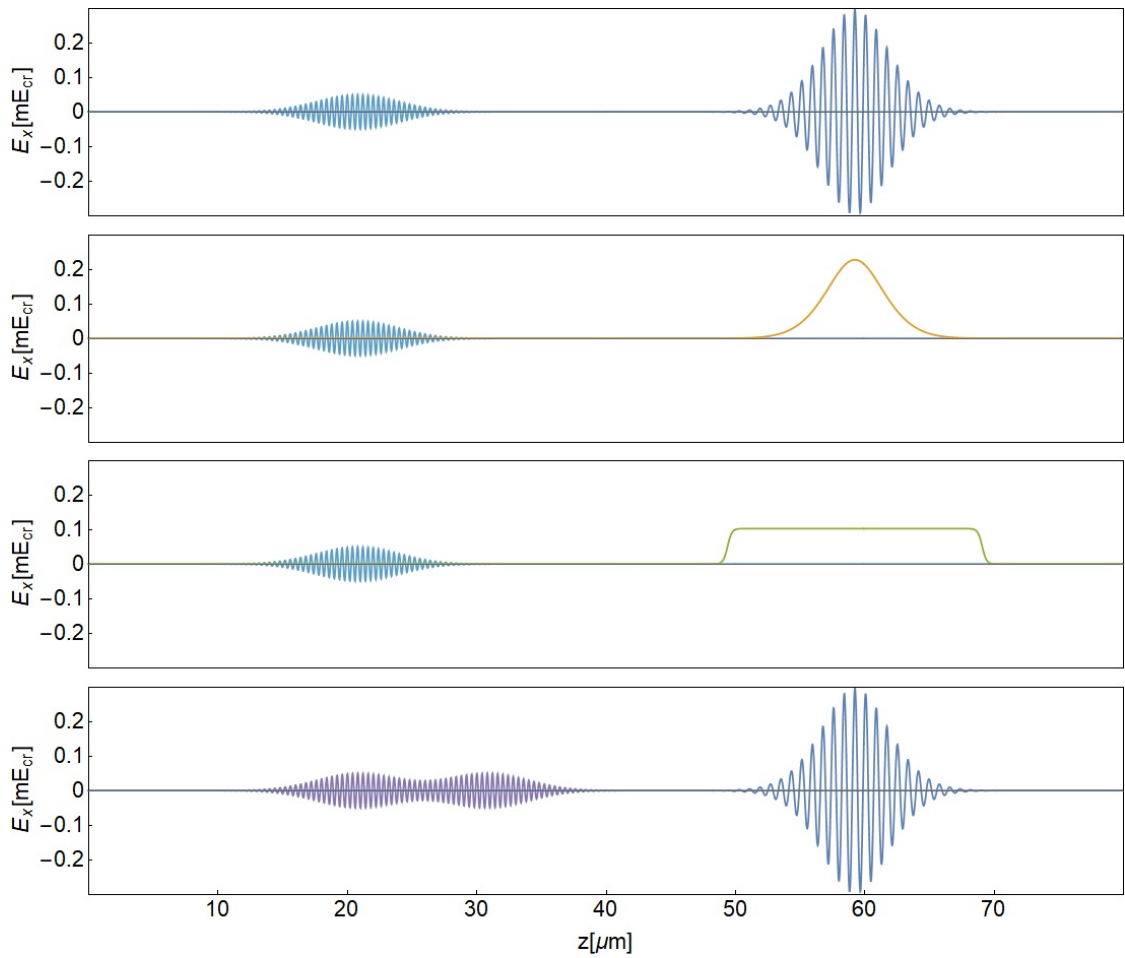


**Figure 6.4.:** Different initial configurations of the em-fields for verification of pulse shape independence. Note that  $\sigma$ ,  $\lambda_{pr}$  and  $E_{pu}$  are the same for all configurations. The reference setting (blue) is the same as the one used in the previous subsection for the benchmark against [8] with  $\lambda_{pr} = 400$  nm, see 6.2. Otherwise there is the 0-frequency pump (orange), the shock regime pump (green) and the chirped probe (purple). The color scheme corresponds to the one used in figure 6.5.

### Pulse shape dependence

Taking once again the settings of table 6.2 with  $\lambda_{pr} = 400$  nm as a reference point, the shape independence of the polarization flipping signal can be put to the test by varying the shape of the pump and probe, while keeping the frequency of the probe and the integral in (6.7) constant. A set of initial conditions with the required variations can be found in figure 6.4.

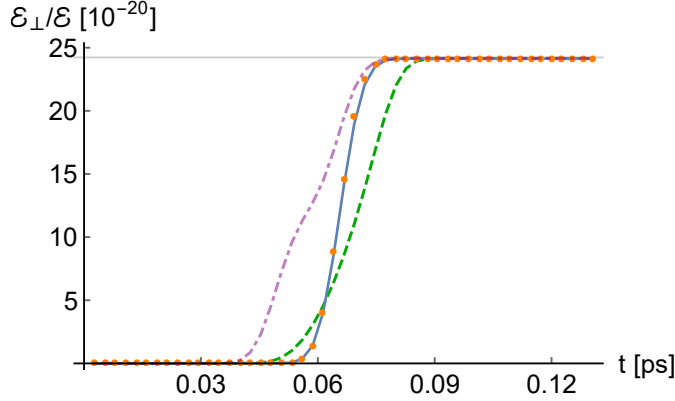


**Figure 6.5.:** Plot of the relative flipping amplitude versus time for the different backgrounds shown in figure 6.4. The color scheme is the same as in figure 6.4. The relative numerical error for the asymptotic value (horizontal line) computed with the help of relation (6.7) is less or equal than 0.5% for all the cases.

As figure 6.5 shows, while each setting has a different time evolution, they all converge against the same value in the asymptotic field.

## 6.3. High harmonic generation

In order to benchmark the generation of higher harmonics, the setup presented in [10] is used. The relevant parameters can be found in table 6.3. In the setup in table 6.3 the background is chosen to be a single cycle pulse with  $|\vec{k}| \gg \omega\tau$ . This is done due to limitation in the front end of the implementation of the QVS algorithm by setting  $\lambda_b = 1$  m, which does not differ from the setup presented in [10] in any noticeable way. A depiction of these initial settings can be found in figure 6.6.

To evaluate the field configurations resulting from the propagation of the initial settings with the QVS algorithm, the signals of the different harmonics need to be separated. In order to do so, a discrete FFT is performed on the data using the algorithms provided by *Mathematica*. Then the data are filtered around the frequency of interest, by setting the rest of the values in the frequency space to

## 6. Benchmarks

Simulation 1709262318		
Description:	Initial settings for the generation of higher harmonics as presented in [10]	
Sim. Box	Size	$300\mu\text{m}$
	# of points	4000
Pump Pulse	$\vec{E}_0$	$(0, 20, 0) \text{ m}E_{cr}$
	$\vec{k}$	$(-1, 0, 0) 1/\text{m}$
	$\vec{x}_0$	$(200, 0, 0) \mu\text{m}$
	$\Phi$	$12.8 \mu\text{m}$
Probe Pulse	$\vec{E}_0$	$(0, 5, 0) \text{ m}E_{cr}$
	$\vec{k}$	$(500, 0, 0) 1/\text{mm}$
	$\vec{x}_0$	$(100, 0, 0) \mu\text{m}$
	$\Phi$	$10 \mu\text{m}$
Notes:	Simulation 1709262354 for contribution from only 4-photon Diagram, 1709262324 only 6-photon See plot of these initial settings in figure 6.6	

**Table 6.3.:** Parameters for the generation of higher harmonics on a zero frequency background with coaxially counter-propagating pump and probe.

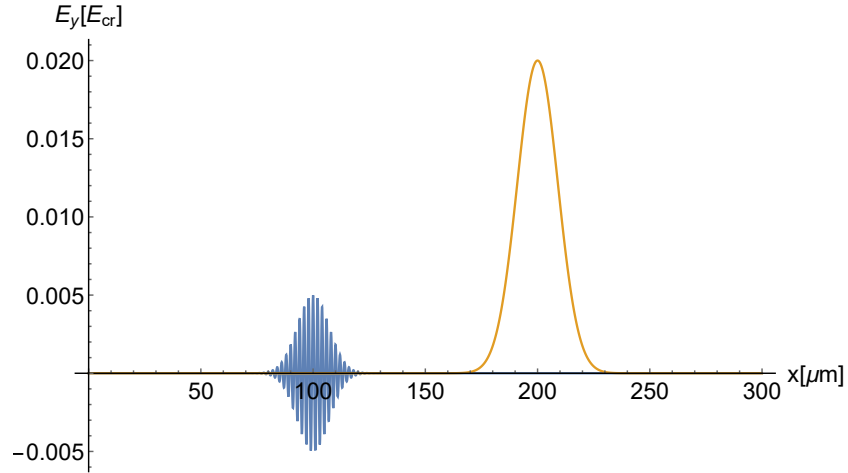


**Figure 6.6.:** Initial settings for the simulation of high harmonic generation against a zero frequency background as defined in table 6.3. The probe pulse (blue) travels to the right and the pump pulse travels to the left.

zero. Due to the finite width of the pump and probe the signals have a finite width in the frequency domain, which needs to be taken into account when filtering. The resulting data are then transformed back into position space and the amplitude of

### 6.3. High harmonic generation

the pulse is measured using the maximum norm on the field data. While this does result in some systematic measurement errors, it does so for both the analytic solution as well as the simulation results. Furthermore, due to the high probe frequencies involved the effect will be barely noticeable.

As the differences caused by the nonlinear interaction are several orders of magnitude below the strengths of the initial fields, the signals for  $\omega = 0$  and  $\omega = \omega_p$  need to be processed further in order to improve visibility. To do so the results of the propagation in classical vacuum  $\mathcal{L} = -\mathcal{F}$  are subtracted from the those of the quantum vacuum. This cancels out the main signal leaving only the difference signal generated by the nonlinearities.

Figures 6.7 to 6.10 show that there is excellent agreement between the simulation results and the analytic expectations given by (2.206). At first glance the absolute amplitude error appears to be  $10^{-15}E_{cr}$ , which given the signal strengths correspond to about 0.02%. Further analysis, however, shows that this difference is due to higher order processes not being taken into account in the computation of (2.206). When considering the signals, which do not suffer from this, the error drops to  $4 \cdot 10^{-18}E_{cr}$ , which corresponds to a relative error of 0.00008%.

Increasing the number of points and increasing the required precision of the ODE solver does not improve these errors, which indicates that the hard wall given by the finite digit representation of the em-field strength in the computer has been reached.

Turning the different contributions on and off enables the identification of the diagrams responsible for the different signals. As expected, the four photon scattering processes dominate when present. It can also be seen, how in the asymptotic field the contributions of the 4 photon high harmonic generation processes in first order disappear leaving only the 6 photon contributions (see figure 6.9). Next, it can be seen that the 3rd harmonic is generated exclusively by the 6 photon diagram as expected (see figure 6.10). Lastly, the change in the 0 frequency field is caused solely by the 6 photon diagram as it is the counterpart to the generation of higher harmonics (see figure 6.7).

## 6. Benchmarks

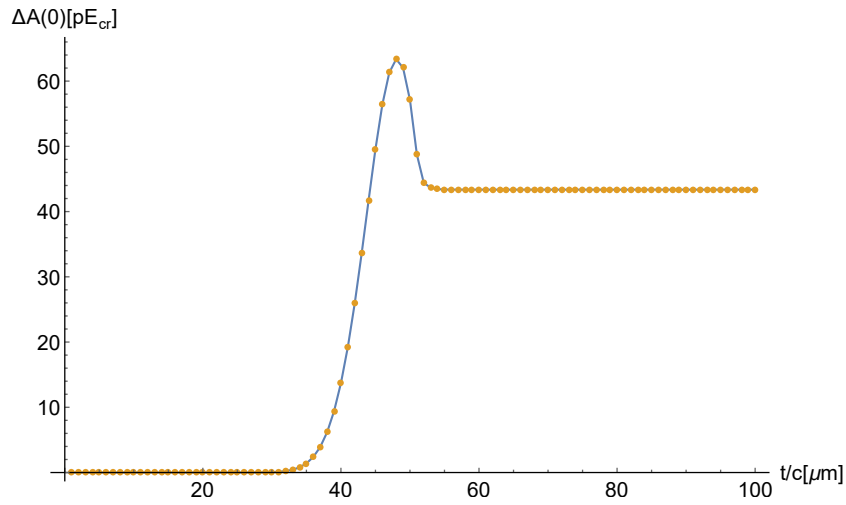


**Figure 6.7.:** Time evolution of the difference between the amplitude of the DC amplitude (0-th harmonic) in the simulation of high harmonic generation against a zero frequency background as defined in table 6.3 and the propagation of the same setup in classical vacuum. The orange dots represent the simulated contribution of the photon scattering, the solid blue line represent the results from (2.206). Note that the whole contribution comes from the 6 photon scattering contributions.

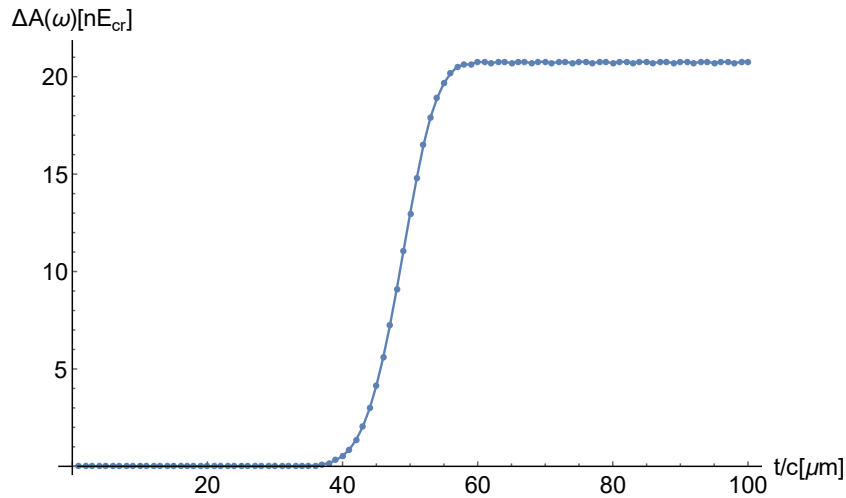


**Figure 6.8.:** Time evolution of the difference between the amplitude of the fundamental harmonic in the simulation of high harmonic generation against a zero frequency background as defined in table 6.3 and the propagation of the same setup in classical vacuum. The blue dots represent the simulated contribution of the photon scattering, the solid blue line represent the results from (2.206). Note the wiggling of the signal in the asymptotic field is a measuring artifact, due to the phase shift between envelope, carrier and measuring points.

### 6.3. High harmonic generation

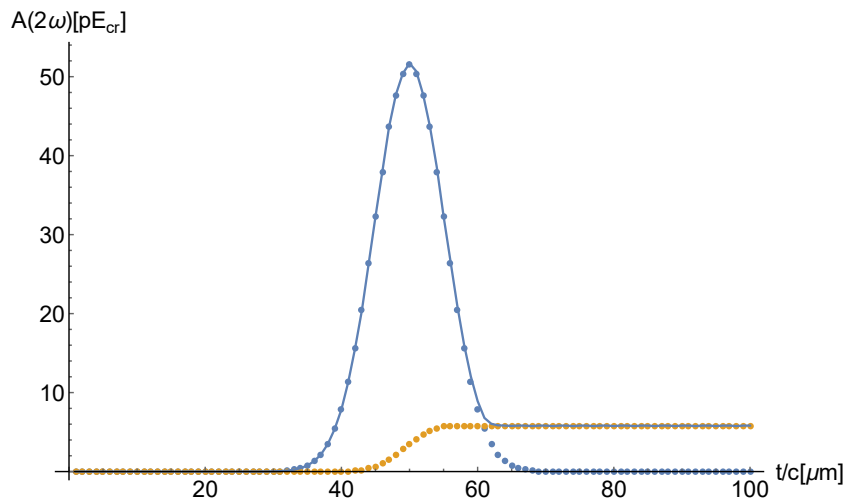


**Figure 6.9.:** Time evolution of the amplitude of the second harmonic in the simulation of high harmonic generation against a zero frequency background as defined in table 6.3. The blue dots represent the simulated contribution from the four photon scattering and the orange dots the contribution from the 6 photon scattering diagramm. The solid blue line represents the results from (2.206)

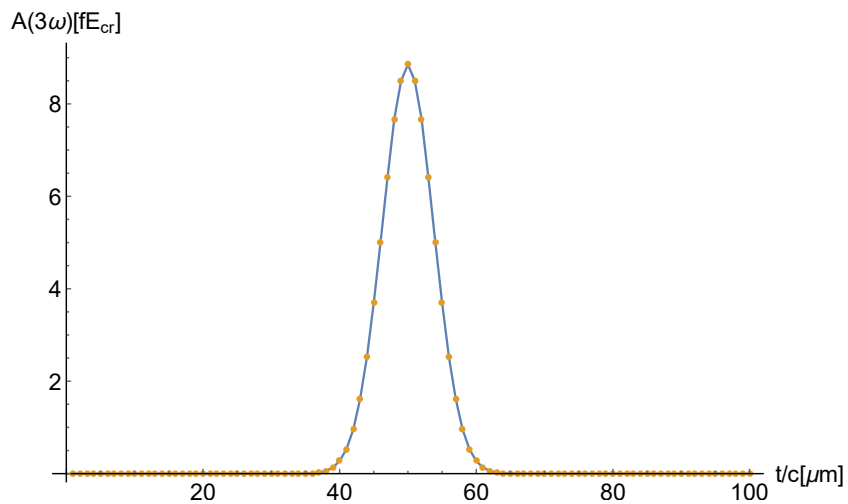


**Figure 6.10.:** Time evolution of the amplitude of the third harmonic in the simulation of high harmonic generation against a zero frequency background as defined in table 6.3. The orange dots represent the contribution from the 6 photon scattering diagramm. The solid blue line represent the results from (2.206)



## 7. Simulation results beyond the scope of analytically solvable setups

As shown in the chapter 6, the algorithm presented in chapter 5 agrees with the analytic examples available. Thus, it can be used to reliably explore the physical realm that lies behind the analytic solvability constraints. To this end a diverse set of initial settings and its time integration results via the QVS algorithm is presented in this chapter, exploring the different properties of the quantum vacuum.

### 7.1. Harmonic generation in the nonzero frequency background case

One analytic assumption that can be easily removed in simulations while remaining in the one dimensional case, is the need for a zero frequency background in [10]. This will separate the degenerate signals as, e.g.,  $2\omega_{pr} + \omega_{pu} \neq 2\omega_{pr} - \omega_{pu}$ .

To this end the simulation presented in 6.3 is modified by setting the frequency of the background pump to  $\omega_{pu} = 0.1 \omega_{pr}$ . Furthermore, both pulses are broadened in physical space in order to achieve a sharper contrast in frequency space. The resulting parameters can be found in table 7.1.

Figure 7.1 shows the result of this simulation. As expected the signal splits up into 14 channels. Note that there would theoretically be  $4\omega_{pr} \pm \omega_{pu}$  channels, however, their strength falls below the numerical noise level. Also, only the positive frequencies have been depicted since by the mathematical properties of the FFT the spectra will be perfectly symmetric.

The dominating signal, both in overlap and asymptotic spectra, is at  $\omega_{pu}$  and  $\omega_{pr}$ . The signal comes primarily from the scattering of one pump and one probe photon via the 4-vertex box. Since it is the process that requires the least amount of interacting photons (two photons) it is clear that it will have the greatest cross section and thus the strongest signal.

7. Simulation results beyond the scope of analytically solvable setups

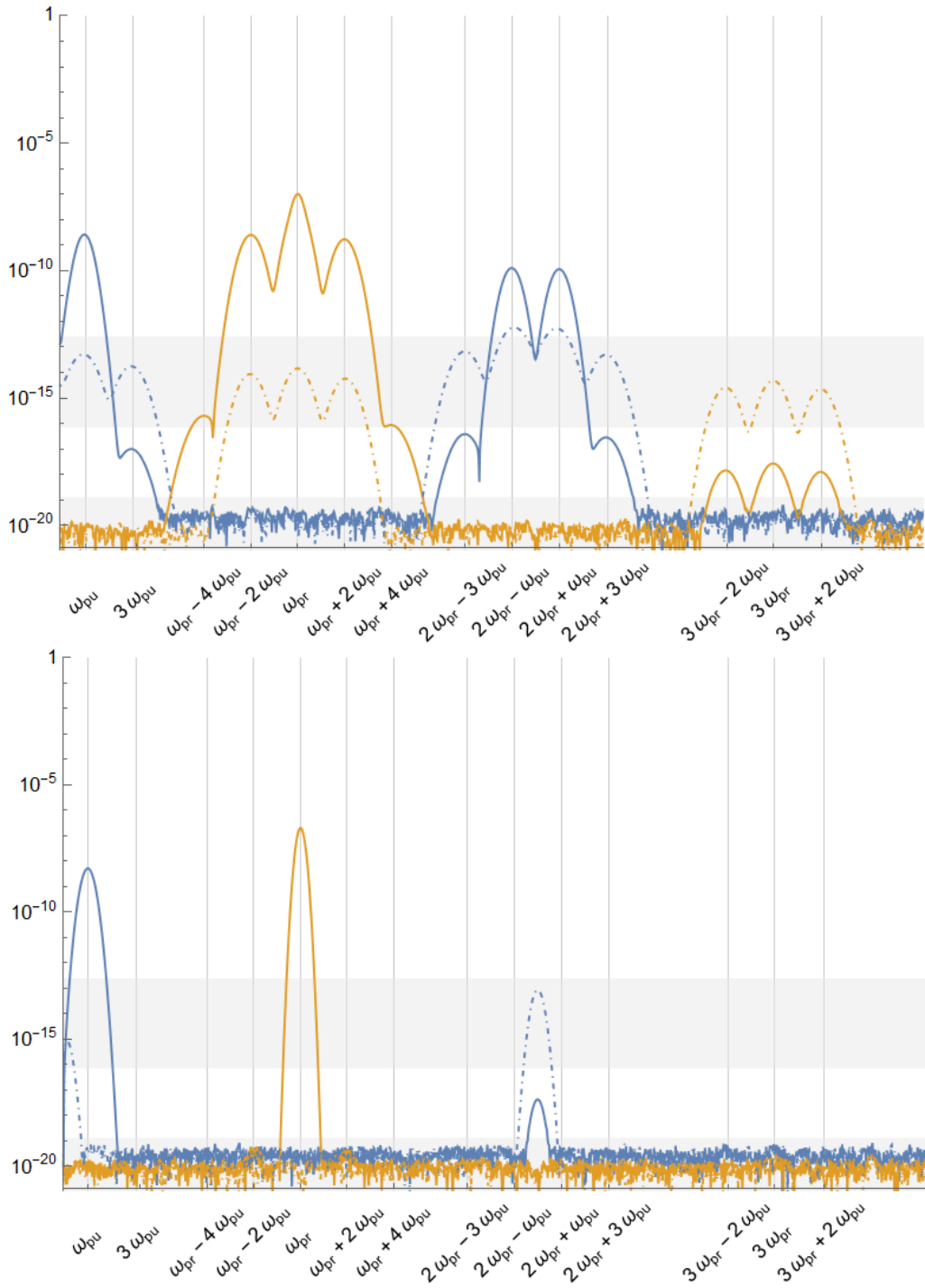


**Figure 7.1.:** Plots of the  $\Delta E_z$  (blue) and  $\Delta E_y$  (orange) for a coaxial collision of two Gaussian pulses with frequencies at a relation  $\omega_{pr} = 10\omega_{pu}$ . The solid lines represent the contributions from 4-photon diagram contributions and the dashed one 6-photon diagram contributions. The plot on the top is for the field values at the overlap, the one on the bottom is for the asymptotic values. The grey grid lines represent the predicted signature channels. The different backgrounds represent the different regimes, the lowermost is the noise regime, the one above that is the 2nd order 4-photon interaction contribution regime, above that is the 1st order 6-photon interaction contribution regime and finally on top is the 1st order 4-photon contribution regime. Note that the simulation error is guaranteed to be below the  $10^{-19}$  mark.

Simulation 1709252215		
Description:	Initial settings for the generation of higher harmonics on a nonzero frequency background with coaxially counterpropagating pump and probe	
Sim. Box	Size	660 $\mu\text{m}$
	# of points	11000
Pump Pulse	$\vec{E}_0$	(0, 0, 20) $\text{m}E_{cr}$
	$\vec{k}$	(-50, 0, 0) 1/mm
	$\vec{x}_0$	(440, 0, 0) $\mu\text{mm}$
	$\Phi$	40 $\mu\text{m}$
Probe Pulse	$\vec{E}_0$	(0, 5, 0) $\text{m}E_{cr}$
	$\vec{k}$	(500, 0, 0) 1/mm
	$\vec{x}_0$	(220, 0, 0) $\mu\text{mm}$
	$\Phi$	25.6 $\mu\text{m}$
Notes:	Simulation 1709252228 for contribution from only 4-photon Diagram, 1709252242 only 6-photon and 1709252203 for none at all See Figure 7.1 for results.	

**Table 7.1.:** Parameters for the generation of higher harmonics on a nonzero frequency background with coaxially counter-propagating pump and probe.

Next, several orders of magnitude below comes the photon merge signal of the 4-photon diagram. As in the zero frequency background case these signals disappear in the asymptotic field.

About 5 orders of magnitude below the 4-photon merge signal come the scattering and merging signals for the 6-photon diagram. Again, the signals mostly disappear in the asymptotic field leaving only two peaks above the error bar at  $2\omega_{pr}$  and a 0-frequency peak.

Last, there are some signals in the 4-photon contribution, that can only occur through 2nd order interactions, i.e., a photon that has merged in a 4-box diagram is merged again. This includes also the generation of a higher harmonics.

## 7.2. Gaussian Beams in 2 Dimension

As full 3D simulations are extremely expensive, the models explored in the rest of this chapter rely on 2D simulations.

With this in mind, special 2D Gaussian pulses need to be introduced, in order to take the increase of the pulse amplitude due to dispersion into account. To do so the factor  $w_0/w(z)$  in the 3D Gaussian needs to be replaced by  $\sqrt{w_0/w(z)}$

## 7. Simulation results beyond the scope of analytically solvable setups

yielding, w.l.o.g. in  $z$ -direction

$$\vec{E}(x, z, t) = \vec{E}_0 \sqrt{\frac{w_0}{w(z)}} e^{-\left(\frac{r}{w(z)}\right)^2} e^{-\left(\frac{z-z_t}{\Phi_t}\right)} \cos\left(\frac{k r^2}{2 R(z)} + \zeta(z) - k z\right), \quad (7.1)$$

where  $\vec{E}_0$  is the strength of the electric field at the peak. the quantity  $w_0$  is the waist of the beam, i.e., the radial distance from the propagation axis at  $z = z_0$ , where the field strength has decayed by a factor of  $1/e$ . The quantity  $w(z)$  is the waist at the position  $z$  given by

$$w(z) = w_0 \sqrt{1 + \left(\frac{z - z_0}{z_R}\right)^2}. \quad (7.2)$$

The distance to the propagation axis  $r$  is  $x$ . The Rayleigh length  $z_R$ , i.e., the longitudinal distance from  $z_0$  at which the waist has increased by a factor of  $\sqrt{2}$  and is given by

$$z_R = \frac{\pi w_0^2}{\lambda}. \quad (7.3)$$

The quantities  $z_t$  and  $\Phi_t$  describe the Gaussian envelope in  $z$ -direction. The wave number  $k$  is defined as

$$k = \frac{2\pi}{\lambda}, \quad (7.4)$$

and  $R(z)$  is the curvature of the beam given by

$$R(z) = z \left(1 + \left(\frac{z_R}{z}\right)^2\right), \quad (7.5)$$

Finally,  $\zeta(z)$  is the Gouy phase, given by

$$\zeta(z) = \arctan \frac{z}{z_R}. \quad (7.6)$$

A sketch of how all these variables are interconnected is shown in figure 7.2.

The factor  $\sqrt{w_0/w(z)}$  in (7.1) can be easily derived from the behavior of the wave in the far field  $z \gg z_R$ . The wave behaves in the limit  $z \gg z_R$  like a cylindrical wave since it is assumed to be constant in the  $y$  direction. A 3D Gaussian in the far field, becomes a spherical wave. In both, the 2D and 3D Gaussian cases, the total intensity in the far field depends solely on the  $w_0/w(z)$  term since all the other terms average out on integration.

In order for the pulse energy to be, more or less, conserved the  $w_0/w(z)$  term contribution has to scale as the surface area of the wave, which in case of the 3D Gaussian is  $\propto \frac{4}{3}\pi z^2$ . Since the surface area of the 2D Gaussian is  $\propto 2\pi z$ , neglecting the constants, the contribution in this case has to be the root of the contribution in the 3D case, thus the need to put a root on the  $w_0/w(z)$  term in (7.1).

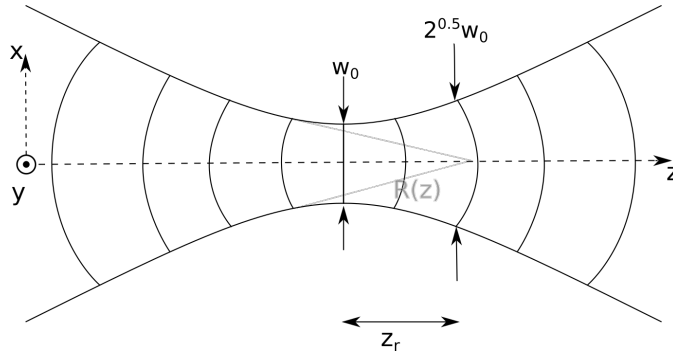


Figure 7.2.: Sketch of a 2D Gaussian beam.

## 7.3. Non-coaxial collisions

Setting the frequency of the pump beam to be the exact same as the frequency of the probe leads to the signal channels to be again degenerate. This is a good starting point for studying the effects of the beams non-coaxial pulses, since in this case the degeneracy disappears as soon as  $\vec{\omega}_{pr} \neq \pm \vec{\omega}_{pu}$  even if  $|\vec{\omega}_{pr}| = |\vec{\omega}_{pu}|$ . To analyse the effect a set of simulations is run (see Figures 7.3, 7.4, 7.5, 7.6 and 7.7) starting from the quasi-1D case, going to orthogonal collisions, and then to odd angles.

### 7.3.1. The quasi 1D case

The first simulation is the quasi-1D case, which is a bridge between the 1D and 2D cases. While 2D Gaussian pulses are used as described above with the parameters given in Table 7.2, they both propagate along the  $x$ -axis and have the same focal point. Furthermore, they are propagated in two dimensions, however, the  $y$ -direction is arbitrary and does only contribute dispersion effects.

As expected the overlap and asymptotic signals behave like in the one dimensional case, with  $3\omega$  and  $5\omega$  signals in the overlap and only a much weaker  $3\omega$  signal in the asymptotic field. Note that the pump/probe indices are not needed, since the signal is degenerated. There is, however, already broadening of the  $\omega$  signal in the frequency space, which can not be observed in a purely 1D setup. This agrees neatly with predictions for higher dimensions as for example in [8], since the birefringence effects are nonlinearly stronger in the center of the pulse and thus the resulting shifted pulses are sharper in position space and thus broader in the frequency domain.

7. Simulation results beyond the scope of analytically solvable setups

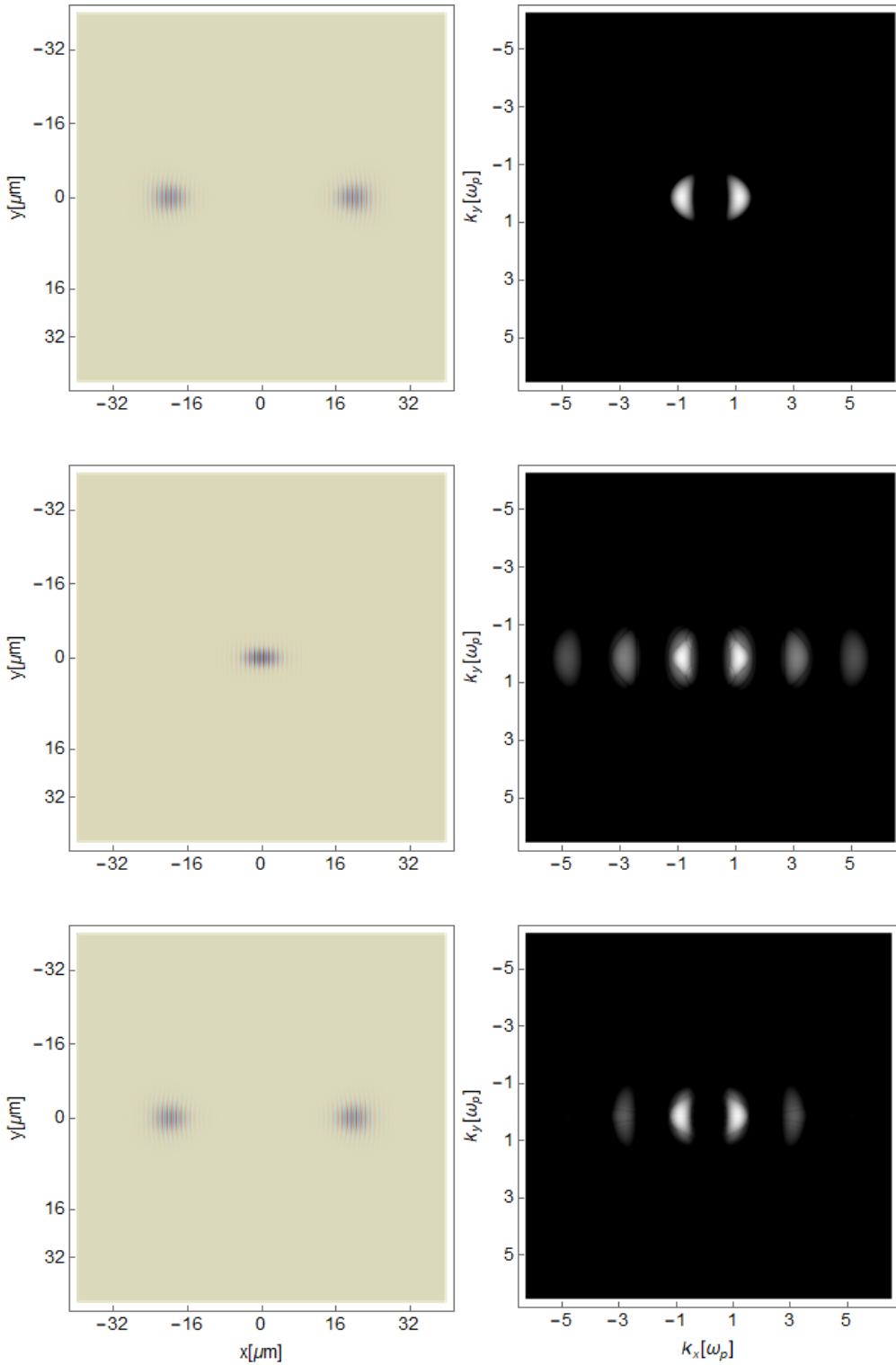


**Figure 7.3.:** Plots of simulated values for  $E_z$  for two co-axially propagating Gaussian pulses  $E_0 = 0.05E_{cr}$ . The plots to the left are in physical space and the ones to the right are in frequency space. The two on top are the initial settings, the ones in the middle are the overlap state and the ones on the bottom represent the field configuration after the collision.

<b>Simulation 1708030002</b>		
Description:	Initial settings for the Simulation of the quasi 1D collision of two similar pulses.	
Sim. Box	Size	$80\mu\text{m}\times 80\mu\text{m}$
	# of points	$1024 \times 1024$
Pump Pulse	$\vec{E}_0$	$(0, 0, 50) \text{ m}E_{cr}$
	$\hat{k}$	$(1, 0, 0)$
	$\vec{x}_0$	$(40, 40, 0) \mu\text{mm}$
	$w_0$	$4.6 \mu\text{m}$
	$z_r$	$16.619 \mu\text{m}$
	$\lambda$	$4 \mu\text{m}$
	$z_t$	$20 \mu\text{m}$
	$\Phi_t$	$4.5 \mu\text{m}$
Probe Pulse	$\vec{E}_0$	$(0, 0, 50) \text{ m}E_{cr}$
	$\hat{k}$	$(-1, 0, 0)$
	***	all other parameters as for the pump
Notes:	See Figure 7.3 for results.	

**Table 7.2.:** Parameters for the collision of two pulses with the same frequency in 2 dimensions.

### 7.3.2. Collisions between pulses with the same polarization at an angle

The next step is to once again split the signal by making the  $\omega$ 's distinguishable in frequency space. To this end the  $\hat{k}$  parameter for the probe in Table 7.2 is changed to  $(0, 1, 0)$  for simulation #1708030130 and to  $(-1/\sqrt{2}, 1/\sqrt{2}, 0)$  for simulation #1708030533 (see figure 7.4 and figure 7.5 respectively for results.)

Starting with the orthogonal collision, it can be observed that the signal channels spread in a similar way as they do in the nonzero frequency background case. Only that this time the separation of the signal peaks is not along the  $k_x$ -axis but along the orthogonal  $k_y$ -axis. The other difference to the 1D case is that due to the larger amount of points across which the Fourier transformation averages, the noise level is reduced. This combined with the stronger peak field strengths, makes the channels that merge 5 photons at once visible.

In the far field it can be seen how once again nearly all the signals disappear. The birefringence effect is no longer symmetric. This is expected since the system should remain invariant under boost transformations, which themselves result in asymmetry. The effect of the birefringence can also be observed on the higher harmonics. This has also caused the creation of a secondary higher harmonic signal, whose existence is required in order to keep the total momentum in the

7. Simulation results beyond the scope of analytically solvable setups

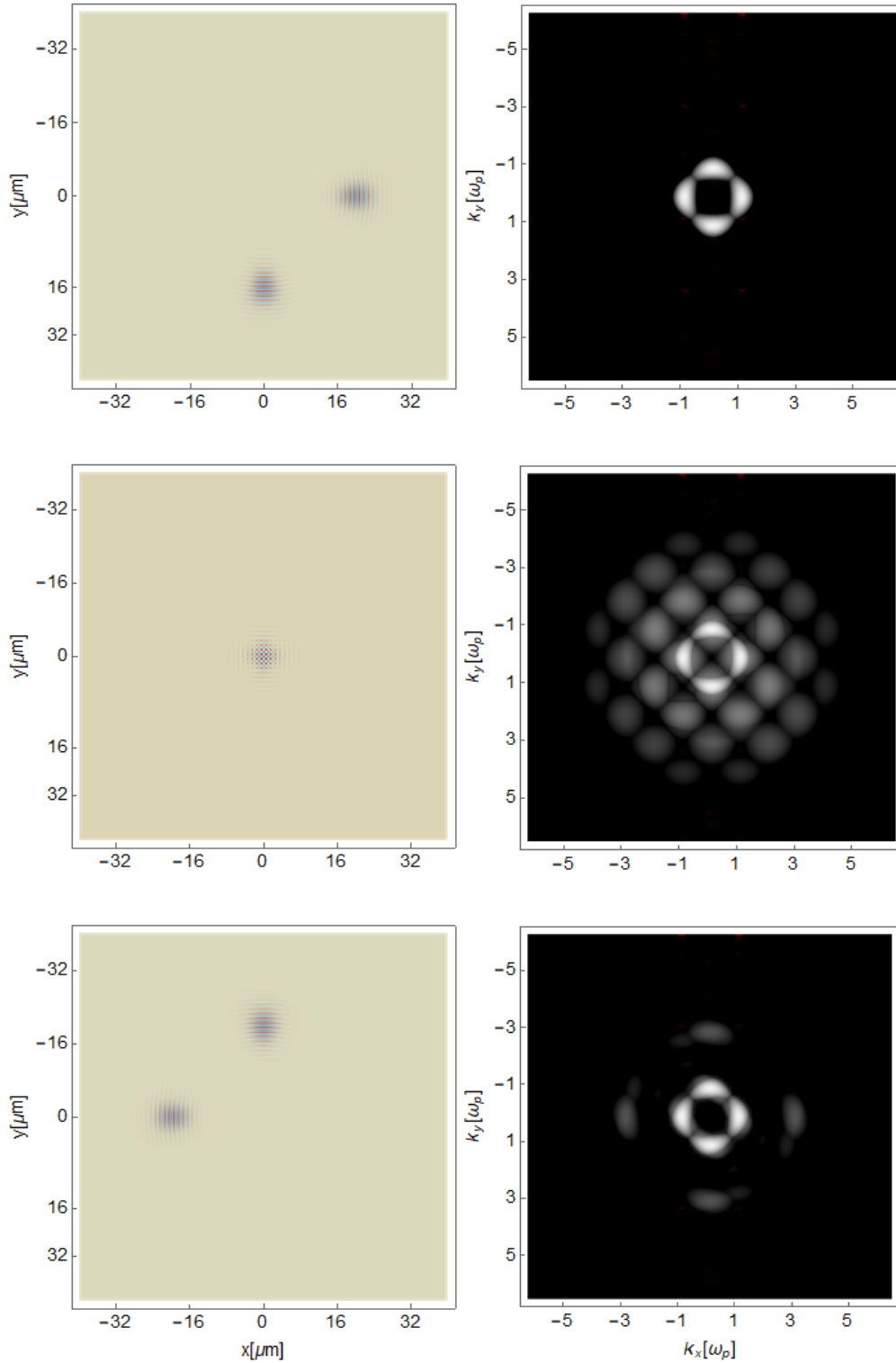


**Figure 7.4.:** Plots of simulated values for  $E_z$  for two orthogonally propagating Gaussian pulses  $E_0 = 0.05E_{cr}$ . The plots to the left are in physical space and the ones to the right are in frequency space. The two on top are the initial settings, the ones in the middle are the overlap state and the ones on the bottom represent the field configuration after the collision.

### 7.3. Non-coaxial collisions

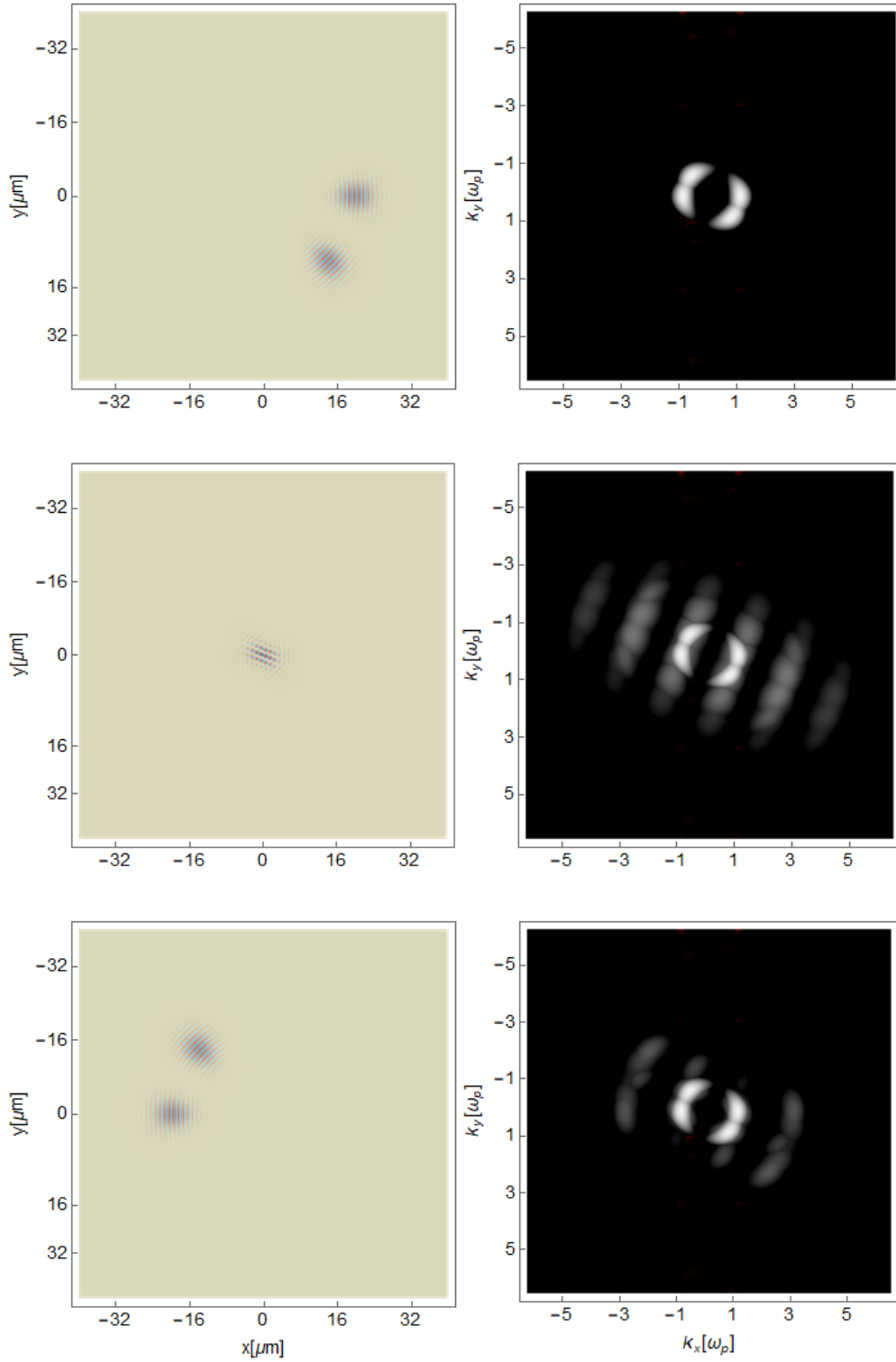


**Figure 7.5.:** Plots of simulated values for  $E_z$  for two propagating Gaussian pulses  $E_0 = 0.05E_{cr}$  at an angle of 45 deg. The plots to the left are in physical space and the ones to the right are in frequency space. The two on top are the initial settings, the ones in the middle are the overlap state and the ones on the bottom represent the field configuration after the collision.

## 7. Simulation results beyond the scope of analytically solvable setups

system constant.

The case of the odd angle collision can now be mostly seen as a boost transformation of the orthogonal case. There are, however, two notable exceptions. Firstly, the symmetry along the line bisecting the two propagation axes is broken. This is not a physical feature since the analytic PDE's with the given initial setup have this symmetry. It is a numerical artifact arising from the fact that a cartesian grid is being used and therefore the two projections and subsequent time-integrations of the Gaussian pulses are not the same.

Secondly, there appears a signal close to  $\omega$  in the spectrum. This is most likely caused by the reflection of the pulses on one another and will be further studied in a later section. Note, that both this result and the secondary signal visible close to the higher harmonic, might be numerical artifacts, since they are below the error bar.

### 7.3.3. Polarization tagging of colliding pulses

To gain more information of the pulse contributions to the different signals the pulses can be tagged by using orthogonal polarizations. Due to momentum conservation the resulting signals have the polarization of the pulse, that contributes an odd amount of photons. To this end the simulations in subsection 7.3.2 are modified by exchanging the polarization of the probe pulse from  $(0, 0, 1)$  to  $\hat{k} \times (0, 0, 1)$ . Furthermore, the angle in the non-orthogonal collision is changed from  $\pi/4$  to  $3\pi/4$ .

The results in Figure 7.6 and 7.7 show that the effects remain largely the same and the mixing is analogous to the one presented in figure 7.1. It is worth noting that the secondary signals are orthogonal to the primary ones they accompany which is another indicator, that they emerge from reflection. Once again, however, their significance is in question as they are below the numerical error bar.

## 7.4. Focusing of light by light

As mentioned on the evaluation of the quasi-1D case, the different refractive indices caused by the vacuum nonlinearities will cause a deformation of the original pulse form. To further study the focusing effect, a picture analogous to the classical focusing of a plane wave by a crystal lens is used as a starting point (see figure 7.8). Here, the function of the lens is to delay the plane wave into the center of the lens by an amount, that is larger at than at the outer parts of the latter, causing a bending of the phase-fronts and leading to a focusing effect. A delay may also be achieved by colliding a strong Gaussian pulse with the plane wave. As the strength of the nonlinearity and thereby the delay caused by it, decrease with decreasing

#### 7.4. Focusing of light by light

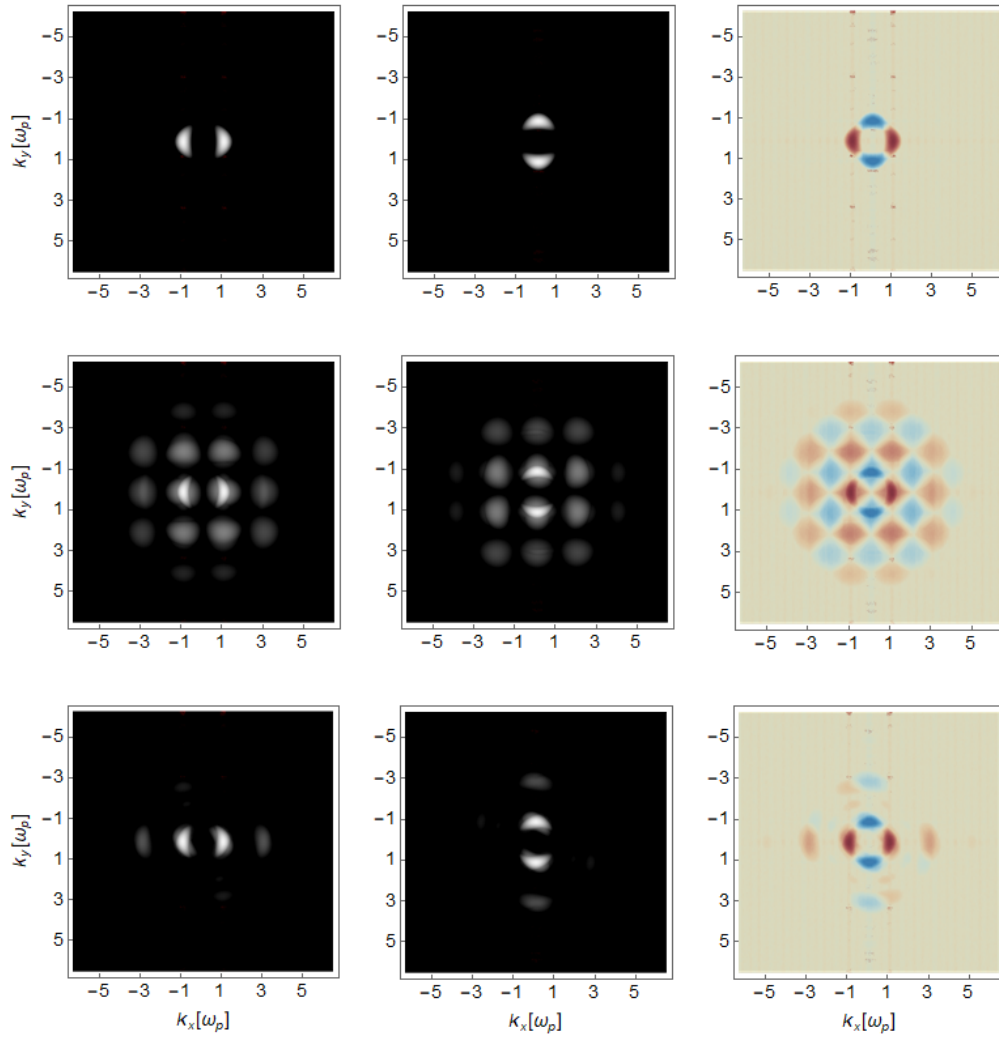


**Figure 7.6.:** Plots of simulated values for  $E_z/E_y/E_z - E_y$  for two orthogonally propagating Gaussian pulses  $E_0 = 0.05E_{cr}$ . Note that the one is a transversal magnetic pulse and the other a transversal electric pulse. The plots are all in frequency space. The three on top are the initial settings, the ones in the middle are the overlap state and the ones on the bottom represent the field configuration after the collision.

7. Simulation results beyond the scope of analytically solvable setups

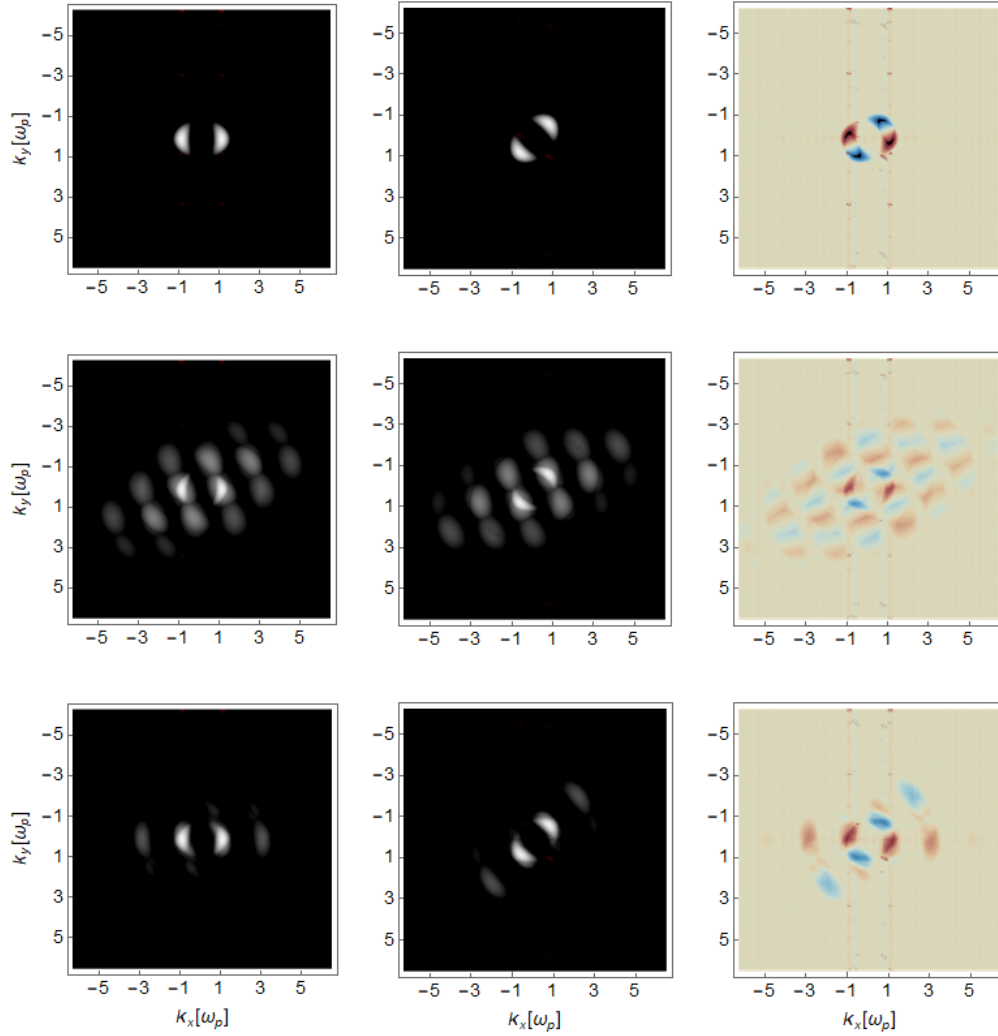


**Figure 7.7.:** Plots of simulated values for  $E_z/B_z/E_z - B_z$  for two propagating Gaussian pulses  $E_0 = 0.05E_{cr}$  at an angle of 135 deg. Note that the one is a transversal magnetic pulse and the othe a transversal electric pulse. The plots are all in in frequency space. The three on top are the initial settings, the ones in the middle are the overlap state and the ones on the bottom represent the field configuration after the collision.

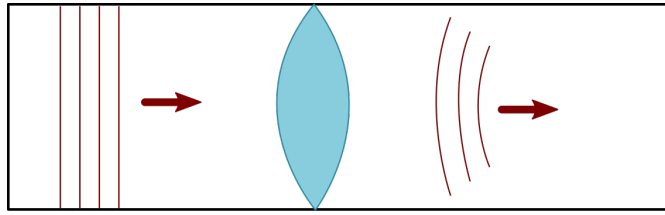


**Figure 7.8.:** Sketch of a plane wave focused by a lens.

field strength, the resulting pattern of delay is similar to the one caused by the lens.

Figure 7.9 shows such a setup. As the intensity of the Gaussian pulse used as the lens is selected within an experimentally realistic range, the focusing effect is quite weak, hence to visualize it, the Fourier transformation of the plane wave after the collision is computed (see figure 7.10).

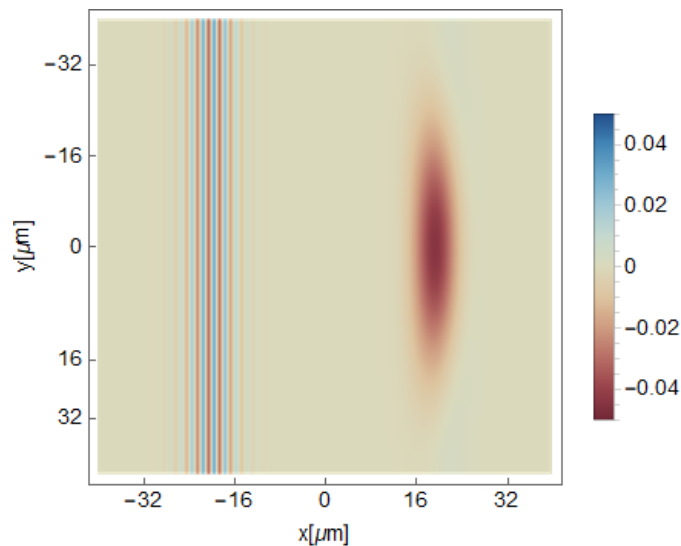


**Figure 7.9.:** Plot of the initial setting for the focusing of light by light simulation. The field strengths are given in units of  $E_{cr}$ . The plane wave to the left will travel to the right through the counter-propagating gaussian pulse to the right.

In figure 7.10 it can clearly be seen how the profile varies from a delta shape in  $k_y$  before to a finite width in  $k_y$  after the interaction. Given the properties of the Fourier transformation this means that the phase front of the plane wave are curved, which is characteristic of a focusing wave.

## 7. Simulation results beyond the scope of analytically solvable setups

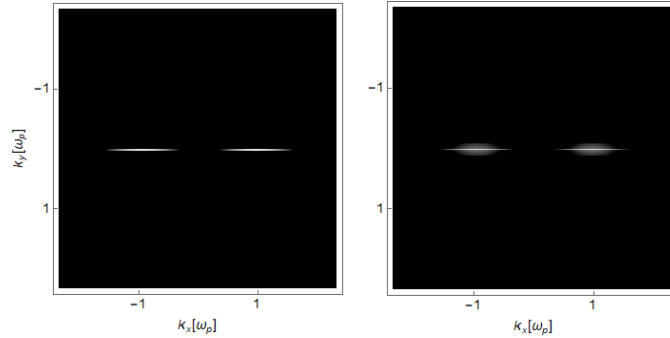


**Figure 7.10.:** Plot of the Fourier transformation of the plane wave before (left) and after (right) it propagates through the Gaussian beam. It can be observed how the delta spectrum in  $k_y$  space broadens into a parabolic spectrum. As the width in position space is inverse to the width in Fourier space this means that the pulse will have focused.

## 7.5. Reflection effects at the pump

Keeping in line with the optical analogon of seeing strong fields as a material, the next thing to look at is be diffraction and refraction. In the classical case a pulse encountering a material boundary is partially reflected and refracted (see figure 7.11).

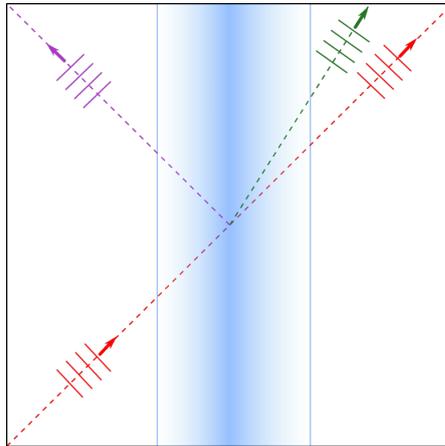


**Figure 7.11.:** Sketch of the partial reflection (purple) and refraction (green) of a plane wave (red) in a medium with  $n_{\text{med}} \neq n_{\text{vac}}$ .

When using a low frequency plane wave instead of a material the collision between pump and probe is adiabatic. Classically this implies that the reflection is suppressed [39]. Setting the experiment up as shown in figure 7.12 and time-evolving the setup until the two counter-propagating fields have separated again, results in no visible diffraction or refraction. Only when they are overlapping can a slight

### 7.5. Reflection effects at the pump

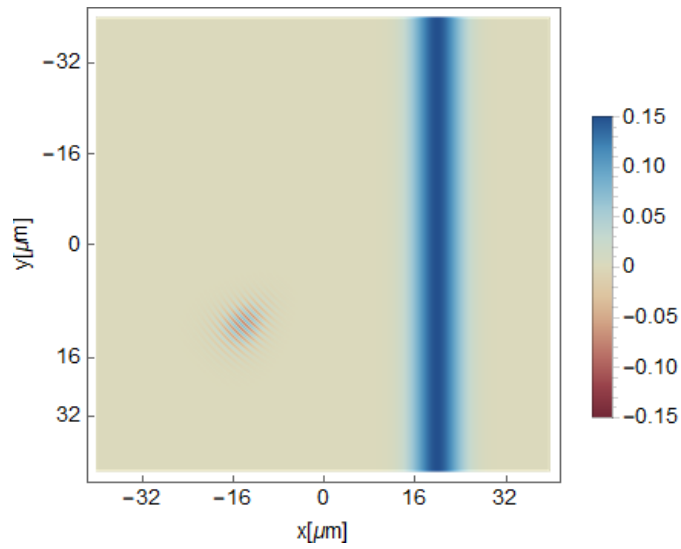


**Figure 7.12.:** Plot of the initial setting for the reflecting/refracting of light by light simulation. The field strengths are given in units of  $E_{cr}$ . The plane wave to the left travels to the right through the counter-propagating Gaussian pulse to the right.

deviation be seen in the Fourier space (see figure 7.13). In hindsight, it is expected

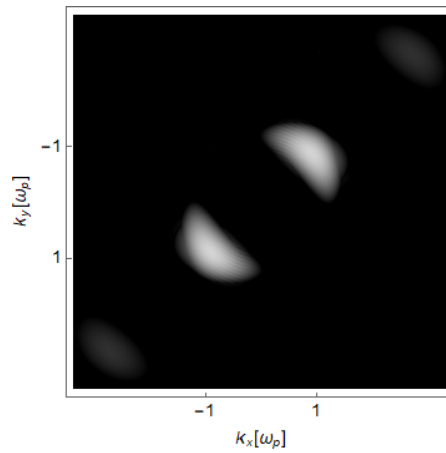


**Figure 7.13.:** Plot of the Fourier transformation of the Gaussian beam in the refraction experiment at overlap. It can be seen that there is no reflection signal and there is only a slight refraction signal that can barely be seen underneath the probe signal.

that the effect is almost negligible, since the nonlinear optical effect is weak, as already discussed in the previous section. In addition, due to the adiabatic rise in the field strengths it is additionally suppressed.

## 7.6. Rabi oscillations

Lastly, the question of what happens when the intensity of the pump beam is pushed to the point, where the flipping probability exceeds 100% is addressed. This situation is achieved in simulations by using an extremely strong pulse  $\sim 20E_{cr}$ . While such a strong pulse no longer satisfies the weak field condition, the same effect can be achieved with a longer, lower energy pulse. This is not done here for computation time optimization purposes. A more thorough calculation of what happens in this regime can be found in [40].

A depiction of these initial settings can be seen in figure 7.14. Note, that a flat top pump is used to support a large amplitude of the pump with small spatial spread.

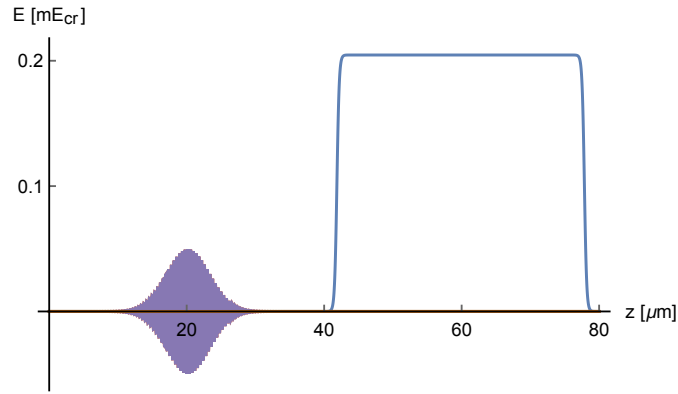


**Figure 7.14.:** Initial electric field settings for the high intensity simulation described above. Note that the Pump field was reduced by a factor of  $10^{-5}$  to improve visibility

As can be seen in figure 7.15, there is an oscillation in time of  $\mathcal{E}_\perp/\mathcal{E} = N_\perp/N$ ,  $N_\perp$  being the number of orthogonal photons and  $N$  the total amount of photons. However, the oscillation amplitude does not vary between 0 and 1 but between 0.3 and 0.7.

This is due to the fact, that the probe pulse finite in time and thus the front part of the probe always sees more of the pump pulse than the rear part on the latter, thus yielding an overlap of multiple oscillations, which results in an oscillation with smaller amplitude.

To clean out this effect a second simulation with a shorter probe pulse width is made, where used  $\Phi = 1.125[\mu s]$ . Furthermore, to visualize more oscillation cycles the width  $w$  of the pump is also enlarged to  $w = 60[\mu m]$ .

As can be seen in figure 7.16 the amplitude of the oscillations has increased with respect to the amplitude in the previous simulation, as expected. However a new effect in form of a dampening of the oscillation amplitude has appeared.

While unexpected in the photon picture used in the derivation of (2.192), it is not outside of what is expected in the coherent wave picture. As it is well known

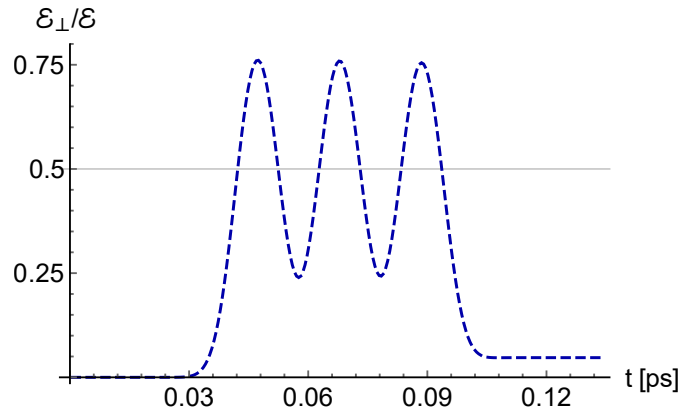


**Figure 7.15.:** Plot of the results of the high intensity simulation for the time evolution of the number of photons with a polarisation orthogonal to the original beam.

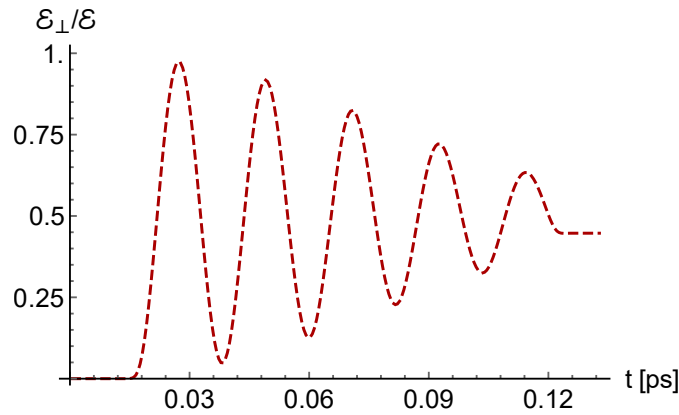


**Figure 7.16.:** Plot of the results of the resolution increased high intensity simulation for the time evolution of the number of photons with a polarisation orthogonal to the original beam.

[13, 41] the vacuum polarization generated by the pump pulse results in a different refractive index in dependence of the polarization, i.e.  $n_\perp \neq n_\parallel$ . This manifests itself in the pulses propagating at different speeds in dependence of their polarization.

Now, if the probe pulse is decomposed in two parts, one is polarized parallel to the pump and one orthogonal to it. It follows, that the parallel part moves slower such that a shift  $\Delta x$  between the two parts is created (see figure 7.17). After has propagated long enough through the pump,  $\Delta x$  is equal to  $\lambda$  and the phase shift between the two parts is zero. However, as now the maxima of the field amplitude of both pulses are no longer aligned with one another but with the first side lobe, the resulting polarization vector is no longer the bisector of their

7. Simulation results beyond the scope of analytically solvable setups

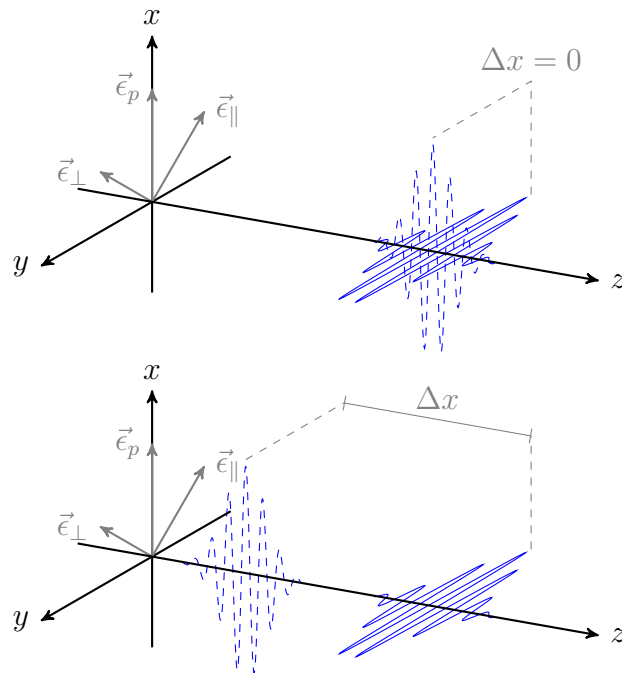


**Figure 7.17.:** Qualitative representation of the probe pulse before (left) and after (right) passing the pump. Note that in the beginning the probe is linearly polarized in  $\vec{\epsilon}_{\parallel}$  direction and thus the  $\mathcal{E}_{\perp}$  as given in (6.8) will be 0. After the collisions there are two non-overlapping linearly polarized pulses at a  $\pi/2$  angle to  $\vec{\epsilon}_{\parallel}$  as well as to  $\vec{\epsilon}_{\perp}$  and thus  $\mathcal{E}_{\perp} = \mathcal{E}_{\perp} = 0.5$

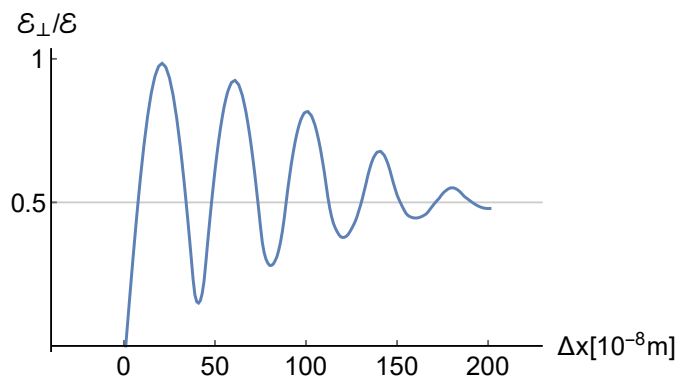


**Figure 7.18.:** Results of the model for the time evolution of the number of photons with a polarization orthogonal to the original beam. Note that  $\Delta x(t) = (t - 0.015\text{ps}) 1.3 \cdot 10^{-3}\text{m/ps}$

polarization, but is skewed to one side. As  $\Delta x$  increases, this effect increases up to the point, where the two parts are completely separated, resulting in a constant  $\mathcal{E}_\perp/\mathcal{E} = 0.5$ . Figure 7.18 shows this polarization evolution and it can be seen that the form agrees with the one seen in figure 7.16.

This asymptotic effect can only be explained in the coherent wave picture but not in the photon picture.



## 8. Summary and conclusions

In chapter 1, a set of modified Maxwell equations is derived from first principles. Starting from the Dirac equation and using renormalization theory two approximations are made. Firstly, the wavelengths involved in the interaction are assumed to be larger than the Compton wavelength and secondly, the intensity of the fields is assumed to be below the Schwinger field intensity, suppressing thereby the creation process of real electron-positron pairs.

In chapter 2 Schwinger's proper time formalism, nonperturbative pair production rates, the weak field expansion, and the resulting modified Maxwell are reviewed. Furthermore, the published results for the cases of constant background fields and plane wave collision [8, 10, 13] are presented.

Chapters 3 and 4 set the prerequisites for an appropriate numerical scheme to solve the underlying nonlinear PDE's. Two key characteristics of the modified Maxwell equations play a crucial role when deciding which numerical schemes to use. Due to the hyperbolic nature of the nonlinear Maxwell equations schemes such as finite elements are unsuitable for the problem. Moreover, the need to compute nonlinearities implies that the use of staggered grids, such as the one in the Yee algorithm, is inappropriate.

In chapter 5 the QVS algorithm is explained in detail. Additionally, a performance analysis of it in terms of numerical error, computational load scaling, numerical dispersion, and further numerical artifacts is made. It is shown that the QVS algorithm can be configured in a way that it outperforms classical schemes such as the Yee algorithm, requiring as little as 20 points per wavelength to achieve a relative precision of  $10^{-13}$  with an orientation independent dispersion error of less than  $10^{-50}$ . On top of that, it is shown that there is a considerable performance boost when using Jacobi matrices for the numerical calculations of polarization and magnetization.

In chapter 6 it is shown that the algorithm is in excellent agreement with published results. The agreement is especially surprising in the benchmarks against [8] and [13], in which the calculations are made using point like probe photons and computing interaction cross sections, while the simulations use an em-wave representation. However, as the effects in [8, 13] are independent of the probe pulse shape and both, the analytical steps in [8, 13] as well as the numerical scheme in this thesis are mathematically consistent, it is to be expected that the results agree. Furthermore, as can be seen, e.g., in the benchmark against [10] the simulations

## 8. Summary and conclusions

always present a complete picture. This means that independent of the initial settings all the information to all perturbation orders is present in the numerical results.

Since the number of assumptions made in the derivation of the QVS algorithm is small, it is possible to use it to access scenarios not easily accessible by analytic means. Those include non-zero vacuum high harmonic generation, high harmonic generation in higher dimensions, scattering, and refraction of light by light.

### 8.1. Outlook

As is shown, the QVS algorithm represents a possibility to simulate the effects of the nonlinear vacuum to a high degree of accuracy. There are multiple applications for the QVS scheme. It can be used as a benchmark tool for future analytic results, giving a fast and easy way to verify these results. Furthermore, it can be used to more realistically compute the expectations of given experimental settings. Lastly, QVS simulations may be used to analyze the robustness of a range of nonlinear quantum vacuum effects. It can also help to find ways of how to improve the sensitivity of quantum vacuum measurements.

For example, to check the robustness of quantum vacuum effects it can be measured to which extent noise affects the results when inserted in the pump and probe beams.

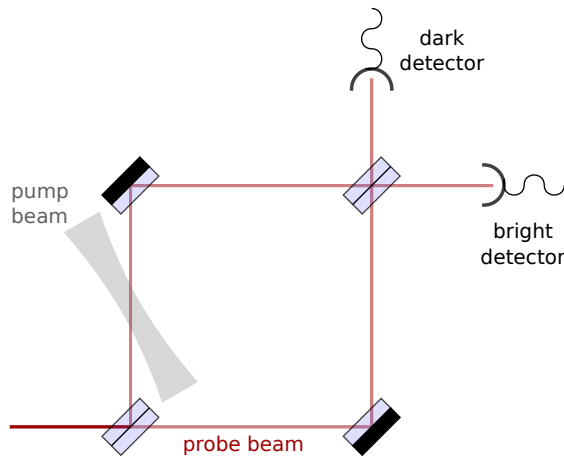


**Figure 8.1.:** Depiction of the proposed experimental setup for vacuum birefringence using a Mach-Zehnder interferometer. The interaction of the probe with the pump occurs only in one of the arms. Therefore, in an ideal setting, the wave generated through this interaction will not cancel out when rejoining the two arms causing it to become the only signal obtained in the center of the dark detector.

A possible procedure to improve measurements is using a Mach-Zehnder interfer-

ometer (see figure 8.1). Here, the relative signal strength is improved by interference.

The question is, how imperfections of the different optical elements can alter the measurements. This question can be addressed by simulating the regions of interest (see boxes in figure 8.2) and using linear propagators between them. Due to the accuracy of the QVS algorithm imperfections in the optical elements can be reproduced up to the nm scale. The required changes to simulate beam splitters and mirrors only require minor adjustment in the computation of  $\vec{M}$  and  $\vec{P}$ .

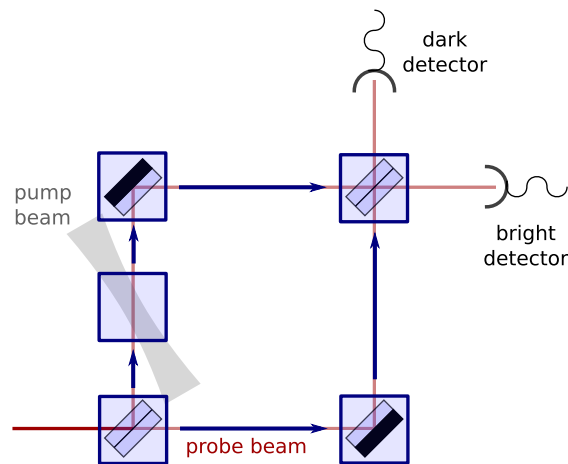


**Figure 8.2.:** Depiction of the proposed measurement setup for regions of interest (blue boxes) for an experiment using a Mach-Zehnder interferometer. The blue arrows denote the areas where linear propagators would be used.



# Publications

Part of this thesis is based on the publication:

- **An implicit ODE-based numerical solver for the simulation of the Heisenberg-Euler equations in 3+1 dimensions**  
Arnau Pons Domenech and Hartmut Ruhl  
*Accepted for publication at Journal of Computational Physics*  
arXiv:1607.00253



# A. Notation

This section provides a quick lookup for the Symbols used throughout this thesis. To speed up the search of a specific symbol they have been divided into four subtables (uppercase italic-, lowercase italic-, greek- and other symbols) each of which is lexicographically sorted.

Symbol	Definition	Def. Eq.
$A(x)$	Amplitude of an electric field at position $x$	
$A_i$	$i$ -th component of the gauge field	(2.12)
$\mathbf{A}$	Matrix element of $\mathbb{R}^{6 \times 6}$ containing the nonlinear contributions to the magnetization	(5.13)
$\vec{B}$	Magnetic field	
$\mathbf{B}$	Matrix element of $\mathbb{R}^{6 \times 6}$ containing the nonlinear contributions to the polarization	(5.14)
$\vec{D}$	Electric displacement field	(1.2)
$D_x$	Covariant derivative in $x$ direction	(2.11)
$\vec{E}$	Electric field	
$E_0$	Amplitude of the Gaussian envelope function of a Gauss pulse	
$\vec{E}_0$	Polarized amplitude of the Gaussian envelope function of a Gauss pulse (equal to $\vec{p}E_0$ )	
$E_{cr}$	Schwinger limit for the electric field strength	
$\mathcal{E}$	Energy (not noted as $E$ to avoid confusions)	
$\mathcal{E}_\perp$	Energy of the projection of the electric field of a probe in the direction perpendicular to the original polarization	(6.8)
$\mathcal{E}_\parallel$	Energy of the projection of the electric field of a probe in the direction parallel to the original polarization	(6.8)
$F_{\mu\nu}$	Electromagnetic field tensor	(2.35)
$F_{\mu\nu}^*$	Dual electromagnetic field tensor	
$\mathcal{F}$	1st electromagnetic invariant	(2.118)
$\mathcal{G}$	2nd electromagnetic invariant	(2.118)
$G(\mathbf{x}, \mathbf{x}')$	Green function between $\mathbf{x}$ and $\mathbf{x}'$	(2.23)
$\mathcal{H}$	Hamiltonian	
$\vec{H}$	Magnetic displacement field	(1.2)

## A. Notation

Symbol	Definition	Def. Eq.
$\mathbf{J}_{\vec{A}}(\vec{B})$	Jacobi Matrix of $\vec{A}$ w.r.t. $\vec{B}$	(5.4)
$\mathcal{L}$	Lagrangian	
$\mathcal{L}_{\text{HE}}$	Heisenberg-Euler Lagrangian	(2.158)
$\vec{M}$	Magnetization	
$\vec{P}$	Polarization	
$\mathbf{Q}_i$	Rotation computation matrices	(5.6)
$\mathbf{R}_i$	Rotation matrices into eigendirections	(5.17)
$R_{e^+e^-}$	Electron positron pair creation rate	(2.148)
$S$	Action	
$\vec{S}$	Derivation Stencil used to compute derivations on a finite difference lattice	(3.20)
$U(s)$	Proper time evolution operator	(2.55)
$W^{(1)}$	Effective action obtained by averaging out the fermionic degrees of freedom	
$a$	1st secular invariant	(2.122)
$b$	2nd secular invariant	(2.122)
$c$	Speed of light (set to 1 in this thesis)	
$\vec{e}_i$	Unit vector in direction $i$	
$e$	Elemental charge	
$f_{\text{Ny}}$	Nyquist frequency	(3.21)
$h$	Planck constant	
$\hbar$	Reduced Planck constant	
$\vec{j}$	Electric current density vector	
$\hat{k}$	Propagation direction of an em-wave	
$\vec{k}$	Propagation vector of an em-wave, equal to $\hat{k}/\lambda$	
$\mathbf{k}$	Propagation 4-vector for an em-wave, equal to $(\omega \vec{k})$	
$m$	Electron mass	
$n_{\pm}$	Refractive index in dependence of the relative polarization w.r.t. the background field	(2.183)
$\vec{p}$	Polarization direction of a plane wave	
$\vec{u}$	Em-field, equal to $(\vec{E} \vec{B})$	(5.9)
$v_g$	Group velocity of a em-wave	
$v_{ph}$	Phase velocity of a em-wave	
$w_0$	Waist size of a Gaussian beam	
$\vec{x}_0$	When describing a Gaussian pulse, position of the maximum of the envelope function at $t = 0$	
$z_r$	Rayleigh length of a Gaussian beam	

Symbol	Definition	Def. Eq.
$\Pi$	Modified impulse operator	(2.30)
$\Phi$	When describing a Gaussian pulse, variance of the envelope function times $\sqrt{2}$	
$\Psi$	Dirac spinor	
$\Psi^\dagger$	Conjugated Dirac spinor	
$\bar{\Psi}$	Adjoint Dirac spinor	
$\alpha$	Fine structure constant	
$\gamma^i$	i-th gamma matrix	
$\delta^{(n)}$	Delta function in $n$ dimensions	
$\delta f$	Variation of $f$	
$\epsilon_{ij\dots}$	Levi-Civita tensor	
$\eta$	Covariant metric	
$\lambda$	Wavelength of an em-wave	
$\lambda_c$	Compton wavelength	
$\xi(x)$	Gouy phase	
$\rho_f$	Electrical charge density	
$\sigma$	Angle between the polarization vector of a pump and the polarization vector of a probe	
$\chi^{(n)}$	Matrix element of $\mathbb{R}^{3^n}$ used to describe the coupling of the electric fields in the n-th order	
$\omega$	Angular frequency	
$\mathbf{1}_n$	Identity matrix in $\mathbb{R}^{n \times n}$	
$\hat{\cdot}$	Vector normalization operator	
Tr	Trace over discrete and continuous dimensions	
tr	Trace over discrete dimensions	(2.22)
$\partial_x$	Partial derivative with respect to $x$	



## B. Further calculations

### Derivation of the dispersion relation

Starting with (5.30) and reducing it to one dimension j

$$\begin{aligned}
0 &= \det \left( i\omega \mathbf{1}_6 + \begin{pmatrix} \mathbf{0}_3 & \mathbf{Q}_j \\ -\mathbf{Q}_j & \mathbf{0}_3 \end{pmatrix} \mathbf{R}_j \sum_{\nu} \frac{1}{\Delta_j} \mathcal{S}_{\nu} \mathbf{R}_j^{\top} e^{i\nu k_j} \right) \\
&= \det \left( i\omega \mathbf{R}_j \mathbf{R}_j^{\top} + \mathbf{R}_j \mathbf{R}_j^{\top} \begin{pmatrix} \mathbf{0}_3 & \mathbf{Q}_j \\ -\mathbf{Q}_j & \mathbf{0}_3 \end{pmatrix} \mathbf{R}_j \sum_{\nu} \frac{1}{\Delta_j} \mathcal{S}_{\nu} e^{i\nu k_j} \mathbf{R}_j^{\top} \right) \\
&= \underbrace{\det(\mathbf{R}_j)}_1 \det \left( i\omega \mathbf{1}_6 + \mathbf{R}_j \begin{pmatrix} \mathbf{0}_3 & \mathbf{Q}_j \\ -\mathbf{Q}_j & \mathbf{0}_3 \end{pmatrix} \mathbf{R}_j^{\top} \sum_{\nu} \frac{1}{\Delta_j} \mathcal{S}_{\nu} e^{i\nu k_j} \right) \underbrace{\det(\mathbf{R}_j^{\top})}_1 \\
&\stackrel{(5.18)}{=} \det \left( i\omega \mathbf{1}_6 + \text{diag}(1, 1, -1, -1, 0, 0) \sum_{\nu} \frac{1}{\Delta_j} \mathcal{S}_{\nu} e^{i\nu k_j} \right) \\
&\stackrel{\text{def } \mathcal{S}_{\nu}}{=} \det \left( i\omega \mathbf{1}_6 + \text{diag}(1, 1, -1, -1, 0, 0) \sum_{\nu} \frac{1}{\Delta_j} \text{diag}(s_{\nu}^b, s_{\nu}^b, s_{\nu}^f, s_{\nu}^f, s_{\nu}^n, s_{\nu}^n) e^{i\nu k_j} \right) \\
&= \det \left( i\omega \mathbf{1}_6 + \sum_{\nu} \frac{1}{\Delta_j} \text{diag}(s_{\nu}^b, s_{\nu}^b, -s_{\nu}^f, -s_{\nu}^f, 0, 0) e^{i\nu k_j} \right) \\
&= \left( i\omega + \sum_{\nu} \frac{1}{\Delta_j} s_{\nu}^b e^{i\nu k_j} \right)^2 \left( i\omega - \sum_{\nu} \frac{1}{\Delta_j} s_{\nu}^f e^{i\nu k_j} \right)^2 (i\omega)^2 \\
&\stackrel{-s_{\nu}^b = s_{-\nu}^f}{=} \left( i\omega - \sum_{\nu} \frac{1}{\Delta_j} s_{\nu}^f e^{i\nu k_j} \right)^2 \left( i\omega - \sum_{\nu} \frac{1}{\Delta_j} s_{\nu}^f e^{-i\nu k_j} \right)^2 (i\omega)^2,
\end{aligned}$$

from which it follows that

$$\omega = 0 \quad \wedge \quad i\omega = \sum_{\nu} \frac{1}{\Delta_j} s_{\nu}^f e^{i\nu k_j} \quad \wedge \quad i\omega = \sum_{\nu} \frac{1}{\Delta_j} s_{\nu}^f e^{-i\nu k_j}.$$

Here the  $\omega = 0$  solution represents the dispersion relation of the non-propagating component of the em-wave. The other two solutions can be combined to form the

## B. Further calculations

expression

$$2i\omega = \sum_{\nu} \frac{s_{\nu}^f}{\Delta_j} [(e^{i\nu k_j} + e^{-i\nu k_j}) + (e^{i\nu k_j} - e^{-i\nu k_j})].$$

which contains all the information on  $\omega$ . Dividing both sides of the equation by  $2i$  and using the Euler-deMoivre identities finally results in

$$\begin{aligned}\omega &= \sum_{\nu} \frac{s_{\nu}^f}{\Delta_j} \left[ \frac{1}{2i} (e^{i\nu k_j} + e^{-i\nu k_j}) + \frac{1}{2i} (e^{i\nu k_j} - e^{-i\nu k_j}) \right] \\ &= \sum_{\nu} \frac{s_{\nu}^f}{\Delta_j} \left[ \frac{1}{i} \cos(\nu k_j) + \sin(\nu k_j) \right] \\ &= \sum_{\nu} \frac{s_{\nu}^f}{\Delta_j} \sin(\nu k_j) - i \sum_{\nu} \frac{s_{\nu}^f}{\Delta_j} \cos(\nu k_j)\end{aligned}$$

# Acknowledgements

## DANK AN...

Meinem Doktorvater Prof. Dr. Hartmut Ruhl für seine Betreuung, Unterstützung und vor allem für seine Geduld.

Prof. Dr. Holger Gies, Prof. Dr. Joachim Rädler, Prof. Dr. Mattias Punk, Prof. Dr. Jan von Delft und Prof. Dr. Bert Nickel, für die Einwilligung, in meiner Prüfungskommission mitzuwirken.

Ute Tobiasch für ihre unbezahlbare Unterstützung in der Navigation des Bürokratischen Labyrinths der Universität.

Patrick Böhl für seine Hilfe bei den ersten Schritten in der Welt der Quantenvakuumphysik.

Karl-Ulrich Bamberg für seine technische Betreuung und seinen Hinweisen zur effizienten Programmierung.

Viktoria Pauw für ihr Engagement in dem Unterfangen aus dem Lehrstuhl mehr als nur eine Gruppe von Doktoranten zu machen.

Pascal du Bosque für die Kameradschaft ohne die das Studium und die Promotion wesentlich schwerer gewesen wären.

Angel Palomar Vidal und Helena Curulla Matosas für die unzählbaren Jahre Freundschaft.

Meiner Familie für deren bedingungslose moralische und seelische Unterstützung vor und während der Promotion.



# Bibliography

- [1] J. Clerk Maxwell. A dynamical theory of the electromagnetic field. *Philosophical Transactions of the Royal Society of London*, 155:459–512, 1865.
- [2] D.J. Griffiths. *Introduction to Electrodynamics*. Prentice Hall, 1999.
- [3] P. Dirac. The quantum theory of the emission and absorption of radiation. *Proceedings of the Royal Society of London A: Mathematical, Physical and Engineering Sciences*, 114(767):243–265, 1927.
- [4] W. Heisenberg and H. Euler. Folgerungen aus der diracschen theorie des positrons. *Zeitschrift für Physik*, 98(11):714–732.
- [5] Colin Danson, David Hillier, Nicholas Hopps, and David Neely. Petawatt class lasers worldwide. *High Power Laser Science and Engineering*, 3:e3 (14 pages), 2015.
- [6] T. Cowan and Hibef Collaboration. Status of the proposed Helmholtz International Beamline for Extreme Fields (HIBEF) at the European XFEL. In *APS Meeting Abstracts*, October 2013.
- [7] N Miyanaga, H Azechi, KA Tanaka, T Kanabe, T Jitsuno, J Kawanaka, Y Fujimoto, R Kodama, H Shiraga, K Knodo, et al. 10-kj pw laser for the firex-i program. *Journal de Physique IV (Proceedings)*, 133:81–87, 2006.
- [8] Felix Karbstein, Holger Gies, Maria Reuter, and Matt Zepf. Vacuum birefringence in strong inhomogeneous electromagnetic fields. *Phys. Rev. D*, 92:071301, Oct 2015.
- [9] Julian Schwinger. On gauge invariance and vacuum polarization. *Phys. Rev.*, 82:664–679, 1951.
- [10] B. King, P. Böhl, and H. Ruhl. Interaction of photons traversing a slowly varying electromagnetic background. *Phys. Rev. D*, 90:065018, Sep 2014.
- [11] P. Böhl, B. King, and H. Ruhl. Vacuum high-harmonic generation in the shock regime. *Phys. Rev. A*, 92:032115, Sep 2015.

## Bibliography

- [12] Holger Gies, Felix Karbstein, and Nico Seegert. Quantum reflection as a new signature of quantum vacuum nonlinearity. *New Journal of Physics*, 15(8):083002, 2013.
- [13] Victor Dinu, Tom Heinzl, Anton Ilderton, Mattias Marklund, and Greger Torgrimsson. Vacuum refractive indices and helicity flip in strong-field qed. *Phys. Rev. D*, 89:125003, Jun 2014.
- [14] Victor Dinu, Tom Heinzl, Anton Ilderton, Mattias Marklund, and Greger Torgrimsson. Photon polarization in light-by-light scattering: Finite size effects. *Phys. Rev. D*, 90:045025, Aug 2014.
- [15] W. Dittrich and M. Reuter. *Effective Lagrangians in Quantum Electrodynamics*. Lecture Notes in Physics. Springer-Verlag, 1985.
- [16] J.J. Sakurai and J. Napolitano. *Modern Quantum Mechanics*. Addison-Wesley, 2011.
- [17] Gerald V. Dunne and Theodore M. Hall. Borel summation of the derivative expansion and effective actions. *Phys. Rev. D*, 60:065002, Aug 1999.
- [18] Holger Gies and Lars Roessler. Vacuum polarization tensor in inhomogeneous magnetic fields. *Phys. Rev. D*, 84:065035, Sep 2011.
- [19] Peter J. Mohr, David B. Newell, and Barry N. Taylor. CODATA recommended values of the fundamental physical constants: 2014, Jul 2015.
- [20] J.V. Narlikar and T. Padmanabhan. *Gravity, Gauge Theories and Quantum Cosmology*. Fundamental Theories of Physics. Springer, 1986.
- [21] Michael E. Peskin and Daniel V. Schroeder. *An Introduction to quantum field theory*. Addison-Wesley, Reading, USA, 1995.
- [22] G. M. Shore. Superluminality and uv completion. 2007.
- [23] J.S. Toll. The dispersion relation for light and its application to the problems involving electron pairs. *Ph.D. Thesis*, 1952.
- [24] Rudolf Baier and P. Breitenlohner. The vacuum refraction index in the presence of external fields. *Il Nuovo Cimento B*, 47:117–120, 1967.
- [25] Z. Bialynicka-Birula and I. Bialynicki-Birula. Nonlinear effects in quantum electrodynamics. photon propagation and photon splitting in an external field. *Phys. Rev. D*, 2:2341–2345, Nov 1970.

- [26] Stephen L. Adler. Photon splitting and photon dispersion in a strong magnetic field. *Annals Phys.*, 67:599–647, 1971.
- [27] F Della Valle, U Gastaldi, G Messineo, E Milotti, R Pengo, L Piemontese, G Ruoso, and G Zavattini. Measurements of vacuum magnetic birefringence using permanent dipole magnets: the pvlas experiment. *New Journal of Physics*, 15(5):053026, 2013.
- [28] Zavattini, Guido and Calloni, Enrico. Probing for new physics and detecting non-linear vacuum qed effects using gravitational wave interferometer antennas. *Eur. Phys. J. C*, 62(3):459–466, 2009.
- [29] Patrick Albert Böhl. Vacuum harmonic generation in slowly varying electromagnetic backgrounds. September 2016.
- [30] William H. Press, Saul A. Teukolsky, William T. Vetterling, and Brian P. Flannery. *Numerical Recipes 3rd Edition: The Art of Scientific Computing*. Cambridge University Press, 3 edition, 2007.
- [31] L.C. Evans. *Partial Differential Equations*. Graduate studies in mathematics. American Mathematical Society, 2010.
- [32] Kane S. Yee. Numerical solution of initial boundary value problems involving maxwell’s equations in isotropic media. *IEEE Trans. Antennas and Propagation*, pages 302–307, 1966.
- [33] A. Taflove and S.C. Hagness. *Computational Electrodynamics: The Finite-difference Time-domain Method*. Artech House antennas and propagation library. Artech House, 2005.
- [34] O. Forster. *Analysis 1: Differential- und Integralrechnung einer Veränderlichen*. vieweg studium; Grundkurs Mathematik. Vieweg+Teubner Verlag, 2008.
- [35] Alan C. Hindmarsh and Radu Serban. User documentation for ccode v2.8.2, 2015.
- [36] E. Hairer, S. P. Nørsett, and G. Wanner. *Solving Ordinary Differential Equations I (2Nd Revised. Ed.): Nonstiff Problems*. Springer-Verlag New York, Inc., New York, NY, USA, 1993.
- [37] E. Hairer and G. Wanner. *Solving Ordinary Differential Equations II: Stiff and Differential-Algebraic Problems*. Springer Series in Computational Mathematics. Springer Berlin Heidelberg, 2010.

## Bibliography

- [38] Ran Raz. On the complexity of matrix product. pages 144–151, 2002.
- [39] W. Zinth and U. Zinth. *Optik: Lichtstrahlen - Wellen - Photonen*. Oldenbourg, 2009.
- [40] Wu-yang Tsai and Thomas Erber. Propagation of photons in homogeneous magnetic fields: Index of refraction. *Phys. Rev. D*, 12:1132–1137, Aug 1975.
- [41] B King and T Heinzl. Measuring vacuum polarisation with high power lasers. *arXiv preprint arXiv:1510.08456*, 2015.